

An Exploratory Study of the Application of Carbon Nanotubes to Skin Friction Measurements

by

Bancroft W. Henderson

Master's Thesis submitted to the Faculty of the
Virginia Polytechnic Institute and State University
in partial fulfillment of the requirements for the degree of

Master of Science
in
Aerospace Engineering

APPROVED:

Dr. Joseph A. Schetz, Chairman

Dr. Ahmad Safaai-Jazi

Dr. Eric R. Johnson

July 16, 2004
Blacksburg, VA

Keywords: skin friction, carbon nanotubes, fiber-optic, wall shear

An Exploratory Study of the Application of Carbon Nanotubes to Skin Friction Measurements

Bancroft W. Henderson
Dr. Joseph A. Schetz, Chairman
Aerospace Engineering

(Abstract)

A small shear sensor utilizing an array of carbon nanotubes to support a sensor head was developed for use in steady, high speed, 2D flow. The sensor is a non-intrusive, direct measurement device with a 2 x 2 mm square sensor head surrounded by a small gap on each side (~0.004 inches). The translation of the sensing element is due to the nanotubes bending when a shear force is applied to the sensor head. Displacements are measured by an interferometric technique using fiber-optics to measure the distance the sensor head travels by viewing a polished side of the head. The fiber-optical displacement sensor is bonded to a stationary substrate so that all measurements are relative to a fixed position.

Arrays of carbon nanotubes were grown on bare 2 x 2 mm square silicon chips. The nanotubes were grown to heights of 75 microns with a thin layer of amorphous carbon on top. The silicon chips were then flipped, and the amorphous layer of carbon was bonded to bare 1 x 1 cm silicon substrates, making the bottom of 2 x 2 mm silicon chip the sensor head. The sensors were calibrated at Luna Innovations using a point-load technique. Four of the six sensors could not be successfully calibrated because they were fatally damaged during the last step of the calibration process. Wind tunnel tests were conducted on the one sensor that survived the calibration.

An arrangement was designed and built from aluminum to test the performance of the sensor in the Virginia Tech Supersonic Wind Tunnel. Seven test runs were conducted in this cold-flow facility at a nominal Mach number of 2.4 and stagnation pressures ranging from 50 – 90 psia. Two test runs gave skin friction values 3 – 20% lower than those values predicted by indirect measurement techniques before the sensor was damaged. While these first results are encouraging, further studies are clearly needed. Due to distinct anomalies in the displacement data during test run 3, it was concluded that

the sensor was damaged during this run. Possible explanations of the failure of this sensor are offered along with suggestions for future work.

Acknowledgements

I begin by saying thank you to my parents, Skip and Jane who have helped guide me to this point in my life. Their unwavering support and encouragement will never go underappreciated. To my friends and family, thank you for keeping me sane and reminding me that there is more to life than school.

Dr. J. Schetz, I am in debt to you for giving me this opportunity. Throughout the obstacles encountered during this project you always kept an optimistic attitude. I believe for every hurdle encountered I heard a relative story or joke. Thank you.

To Dr. A. Safaai-Jazi and Dr. E. Johnson, I appreciate your availability and eagerness to help when I approached with questions.

My thanks goes to Matt Orr, Matt Palmer, Alex Sang, Kelly Stinson-Bagby, Mike Tonks, and Mike Vercellino for your input and suggestions throughout this project.

I extend my gratitude to Steve Edwards, James Lambert, Bruce Stanger, and Larry Vicari for their generosity of their valuable time.

Lastly, I praise the Lord Almighty who makes all this possible.

Table of Contents

Abstract.....	ii
Acknowledgements.....	iv
Figures and Tables.....	vii
Figures.....	vii
Tables.....	x
Nomenclature.....	xi
1 INTRODUCTION.....	1
1.1 Drag Overview.....	1
1.2 Skin Friction Background.....	2
1.3 Measurement Techniques of Skin Friction.....	4
1.3.1 Method of Indirect Measurement.....	5
1.3.2 Method of Direct Measurement.....	8
1.4 Historical Overview of Direct Measurement Techniques.....	10
1.5 Motivation for Small Skin Friction Gage.....	14
1.6 Outline.....	15
2 CARBON NANOTUBES.....	16
2.1 Background.....	16
2.2 Properties of Carbon Nanotubes.....	19
2.2.1 Mechanical Properties.....	19
2.2.2 Electrical Properties.....	20
2.2.3 Electromechanical Properties of MWNTs.....	21
2.3 Growth Techniques of MWNTs.....	24
3 FREESTANDING ARRAY OF MWNTS AS A C_f GAGE.....	27
3.1 Freestanding MWNT.....	27
3.1.1 Fluid Dynamics.....	27
3.1.2 Analytical Design.....	31
3.2 Complications in the Fluid Dynamics.....	35
3.3 Electro-Optical Measurement Technique.....	37
4 TABLE TOP DESIGN UTILIZING MWNTS AS A C_f GAGE.....	41
4.1 Advantages of a Table Top Design.....	41
4.1.1 Analytical Design.....	42
4.2 Electromechanical Measurement Concept.....	44
4.2.1 Design of Sensor.....	46
4.2.2 Resistance of Substrates.....	47
4.2.3 Nominal Resistance of Nanotube Arrays.....	48
4.2.4 Theoretical Change in Resistance of Nanotube Arrays.....	49
4.3 Array of Nanotubes as a Flexure.....	51
4.3.1 Aligned MWNTs.....	52
4.3.2 Aligned MWNT Structures.....	53
4.3.3 'Lift-Up' Growth Technique.....	55
4.4 Potential Uncertainties.....	57
5 FABRICATION OF TABLE TOP DESIGNS.....	59
5.1 Electromechanical Measurement Design.....	59
5.1.1 First Concept Attempt.....	59

5.1.2	<i>Second Concept Attempt</i>	61
5.2	Mechanical Measurement Design.....	63
5.2.1	<i>Aligned MWNT Concept</i>	63
5.2.2	<i>Aligned MWNT Structures</i>	63
5.2.3	<i>'Lift-Up' Growth Concept</i>	64
5.2.3.1	<i>Ni + oxide Substrate</i>	65
5.2.3.2	<i>Ni + oxide with Au/Sn Substrate</i>	66
5.2.3.3	<i>Cr + Ni + oxide Substrate</i>	67
5.2.3.4	<i>Bare silicon chips</i>	67
5.3	Sensor Housing Design.....	69
5.4	Sensor Calibration.....	76
5.4.1	<i>Displacement Sensor</i>	76
5.4.2	<i>Temperature Sensor</i>	81
6	SUPERSONIC WIND TUNNEL TESTING	83
6.1	Components of Supersonic Wind Tunnel Testing.....	83
6.1.1	<i>Supersonic Wind Tunnel</i>	83
6.1.2	<i>Fiber-Optical Data Acquisition</i>	84
6.1.3	<i>High-Speed Camera</i>	84
6.2	Test Setup.....	86
6.3	Supersonic Wind Tunnel Test Results.....	87
6.3.1	<i>Initial Testing at Mach 2.4</i>	87
6.3.2	<i>Vacuum Test of Sensor</i>	89
6.3.3	<i>Mach 2.4 Results</i>	91
6.3.4	<i>Comparison of Results</i>	96
7	CONCLUSIONS AND RECOMMENDATIONS	99

Figure and Table References

Figures

Figure 1-1. Schematic of a winglet.....	1
Figure 1-2. Schematic of the boundary layer [4].....	2
Figure 1-3. Defect law plot [5].....	4
Figure 1-4. Schematic of a direct measurement technique.....	5
Figure 1-5. Various types of indirect measuring techniques [6].....	6
Figure 1-6. Schematic of the Stanton tube method [7].....	7
Figure 1-7. Illustration of point-load calibration technique [8].....	9
Figure 1-8. Schematic of a “nulling” skin friction gage [9].....	9
Figure 1-9. Illustration of test setup used by Froude [10].....	11
Figure 2-1. Buckey Ball structure of C ₆₀ [60]	16
Figure 2-2. A model of a SWNT [60]	16
Figure 2-3. A model of a telescopically extended MWNT [60]	17
Figure 2-4. Geometry of SWNTs [62]	17
Figure 2-5. Models of the three types of SWNTs [61]	18
Figure 2-6. Diagram of possible chiral vectors of SWNTs [62]	18
Figure 2-7. Schematic of beam bending using AFM [64].....	19
Figure 2-8. SEM image of a typical MWNT electric device [69].....	21
Figure 2-9. Conductance measuring technique of single nanotubes [70].....	21
Figure 2-10. Conductance versus bending angle of SWNT [72].....	22
Figure 2-11. Schematic of AFM tip deflection of a SWNT [71].....	23
Figure 2-12. Experimental results of conductance drop due to deformation [71].....	24
Figure 2-13. Schematic of arc-discharge growth method [74].....	25
Figure 2-14. Schematic of CVD growth process [75].....	25
Figure 2-15. SEM image of an array of aligned nanotubes [76].....	26
Figure 3-1. Plot of Reynolds number versus cylinder height and drag coefficient.....	29
Figure 3-2. Plot of load intensity versus cylinder height.....	31
Figure 3-3. Schematic of cylinder with linearly distributed load.....	31
Figure 3-4. Rotation angle and deflection due to linearly distributed load.....	33
Figure 3-5. Schematic representation of the velocity components acting on an element at angle θ to the flow.....	34
Figure 3-6. Convergence of the deflection of a hollow cylinder.....	34
Figure 3-7. Schematic of the different flow regions of a finite cylinder.....	37
Figure 3-8. Schematic of optical viewing path of nanotubes.....	37
Figure 3-9. Schematic of an incident wave into a nanotube-loaded medium at a deflection angle θ_0 [83].....	38
Figure 3-10. Magnitude of reflection coefficient versus deflection angle [83].....	40
Figure 3-11. Phase angle of the reflection coefficient versus deflection angle [83].....	40
Figure 4-1. Schematic of undeflected (solid) and deflection (dotted) nanotubes supporting a sensing element.....	41
Figure 4-2. Schematic of pressure gradient applied to the sensing element.....	42
Figure 4-3. Schematic of clamped-clamped nanotube with point load.....	42

Figure 4-4. Analytical solution of a clamped-constrained circular cylinder with point load at tip.....	44
Figure 4-5. Schematic of circuitry capable of measuring small resistance changes.....	45
Figure 4-6. Experimental setup used to measure small changes in resistance.....	45
Figure 4-7. Photograph of oscilloscope display.....	46
Figure 4-8. Schematic of a skin friction sensor using the electromechanical measurement technique.....	46
Figure 4-9. Illustration of silicon substrates bond to a glass slide.....	47
Figure 4-10. Schematic illustration of fiber optic displacement sensor [57].....	51
Figure 4-11. Diagram of Fiber Optic system used to measure gap distance [57].....	52
Figure 4-12. SEM images of aligned MWNT structures.....	53
Figure 4-13. Representation of the top view of one MWNT structure.....	54
Figure 4-14. Representation of the contribution to inertia of one nanotube.....	54
Figure 4-15. Schematic illustration of ‘Lift-up’ growth technique [88].....	56
Figure 4-16. Electron DOS of ideal nanotube and highly defective nanotube [89].....	57
Figure 4-17. Representation of ideally spaced nanotubes with identical geometries.....	58
Figure 5-1. SEM images of successful sensor head bond.....	60
Figure 5-2. Schematic illustration and photograph of bench test to determine is sensing element is free to displace.....	61
Figure 5-3. Photograph of optical fiber monitoring sensor head and buckled quartz capillary tube.....	61
Figure 5-4. Schematic drawing of the electrode mask on glass to electrically isolate nanotubes.....	62
Figure 5-5. SEM images of the patterned electrode strip.....	63
Figure 5-6. Dimensions of diced wafers and Ni film to be patterned.....	64
Figure 5-7. SEM images of patterned Ni film.....	65
Figure 5-8. SEM images of Ni + oxide samples.....	66
Figure 5-9. SEM image of a bundle of nanotubes.....	66
Figure 5-10. SEM images of Cr + Ni on oxide samples.....	67
Figure 5-11. SEM images of aligned nanotubes grown on bare silicon chips.....	67
Figure 5-12. Schematic illustration of product after bonding process.....	68
Figure 5-13. SEM image of the carbon nanotubes bonded to a silicon substrate with a strain gage epoxy.....	69
Figure 5-14. Schematic of sensor in the wind tunnel housing arrangement.....	70
Figure 5-15. Drawing of sensor plug housing.....	70
Figure 5-16. Drawing of test section floor plate.....	71
Figure 5-17. Drawing of sensor plug.....	71
Figure 5-18. Photograph of gage components with 6” scale.....	72
Figure 5-19. Drawing of shim stock.....	73
Figure 5-20. Photograph of shim stock taken through a microscope.....	73
Figure 5-21. Photograph of gage assembly.....	74
Figure 5-22. Setup used to apply shim stock to sensor plug.....	75
Figure 5-23. Photograph of the top view of the completed assembly.....	75
Figure 5-24. Schematic illustration of the calibration setup.....	77
Figure 5-25. Diagram and photograph of calibration setup.....	77
Figure 5-26. Plot of applied mass and measured displacement during calibration.....	79

Figure 5-27. Schematic illustration of sensor without nanotubes.....	80
Figure 5-28. Plot of gap distance during calibration of sensor without nanotubes.....	80
Figure 5-29. Photograph of sensor head positioned in shim stock after excess bonding agent was removed.....	81
Figure 5-30. The EFPI Surface-Attachable/Embedment Temperature Gage [91].....	82
Figure 5-31. Photograph of displacement sensor, temperature sensor, and sensor head taken through 50x microscope.....	82
Figure 6-1. Virginia Tech Supersonic Wind Tunnel layout.....	83
Figure 6-2. Photograph of high-speed camera setup.....	85
Figure 6-3. Single frame captured by high-speed camera during the start of the tunnel.....	85
Figure 6-4. Drawing of removable floor plate.....	86
Figure 6-5. Photograph of floor plate, sensor plug housing, shim stock, and sensor in the test section.....	87
Figure 6-6. Tunnel conditions for initial test run 1 at nominal Mach 2.4.....	88
Figure 6-7. Single picture captured by high-speed camera after sensor head failure.....	89
Figure 6-8. Schematic illustration of venting air pockets in a nanotube array.....	89
Figure 6-9. Photograph of the vacuum experiment setup.....	90
Figure 6-10. Measured pressures during vacuum experiment.....	91
Figure 6-11. Representative tunnel conditions for nominal Mach 2.4.....	92
Figure 6-12. Shear and temperature measurements of Run 02 at Mach 2.4.....	93
Figure 6-13. Shear and temperature measurements of Run 03 at Mach 2.4.....	95
Figure 6-14. Shear and temperature measurements of Run 04 at Mach 2.4.....	96
Figure 6-15. Predicted and measured skin friction values.....	98
Figure 7-1. Schematic illustration of venting air pockets in a nanotube array.....	100
Figure 7-2. SEM image of an array of MWNTs exposed to moisture.....	100

Tables

Table 1-1. List of history of skin friction gages [10-57]	14
Table 3-1. Convergence of values of tip displacement and rotation angle for a bent cylinder.....	35
Table 4-1. Summary of conductance drop due to bending angle.....	50
Table 5-1. Theoretical tip displacements based on array size.....	64
Table 5-2. List of calibration run number, masses applied, and measured displacements.....	78
Table 6-1. Test runs conducted on 05-27-04 at a nominal Mach number of 2.4.....	92

Nomenclature

a	Unit Vector
C_D	Drag Coefficient
C_f	Skin Friction Coefficient
D	Diameter
E	Modulus of Elasticity
G	Conductance
I	Moment of Inertia
L	Length
M	Mach Number, Moment
N	Number of Nanotubes
P	Pressure, Force
Pr	Prandtl Number
$R_{()}$	Resistance of ()
Re	Reynolds Number
S	Surface Area
St	Stanton Number
T	Temperature
W	Weight
u^*	Friction Velocity
U	Velocity
V	Shear, Velocity, Volume
Z	Vertical Distance
d	Diameter
$d(*)$	Derivative
g	Gravitational Constant
l	Length
m	Mass, Integer
n	Normal to wall, Integer
n_1	Refractive Index
q_0	Load Intensity
r	Radius
u^+	Velocity Divided by Friction Velocity
v	Displacement
v'	Slope
x	Horizontal Distance
y	Vertical distance
y^+	Transverse Coordinate for Law of the Wall

Greek

Δ	Change
Γ	Reflection Coefficient
δ	Boundary Layer Thickness, Deflection distance
ε	Relative Permittivity
λ	Wave Length
μ	Laminar Viscosity
ρ	Density, Resistivity
σ	Conductivity Constant
τ	Shear Force
θ	Chiral angle, Deformation Angle, Rotation Angle, Slope
ν	Laminar Kinematic Viscosity

Subscripts

D	Diameter
LSL	Laminar Sublayer
cr	Critical
cyl	Cylinder
e	Edge
i	Inner
j	Index
l	Length
n	Normal
o	Outer
$r1$	Region 1
$r2$	Region 2
$trans$	Transition
w	Wall
xx	About x-axis

1 INTRODUCTION

1.1 Drag Overview

Drag can be defined as an aerodynamic force between a vehicle and fluid which acts opposite to the motion of the vehicle. This resistive force can be split into two categories: pressure drag and skin friction drag. Pressure drag is a consequence of unequal dynamic pressures acting on an object. The dynamic pressure on the front of the object is not counterbalanced by an equal and opposite pressure on the rear [1]. This creates a resultant force acting against the motion of the object. Skin friction drag is related to the surface area of the vehicle exposed to the fluid. This type of drag is a result of the interaction between the surface of the body and a thin viscous layer directly adjacent to the surface of the body, known as the boundary layer.

An area of continuing interest is minimizing this resistance known as drag. If a recent modification in the Boeing 737 commercial airliner is examined, one can easily see the gains, both performance-wise and economically, of reducing drag. Boeing recently added 8 foot vertical extensions to the 737's wings, called winglets, to reduce the drag of the airplane (Fig. 1-1). This modification increased fuel efficiency by 4 percent, extended the range of the aircraft, and reduced the wear on the aircraft's engines. The aircraft now has better performance characteristics and costs less to fly [2].

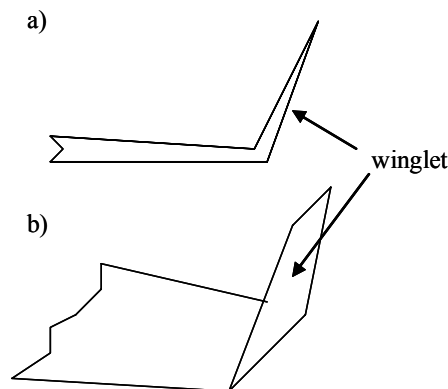


Figure 1-1. Schematic of a winglet. Front a) and oblique b) views.

The capability of understanding both the pressure and skin friction drag on a body can help improve the performance and economics of any aerodynamic system.

Improving these parameters is a driving factor in the ability to quantify the two types of drag. The history of the prediction of pressure drag has resulted in mathematical and computational methods that achieve satisfactory accuracy in a wide variety of cases. Quantifying the skin friction drag, on the other hand, has required a much greater dependency on empirical results [3]. Only the simplest cases of laminar, two-dimensional, constant-property flow for special pressure gradients have been successfully modeled analytically [5]. To an engineer, these simple models do not lend much use since they require a great deal of prior knowledge of the flow under study. Thus, there is a demand to measure skin friction directly at desired locations on an aerodynamic body via a sensor to obtain the skin friction distribution. This helps to identify and correct problem areas in the design of an aerodynamic system.

1.2 Skin Friction Background

Skin friction, or wall shear stress, τ_w , is proportional to the velocity gradient normal to the surface. This relationship for a Newtonian fluid is expressed as,

$$\tau_w = \mu \left. \frac{\partial U}{\partial n} \right|_w \quad (1-1)$$

where μ is dynamic viscosity of the fluid. Equation (1-1) states the greater the velocity gradient normal to the surface the larger the value of wall shear stress on the surface. Figure 1-2 displays a schematic illustration of a velocity gradient in the boundary layer formed over a flat plate. From this figure the reader can visualize how the shape of the velocity profile will influence the value of wall shear stress, and vice versa.

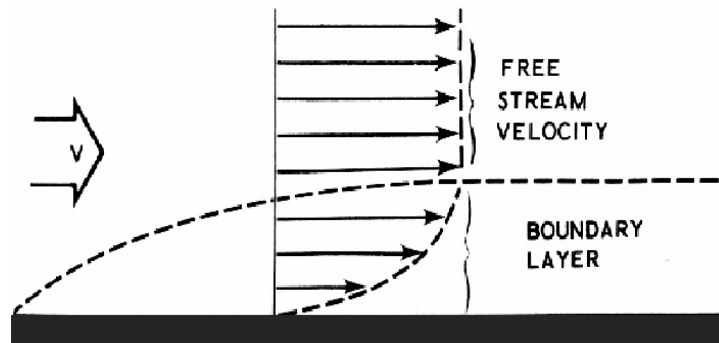


Figure 1-2. Schematic illustration of the boundary layer over a flat surface [4].

CHAPTER 1 – INTRODUCTION

The wall shear stress is often non-dimensionalized by the dynamic pressure at the boundary layer edge. This quantity is known as the skin friction coefficient, C_f . Equation (1-2) shows this relationship,

$$C_f = \frac{\tau_w}{\frac{1}{2}\rho U_e^2} \quad (1-2)$$

where ρ is the density and U_e is the velocity at the edge of the boundary layer.

The modeling of turbulent flows utilizes a normalizing quantity called the friction velocity, u_* , to express the influence of the wall shear (Eqn. 1-3).

$$u_* \equiv \sqrt{\frac{\tau_w}{\rho}} = U_e \sqrt{\frac{C_f}{2}} \quad (1-3)$$

Using the friction velocity one can choose the proper scaling parameter such to correlate the desired region of turbulent boundary layer profiles. This scaling parameter for the outer region is termed the defect law (Eqn. 1-4),

$$\frac{(U - U_e)}{u_*} = f\left(\frac{y}{\delta}\right) \quad (1-4)$$

where U is the local tangential velocity in the boundary layer, y is the vertical distance from the surface and δ is the boundary layer thickness. Figure 1-3 is a plot, called a defect law plot, which displays various turbulent, flat-plate boundary layer profiles correlated to a common profile by the defect law.

The successful correlation of the outer region of turbulent boundary layers shown in Figure 1-3 does not hold for small values of y/δ [5]. A different scaling parameter is needed for this near-wall region, which makes up the inner 10 percent of the total boundary layer. For this region the scaling parameter is termed the law of the wall,

$$\frac{U}{u_*} = g\left(\frac{yu_*}{\nu}\right) \quad (1-5)$$

where ν is the kinematic viscosity of the fluid.

Equations (1-4) and (1-5) are primary components in the development of computational models for fluid dynamics (CFD). By improving the techniques used to measure values of wall shear directly, one could use this data in turbulence modeling, which is fundamental to accurate CFD analysis. From a practical standpoint, skin friction

is a key item in assessing the performance of any fluids system [8]. Obtaining the skin friction distribution over a fluids system can help identify and correct problem areas in the design of the system. An emerging area of the application of skin friction measurements is as critical and sensitive inputs for flow control systems [8].

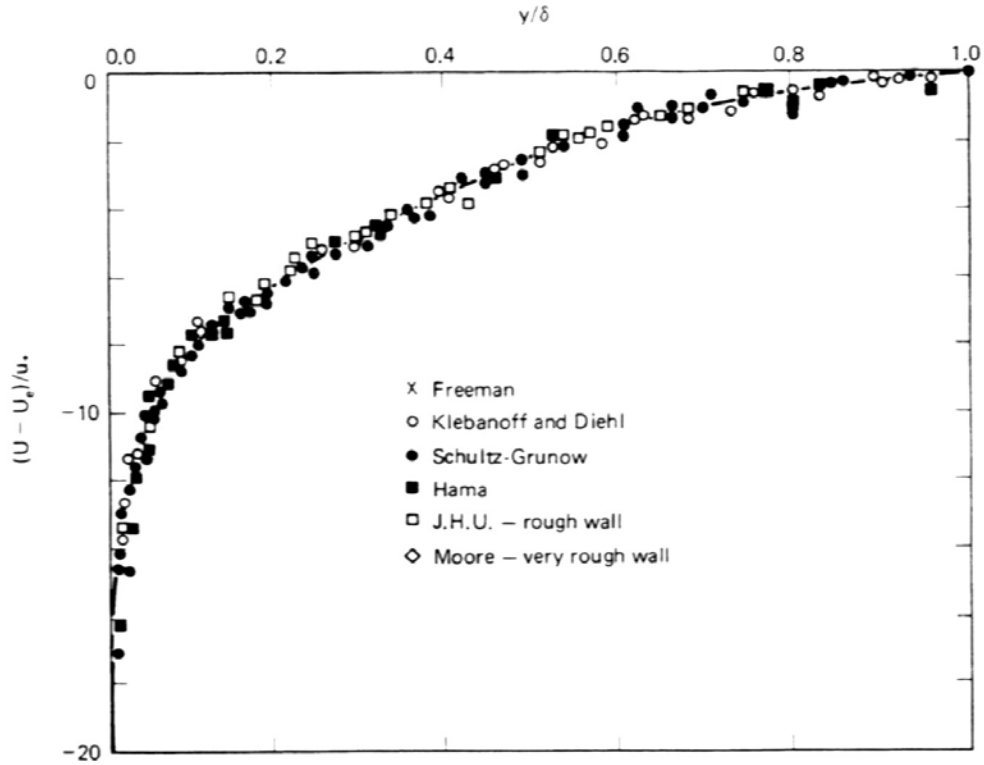


Figure 1-3. Defect law plot for turbulent, flat-plate boundary layer profiles [5].

1.3 Measurement Techniques of Skin Friction

As previously mentioned only the simplest cases of laminar, constant-property, steady flow over a flat plate have been analytically modeled. These models are relatively useless for engineers since prior knowledge of the flow for many practical applications may be impossible to obtain. One emerging field of practical applications, for which skin friction quantification is critical, is flow control. Since the dependability of such models is uncertain, one must look to other methods to obtain highly localized skin friction measurements.

There are two types of methods used to make skin friction measurements: indirect and direct measurements. Indirect measurements gather information of the flow and make estimations of the wall shear based on some analogy or data correlation. These

types of measurement techniques depend on prior knowledge of the flow. Also, some methods require optical access to the area of study. Much of the time this is either very difficult or impossible since an optical view of the test area is not always present. Direct measurements are made by replacing a portion of the surface by a movable sensing element with a very small gap around the perimeter (Fig. 1-4). This sensing element is mounted on top of some sort of flexure. When flow is initiated over the element, either the strain in the flexure or the displacement of the element is measured. This measurement corresponds to a value of wall shear for which the sensor has previously been calibrated. These two techniques sound simple; however, there are far-reaching complications for each.

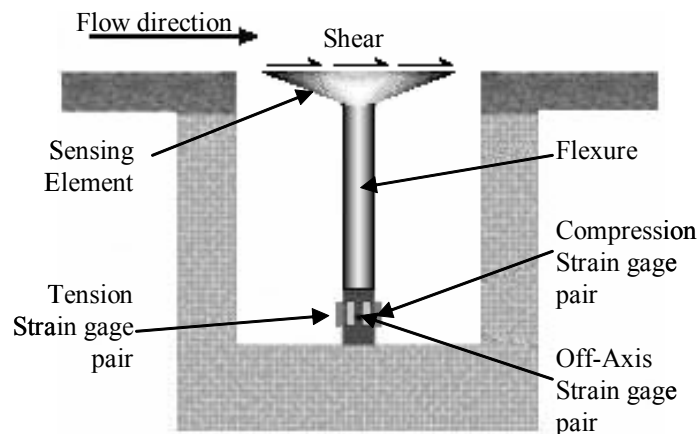


Figure 1-4. Schematic of a direct measurement technique.

1.3.1 Method of Indirect Measurement

Several techniques of indirect measurement of wall shear rely on the measurement of quantities such as velocity or dynamic pressure at known locations in the boundary layer. The most common measurement techniques for velocity and pressures are hot-wire anemometry, laser Doppler anemometry (LDA), Preston tube, and Stanton tube. Figure 1-5 displays some common indirect measurement techniques, what calibration is used, and the underlying principle behind the technique. A short discussion of the most common procedures will follow.

Hot-wire anemometry is a procedure which makes velocity measurements throughout the boundary layer. Knowing the vertical position of these velocity measurements allows a correlation to wall shear through the law of the wall. This in turn,

CHAPTER 1 – INTRODUCTION

is a limitation of the technique because assuming the law of the wall to hold for all pressure gradients has far-reaching implications [5]. A major source of error stems from the uncertainty of the vertical position of the velocity measurement relative to the wall. A limitation of hot-wire anemometry is that this technique is an intrusive procedure. In any type of experimentation, altering the flow field is an undesirable consequence since the physical environment is no longer the same. This technique cannot be employed to a variety of flow environments because hot-wire probes are not physically robust.

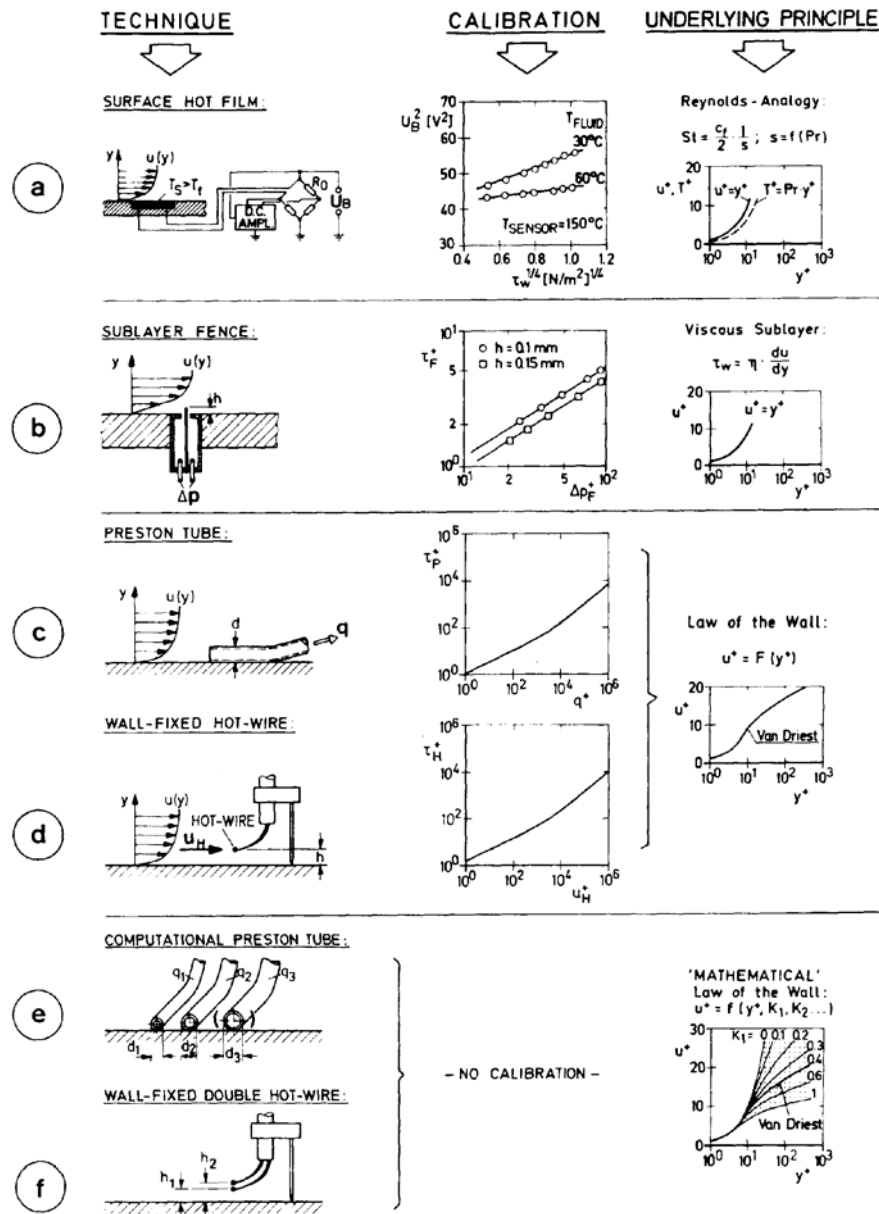


Figure 1-5. List of various types of indirect measuring techniques [6].

CHAPTER 1 – INTRODUCTION

LDA is similar to hot-wire anemometry in that this procedure makes velocity measurements throughout the boundary layer. The same disadvantages arise in errors of measurement location relative to the wall and the assumption of the law of the wall. This technique is expensive, where a simple system typically costs \$40,000. A major advantage to LDA is that the method is not intrusive and can obtain three-dimensional velocity measurements. This technique also can obtain data at a high frequency rate, useful in measurements of unsteady flow.

An indirect method which makes pressure measurements is the Preston tube. As seen in Figure 1-5, the Preston tube lies on the surface of the wall and makes dynamic pressure measurements in the laminar sublayer and log region of the boundary layer. Like hot-wire anemometry and LDA, a value of the wall shear is correlated through the law of the wall. Disadvantages arise from the law of the wall assumption and because it is an intrusive method. This technique also is not available for unsteady flows because it cannot obtain data at a high frequency. The last limitation of this method is that the boundary layer thickness must be large enough such that the tube lies in the inner region.

The Stanton tube method can be seen in Figure 1-6. This technique uses a static pressure port and a razor blade. By partial covering the port a total pressure reading can be made in the laminar sublayer of the boundary layer. The limitations of this procedure are that it is an intrusive method which depends on the law of the wall assumption. Like the Preston tube it has a slow response, making it a method useful for steady flow measurements.

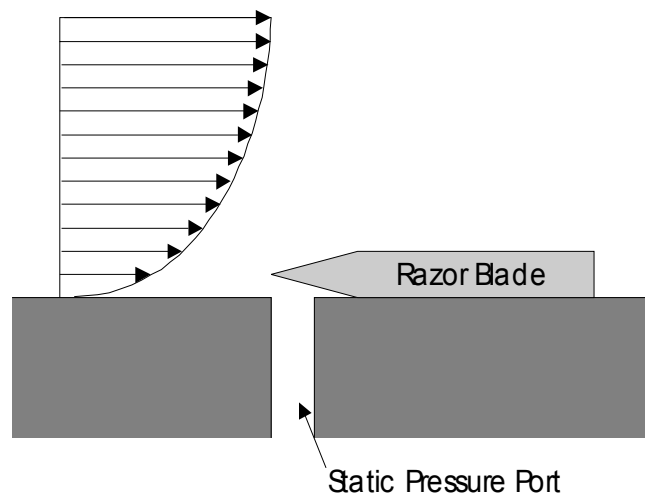


Figure 1-6. Schematic illustration of the Stanton tube method [7].

A non-intrusive method of obtaining skin friction measurements is using a surface hot-film (Fig. 1-5a). This technique relates skin friction through heat transfer by the Reynolds analogy [5],

$$St = Pr^{-2/3} \frac{C_f}{2} \quad (1-6)$$

where St is the Stanton number and Pr is the Prandtl number. The principle of this method uses the surface hot-film in a constant-temperature anemometer circuit to relate the heat loss via convection to a shear stress by a calibration [3]. The surface hot-film technique is useful in steady and dynamic flows if knowledge of the flow direction is not desired.

As illustrated there are many different indirect methods to measure wall shear. Each technique has certain advantages and disadvantages which lend themselves to particular flow environments. A more in-depth discussion on indirect measurement techniques can be found in Nitsche et al. [6]. Due to the great uncertainty associated with indirect measurement techniques, this type of approach for measuring skin friction was not investigated.

1.3.2 Method of Direct Measurement

Measuring wall shear directly involves replacing a portion of the surface by a sensing element mounted on a flexure. The flexure is weak in the direction of the flow so that it deflects easily, but strong orthogonally such that it resists the normal pressure forces. The sensing element is surrounded by a very small gap that allows for the necessary movement. This gap can be eliminated by filling it with some sort of liquid. When the fluid flows over this portion of the surface, it is exposed to a shear force. A measurement is made by either one of two methods: the sensing element is allowed to move once exposed to the shear load and then restored to its ‘null’ position by a restoring force or by allowing the floating element to move and recording the displacement of the element or the strain in the flexure. These two types of skin friction gages are known as “nulling” and “non-nulling”, respectively. For these methods to work one must first calibrate the sensor by simulating the expected range of shear levels and recording the response of the sensor. The most common method of calibration is hanging known

CHAPTER 1 – INTRODUCTION

masses on the sensing element and recording the displacement of the element or strain in the flexure (Fig. 1-7). By knowing the area of the sensing element that is exposed to the flow, the forces can easily be converted to shear values.



Figure 1-7. Illustration of point-load calibration technique [8].

Sensors classified as “nulling” comprise all gages where the floating element has a zero net displacement. This zero net displacement is made possible by a restoring force equal and opposite of the wall shear. By not allowing the floating element to have a net displacement, the flow field is virtually undisturbed, which is advantageous. However, a disadvantage arises from the restoring force being applied by a complicated mechanical system (Fig. 1-8). The complexity of the mechanical system lends itself to problems which affect the functionality and time response of the gage.

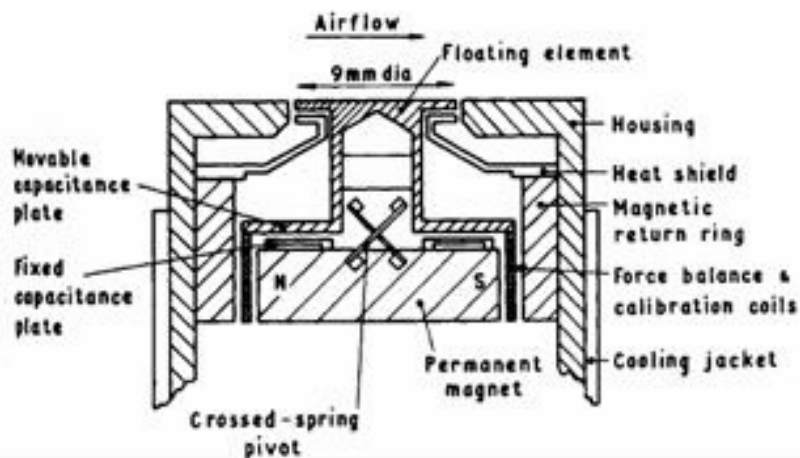


Figure 1-8. Schematic illustration of a “nulling” skin friction gage [9].

The second category of sensors mentioned is “non-nulling” skin friction gages. These sensors have a floating head which is free to displace when exposed to a shear force (Fig. 1-4). Once the shear force is removed, the head returns to its neutral position. There are two primary methods of measuring the shear level with this type of gage. The first uses strain gages attached to a flexure which bends when the floating element displaces. The second method is to measure the distance the floating element displaces. In both instances the gage has already been calibrated such that the measured strain or displacement correlates directly to a value for the shear stress. This type of gage is advantageous in that it does not have a complicated mechanical system providing a restoring force. However, since the floating head is allowed to displace the flow field can be slightly altered. This can be compensated for by designing the gage to have small enough movements so that any alteration in the flow is minimal.

1.4 Historical Overview of Direct Measurement Techniques

The direct measurement of drag dates back to 1892 when Froude used two large wooden planks in a towing tank to obtain the resistance through an extensive lever and spring system (Fig. 1-9). Over the last one hundred and fifteen years the direct measurement techniques have evolved and advanced the field of skin friction quantification. Gages have been designed for all most every imaginable type of flow condition. Table 1-1 summarizes the advances in skin friction gages; however it does not claim to be complete. The material presented is the date which the sensor came to existence, the flow conditions and type of gage, whether it measured one or two components of shear, head size, measurement method and gap filler.

CHAPTER 1 – INTRODUCTION

1872 Report British Assoc. 3712.

Experiments on Surface Friction: Dynamometric Apparatus.

Plate 2.

REFERENCES.

- A A Belt of Carriage
- B B Plane, the surface friction of which is to be recorded
- C C Horizontal beam carrying Plane and transmitting resistance of the same to spring, by means of Looped Conceiving line & h
- D D Curves fixed to beam CC by means of a
- E E Threaded nuts supporting beam CC
- F F Counterpoise to beam CC & c
- G G Lever arrangement for steadying the apparatus taking the strain off the spring while uniform speed is being obtained
- H H Spring extension of which measures resistance.
- K K Index Arm communicating extension of Spring to Cylinder
- W W Counterpoise to Index Arm
- L L Fulcrum of Index Arm, carried by bar b b

REFERENCES.

- M M Lever communicating extension of Spring to Index Arm.
- N Connecting Link, medium of communication of extension of Spring to Index Arm.
- O D Towing beam, holding fore end of Spring.
- P P Brass Cap, about which b b and M M hinge
- Q Q Bar ending head of Towing Beam and Cap P to frame Carrying Cylinder.
- R R Bell Crank for extending Spring by known weights hung on at c, thereby testing Scale.
- d d Connection of Bell Crank with Spring.
- e e Weight giving initial extension to Spring forming zero of Scale.
- S S Pen registering extension of Spring.
- U U Revolving Cylinder receiving paper on which is registered motion of Pen &c.
- T T Frame carrying Cylinder &c, capable of vertical adjustment.
- V V Time Pen worked by clock work.
- g g Gear for transferring motion of Carriage to Cylinder U U

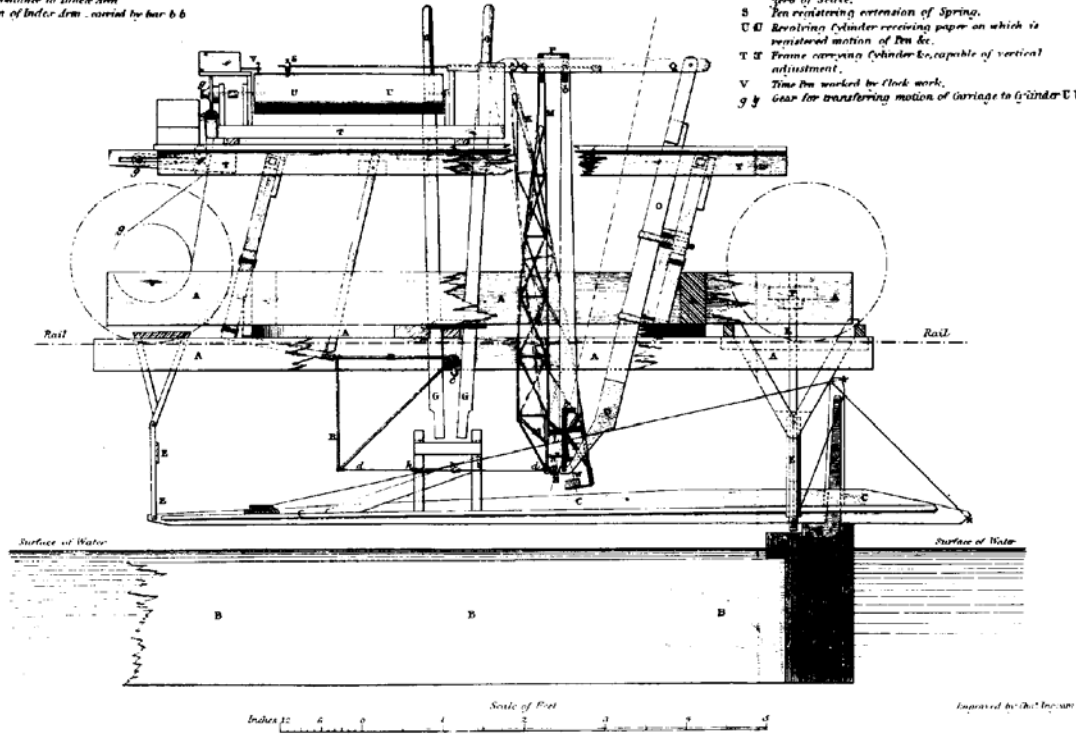


Figure 1-9. Illustration of test set up used by Froude to measure drag on wooden planks [10].

Table 1-1. List of history of skin friction gages [10-57].

YEAR	AUTHOR	TEST CONDITIONS	$\frac{2D}{3D}$	NULLING	HEAD SIZE (MM)	MEASUREMENT METHOD	GAP FILLER	NOTES
1872	Froude[10]	Planks in a Towing Tank	2D	No	482 mm wide with various lengths	Levers and springs	n.a.	Drag of whole plates
1929	Kemp[11]	Bottom of 77m pontoon $Re < 5 \times 10^8$	2D	Yes	309 x 1010	Pulleys and Springs	None	Measurements made in water
1932	Schoenherr[12]	"Catamaran Friction Plates" 0.3-3.0 ft/s $Re \sim 2 \times 10^6$	2D	Yes	914 x 457 to 1829 x 914	Hanging Weights	None	Towing tank with water or glycerin
1940	Schultz-Grunow[13]	$U=20$ m/s $1.6 \times 10^6 Re_x < 16 \times 10^6$	2D	Yes	300 x 500 (Estimated)	Manual Torsion Bar	None	Very Large

CHAPTER 1 – INTRODUCTION

1952	Weiler and Hertwig[14]	Supersonic Wind Tunnel	2D	Yes	25 Diameter (D)	Flexure with Linear Variable Differential Transformer (LVDT)	None	DRI University of Texas
1953	Chapman and Kester[15]	Subsonic and supersonic axial flow over cylinders	2D	Yes	Cylinder Length to Diameters of 8, 13, and 23	Transducer	None	Ames Lab NACA (Chapman and Kester, 1953)
1953	Coles[16]	$M=1.97$ $4 \times 10^5 < Re_x < 1 \times 10^7$ $M=2.57$ $4 \times 10^5 < Re_x < 9 \times 10^6$	2D	Yes	6 x 38	Parallel linkage flexure with Schaevitz LVDT	Oil	Figures 15-17 of (Coles 1952)
1953	Dhawan[17]	Low speed $6 \times 10^6 < Re_x < 6 \times 10^7$ Subsonic $0.2 < M < 0.8$ $3 \times 10^5 Re_x < 1.2 \times 10^6$	2D	Yes	12 x 63 2 x 20	Parallel LVDT	None	GALCIT "Correlation" Tunnel
1953	Eimer[18]	Hypersonic $M=5.8$ laminar flat plate with condensation	2D	Yes	51 x 25	Schaevitz LVDT Chemical balance and flexures	None	GALCIT-Hypersonic 5" x 5" Tunnel
1953	Hakkinen[19]	Turbulent boundary layer of flat plate at high subsonic to Mach 1.75 $3.3 \times 10^5 < Re_x < 1.2 \times 10^6$	2D	Yes	2 x 20	Schaevitz LVDT	None	GALCIT-Similar to Dhawan's Gage
1954	Blumer, Bradfield, and DeCoursin[20]	Axially symmetric conical turbulent boundary layer $M=2.6$ $1 \times 10^6 < Re_x < 8 \times 10^6$	2D	Yes	254 Long 15° Cone	Schaevitz LVDT	None	University of Minnesota, Rosemount Aeronautical Laboratory
1956	Wolff[21]	64 to 286 ft/s	2D	Yes	1006 x 749	Baldwin cantilever spring strain gages	None	University of Minnesota
1957	Lyons and Fenter[22]	Supersonic Flight	2D	Yes	50 (D)	Double Parallel inter-connected linkage to eliminate sensitivity to linear and rotational accelerations	None	Tested on Rockets
1958	Everett[23]	Incompressible liquid flow with variable channel height	2D	Yes	25.4 and 25.15 (D)	Beryllium-copper flexure Schaevitz LVDT	Silicon Fluid	Variable gap size and thickness
1958	Smith and Walker[24]	$0.11 < M < 0.32$ $10^6 < Re_x < 40 \times 10^6$	2D	Yes	50 (D)	Parallel linkage LVDT Kelvin current balance	None	
1963	MacArthur[25]	Shock Tunnel/Impulse Facilities	2D	Yes	6.4 (D)	Parallel linkage lead zirconium titanate piezoelectric ceramic	None	Acceleration load compensation. No static calibration. 5 kHz.
1963	Moulic[26]	$M=6$ Low Density	2D	Yes	0.25 x 25	Side flexure pivot LVDT	None	Studied strong interaction region near leading edge of flat plate
1964	O'Donnell[27]	$M=2.67$ $Re=100070$	2D	Yes	25 (D)	Parallel linkage	None	Studied effects of misalignment of floating head
1965	Young and Westkaemper[28]	Supersonic flow with heat transfer and surface roughness	2D	Yes	25 (D)	Parallel linkage	None	
1966	Dershin <i>et al.</i> [29]	Supersonic flow with mass transfer	2D	Yes	"Pointed ellipse"	Parallel linkage LVDT	None	
1966	Moore and McVey[30]	High temperature hypersonic flows	2D	Yes	N/A	Flexure pivot Pneumatic position sensor	None	
1969	Brown and Joubert[31]	Low-speed adverse pressure gradients	2D	Yes	19 (D)	Parallel Linkage LVDT	None	Studied gradient forces in gap

CHAPTER 1 – INTRODUCTION

1969	Fowke[32]	Supersonic	2D	Yes	127 (D)	Flexure pivot LVDT	None	
1969	Bruno, Yanta and Risher[33]	Supersonic flows with heat transfer	2D	Yes	20.3 (D)	Flexure pivot LVDT	None	Force variable by changing loading spring
1970	Winter and Gaudet[34]	$0.2 < M < 2.8$ $1.6 \times 10^7 < Re_x < 2 \times 10^8$	2D	Yes	368 (D)	Parallel linkage Resistance strain gages	None	Surface roughness tests
1970	Hastings and Sawyer[35]	$M=4$ $1 \times 10^7 < Re_x < 3 \times 10^7$	2D	Yes	7.9 (D)	Parallel Linkage LVDT	None	
1970	Paros (Kistler)[36]	Used in a wide range of conditions including flight. Cooling system available	2D	Yes	9 (D)	Pivoted about crossed-spring flexure	None	Schematic Figure 4 of Winter (1977)
1971	Miller[37]	Low speed flow with a favorable pressure gradient	2D	Yes	25 (D)	Parallel Linkage LVDT	None	Extension of Brown and Joubert (1961)
1973	Franklin[38]	Subsonic wind tunnel and water	2D	Yes	16 (D)	Pivoted variable geometry electric valve	None	
1973	Waltrup and Schetz[39]	Supersonic flow with a strong adverse pressure gradient $M=2.4$	2D	Yes	25.4 (D)	LVDT	None	VT Supersonic Wind Tunnel (VT-SST) Gage design of Ref. [24]
1974	Morsy[40]	Low speed flow past circular cylinder	2D	Yes	50.1 x 3.2	Jeweled pivots clock springs	None	
1980	Frei and Thomann[41]	Low-speed, $M < 0.25$	2D	No	10 mm wide ring in a 200 mm tube	Piezo-ceramic beam	Oil	Specially developed of pressure gradients
1980	Allen[42]	$M=2.16$	2D	Yes	127(D)	Parallel linkage	No	Study of errors from misalignment and gap size e
1977-84	Schetz and Nerney[43], Kong and Schetz[44], Collier and Schetz[45]	Low-speed, turbulent flow over smooth, rough and porous surfaces with injection through the head	2D	No	25.4(D)	Semi-conductor strain gages	None	
1990	Deturris, Hellbaum, and Schetz[46]	Hot high speed flow $M=3$ $T=1667$ K	2D	No	12.7 (D)	Semi-conductor strain gages (DSC sensor)	Silicon oil	Housing cooled with water
1992	Kelly, Simmons, and Paul[47]	Impulse test in hypersonic flow	2D	No	10 (D)	Piezoelectric transducers	Thermal cover	No static calibration
1993	Chadwick, DeTurris, and Schetz[48]	Very High Heat Flux $M=10-12$ $T_w=4500$ K	2D	No	6.35 (D)	Semi-conductor Strain Gages	Silicon Oil	Housing and head cooled with water
1995	Bowersox, Chadwick, Diewert, and Schetz[49]	Impulse tests $M=14$ NASA Ames 16" Shock Tunnel $T=2.0$ milliseconds Hypulse Facility $T=0.3$ milliseconds	2D*	No	8.13 (D)	Semi-conductor strain gages	Silicon Oil	Plastic head, beam and housing. 10 kHz. *Can be extended to 3D.
1995	Paik and Schetz[50]	Supersonic flow with heat flux $M=2.4$ $T_w=300$ $Re_x=4.9 \times 10^7$	2D	No	12.7 (D)	Foil Strain Gages	None	Water cooled with heat flux micro-sensor on head
1996	Novean, Bowersox, and Schetz[51]	Shock Tunnel $M=12-14$, 200-3000 Pa, Hypulse $M=14$, 800-3000 Pa	2D*	No	4.55, 4.6, and 5.4 (D)	Semi-conductor strain gages	Silicon oil or rubber RTV615	40 kHz. *Can be extended to 3D.

CHAPTER 1 – INTRODUCTION

1999	Remington and Schetz[52]	Supersonic, Mach 2.4	2D	No	4.2, 6.35, and 9.53 (D)	Kistler-Morse Strain gages	None	Magnetic damping
1999	Pulliam and Schetz[6]	Supersonic Flow	2D	No	1.63 (D)	Fiber Optic Displacement Sensors	None	Sensitive to vibration
2001	Smith and Schetz[3]	M=2.4 T ₀ =300k Scramjet Engine Model M=6.4 T ₀ =1555 K	2D	No	7.6 (D)	Flexure Ring with Metal Foil Strain Gages	None	No cooling and could operate for about 4-5 secs. without thermal effects
2002	Magill et al [53]	Mach 2.4	2D	No	3(D)	Semi-conductor strain gages	This RTV sheet over head and gap	Rubber sheet provided good damping
2002	Sang and Schetz[54]	Supersonic flow M=2.4 T ₀ =300k Transonic Flight Test (F-15)	3D	No	19 (D)	Aluminum Flexure Rod with Semiconductor Strain Gages	Thin Silicon RTV Sheets w/ or w/o Glycerin Fill	Flight Test Gage Used Only RTV Sheet for Damping. Sensitive to temperature
2002	Goldfeld, Nestoulia, and Falempin[55]	Supersonic Flow Mach 2, 4, 6 Re _x =2.5-10x10 ⁶	3D	No	6-10 (D)	Semiconductor resistive-strain Sensors	Rubber Damper to Isolate the Gage from the Tunnel and Fill Oil	
2002	Goynne, Stalker and Paull[56]	Mach 6.6 in a shock tunnel	2D	No	1(D)	Piezo-ceramic disk	Felt wafer	Upgrade of Ref. [37] gage. 40 kHz. No static calibration
2004	Orr, Schetz and Fielder[57]	Supersonic Flow, Mach 2.4 and 4 at high Re	3D	No	25.4(D)	Flexure rings with both Fiber-Optic displacement and Foil Strain gage sensors	None	Good Agreement between both types of sensors and predictions

1.5 Motivation for Small Skin Friction Gage

By knowing the skin friction distribution of an aerodynamic body, problem areas in the design become visible and can be corrected. As mentioned previously, analytical models and indirect measurement techniques are not of interest because of the large uncertainties associated with each method. This leaves the method of direct measurement as the primary technique to obtain skin friction data. The motivation for the design of a small skin friction gage lies in the desire for a truly local measurement needed to obtain a skin friction distribution and also to implement flow control, which is an emerging field of interest to practicing engineers. It is acknowledged that other gages have been designed with this in mind (MEMS); however severe implications arise in the calibration and validation of these types of gages [8].

New difficulties arise when the size of a skin friction gage is to be scaled down. The first and most salient complication of producing a gage capable of making truly localized shear measurements is the machining of such a device. With the need for the

CHAPTER 1 – INTRODUCTION

scale of the flexures to be less than the tolerances of the machines themselves, there is not a cost efficient way to fabricate such parts. A method of obtaining small scale (microns) silicon flexures is available, however the high tensile strength and small region of elastic deformation is not desirable. There is a need for a flexure composed of a material with a high modulus of elasticity capable of elastic deformation whose size can be controlled. This leads to the concept of applying carbon nanotubes to a skin friction gage.

Carbon nanotubes are sheets of graphene rolled into circular cylinders with diameters of approximately 50 nm and lengths ranging from 10 – 20 microns. They possess mechanical properties which lend themselves to a structural application. The modulus of elasticity of a carbon nanotube is on the order of a teraPascal. Nanotubes have the ability to significantly alter their shape due to external forces without irreversible atomic arrangement [58]. These tubes are man-made structures with heights and diameters controlled within the growth technique. The application of carbon nanotubes as a flexure for a skin friction gage has not previously been attempted. In order to successfully design, fabricate and test such a device, this research targeted localized skin friction measurements of two-dimensional, steady flow over surfaces with relatively large radius of curvature ($> 1\text{m}$) for an initial trial.

1.6 Outline

The remainder of this report will proceed as follows: Chapter 2 informs the reader of the background of carbon nanotubes. Chapter 3 investigates utilizing a freestanding array of nanotubes as a skin friction sensor. The concept of using carbon nanotubes in a table top arrangement is explored in Chapter 4. Chapter 5 consists of the fabrication, integration, and calibration of the table top prototype. The supersonic wind tunnel testing is presented in Chapter 6, and conclusions and recommendations for future work can be found in Chapter 7.

2 CARBON NANOTUBES

2.1 Background

Carbon nanotubes have been the subject of intense research since their accidental discovery in 1991 by the Japanese scientist Sumio Iijima. The discovery was made experimenting with techniques (arc evaporation synthesis) scientists used to create C_{60} molecules (Fig. 2-1). Iijima passed electrical sparks between two closely spaced graphite rods [59]. He vaporized the graphite rods and allowed the carbon to condense into soot. When Iijima examined the carbon soot under the microscope, he found tubes of many-layered carbon known now as multi-walled nanotubes (MWNTs).

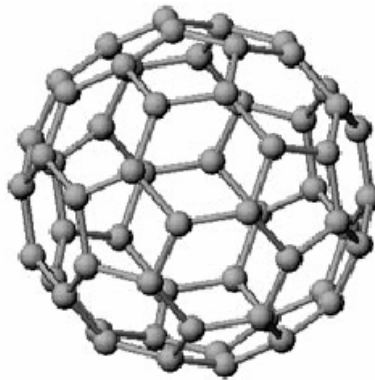


Figure 2-1. Bucky Ball structure of C_{60} [60].

There are two types of carbon nanotubes; single-walled nanotubes (Fig. 2-2) and multi-walled nanotubes (Fig. 2-3). Single-walled nanotubes (SWNTs) consist of a single graphene sheet formed in a tubular shape, and they typically have diameters ranging from 1 to 5 nm. MWNTs are composed of many layers (up to 50) of concentric graphene sheets [61]. The outer diameter of a multi-walled nanotube can range from several nanometers to several hundreds of nanometers. The inner diameter depends on the number of coaxial tubes composing the MWNT. The lengths of single and multi-walled nanotubes vary depending on the technique by which they are grown.

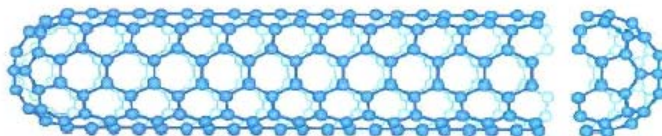


Figure 2-2. Computer model of a single-walled nanotube (SWNT) [61].



Figure 2-3. A computer generated model of a telescopically extended MWNT [60].

Single-walled nanotubes can be classified as either armchair, zigzag or chiral depending on the geometry of the carbon atoms. The chiral vector, $\overline{OA} = n\overline{a}_1 + m\overline{a}_2$, is defined on the hexagonal lattice of carbon atoms where n and m are integers, and \overline{a}_1 and \overline{a}_2 are unit vectors (Fig. 2-4).

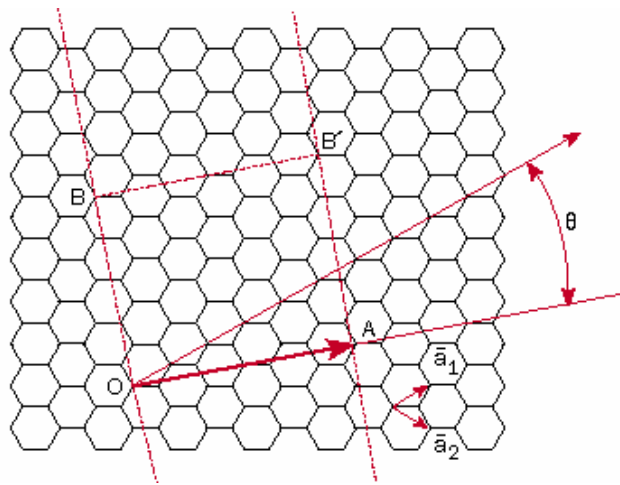


Figure 2-4. The chiral vector \overline{OA} defined by unit vectors \overline{a}_1 and \overline{a}_2 . The chiral angle θ with respect to \overline{a}_1 ($\theta=0^\circ$) [62].

The chiral angle θ is given by Eqn. (2-1) [62].

$$\theta = \tan^{-1} \left[\frac{\sqrt{3}n}{2m+n} \right] \quad (2-1)$$

A nanotube, for which the integer n equals m , is considered an armchair nanotube. Using Eqn. (2-1) it follows that $\theta = 30^\circ$ for an (n, n) armchair nanotube. The classification as a

CHAPTER 2 – CARBON NANOTUBES

zigzag nanotube is given when $m = 0$ and is denoted as a $(n, 0)$ zigzag nanotube. In this case $\theta = 0^\circ$. For all other values of n and m where $n > m$, the nanotube is known as a (n, m) chiral nanotube, with $0^\circ < \theta < 30^\circ$ (Fig. 2-5).

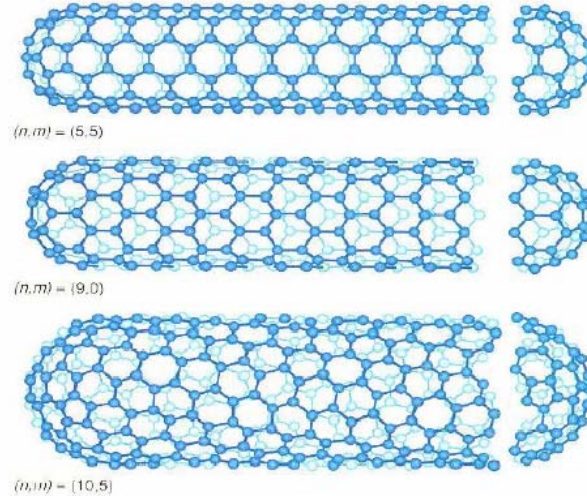


Figure 2-5. Computer models of the three types of single-wall nanotubes. (top) (5, 5) armchair nanotube, (center) (9, 0) zigzag nanotube, (bottom) (10, 5) chiral nanotube [61].

The three different types of SWNTs can either be metallic or semi-conducting depending on the values of the integers n and m . If $(n + m) = 3i$, where i is any integer, the nanotube behaves as a metal, otherwise it behaves as a semiconductor. Figure 2-6 illustrates that all armchair nanotubes are metallic, while zigzag and chiral nanotubes may be metallic or semi-conducting depending on the chiral vector.

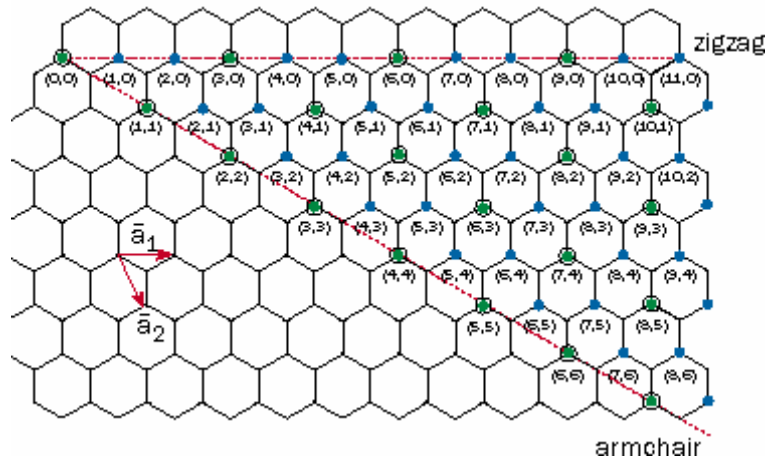


Figure 2-6. Diagram of possible chiral vectors specified by pairs of integers (n, m) for carbon nanotubes (Green encircled dots dictate metallic nanotubes, blue dots dictate semi-conducting nanotubes) [62].

2.2 Properties of Carbon Nanotubes

Since the discovery of carbon nanotubes, quantifying the mechanical and electrical properties has become a major focus of research. Quantifying these properties is difficult due to the sub-micron size and variable geometry of nanotubes. An agreement upon exact values has not been established. The parameters of primary interest here are the Young's modulus, the nominal electrical resistance of MWNTs and the change in resistance under stress.

2.2.1 Mechanical Properties

Theoretical calculations have been made which predict nanotubes have a modulus of elasticity between 1 TPa and 5 TPa [63]. The large range of values can be attributed to each author's interpretation of wall thickness and separation distance between walls. The thicker the walls are assumed to be, the lower the value of the modulus.

Various attempts have been made to obtain experimental values for the mechanical properties of multi-walled carbon nanotubes [64-68]. Wong *et al.* [64] measured the mechanical properties of individual MWNTs using atomic force microscopy (AFM). The bending force was measured along the unpinned tube by moving the AFM tip from left to right, causing the nanotube to apply a lateral force to the tip (Fig. 2-7). The mean measured value of the elastic modulus was 1.28 ± 0.5 TPa with no dependence on nanotube diameter [64].

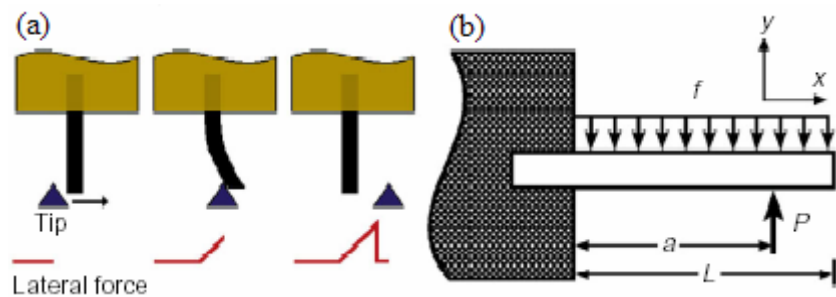


Figure 2-7. (a) Schematic of beam bending using AFM. The AFM tip (blue triangle) moves in the direction of the arrow and the corresponding lateral force (red) is shown. (b) Schematic of a pinned beam with distributed friction force f . Force P exerted on the AFM tip at a distance a , from pinned end [64].

A different technique was used to find the modulus of elasticity by researchers at NEC in Princeton and the University of Illinois in 1996 [65]. They analyzed the

thermally excited vibrations measured in a transmission electron microscope (TEM) which yielded a Young's modulus of 1.8 ± 1.4 TPa. This measurement technique contains a large statistical error, questioning the validity of the result. In 1998, Treacy *et al.* [66] used a similar TEM technique as in 1996, and found the elastic modulus to be 1.25 TPa. This more closely matched the value found by Wong *et al.* and is the value many have assigned to the Young's modulus of a MWNT.

2.2.2 Electrical Properties

Quantifying the electrical properties of MWNTs has been equally as difficult as measuring the mechanical properties, because MWNT are such complex conductors. Any given shell in a MWNT is geometrically unique from its neighbors, making each tube electrically distinguishable from the next [69]. In addition to this, there is not a fundamental agreement on how many tubes in a MWNT contribute to the electrical transport. Some researchers believe only the outermost shell is responsible for the electrical transport, while others believe the electrical transport depends on how the nanotubes are contacted.

Recently, Collins *et al.* [69] came up with an electrical procedure to dismiss the theory that only the outermost nanotube is responsible for electrical transport. The procedure destructively removes the outermost carbon shell from a MWNT via current-induced oxidation. By repeating this procedure all the shells of a MWNT can be removed one at a time. This allows for both the electrical characterization of each shell of a MWNT and quantifying how many shells contributed to room temperature conductance. It was estimated that shells of the nanotube exhibiting zero barrier, ohmic characteristics contribute to room temperature conductance. Using a typical device to obtain electrical measurements of MWNTs (Fig. 2-8), Collins [69] found the nanotube resistances range from 5 to 15 k Ω .

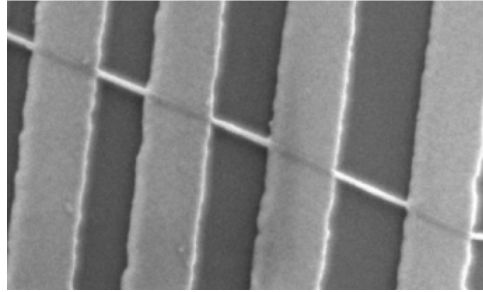


Figure 2-8. SEM image of a typical MWNT electrical device [69].

Another method to measure the conductance of a single MWNT has been carried out by Frank *et al.* [70]. A single MWNT replaces the tip of a scanning probe microscope, which can be lowered into a liquid metal (e.g. mercury) to establish an electrical contact. The nanotube is immersed and pulled out of the liquid metal several times to remove graphite particles from the tube. The conductance of arc-produced MWNTs with typical lengths of 4 microns and diameters of 15 nanometers was found to be one unit of the conductance quantum $G_o = 2e^2/h = 1/12.9 \text{ k}\Omega^{-1}$ [70]. This value falls in the range of 5 to 15 k Ω found by Collins.

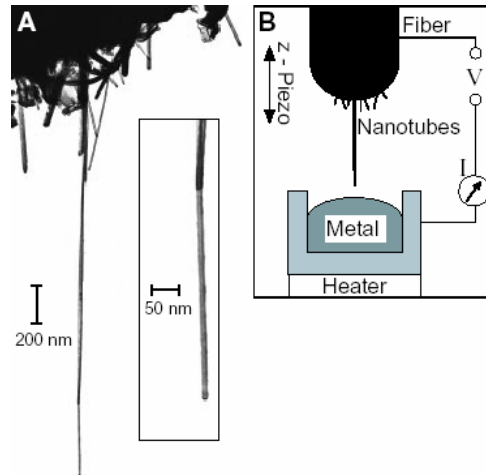


Figure 2-9. (A) Transmission electron micrograph of one single MWNT extending from the end of a nanotube fiber. (B) Schematic diagram of apparatus used to contact nanotubes to liquid metal [70].

2.2.3 Electromechanical Properties of SWNTs

The effects of mechanical deformation on the electrical properties of carbon nanotubes have been studied both theoretically and experimentally [71]. Depending on the chirality of a single-walled nanotube, when subjected to bending, the conductance can

decrease significantly. This result is due to simple stretching of the nanotube which opens an energy gap at the Fermi surface that turns the nanotube into a semiconductor, thus decreasing its conductance [71]. To achieve large changes in the conductance the chirality must be such that the nanotube is classified as a metallic zigzag nanotube. These tubes are represented as $(3n, 0)$ zigzag nanotubes, where n is any integer.

Theoretical calculations of the conductance drop of single-wall nanotubes have been obtained by Maiti *et al.* [72]. The group performed conductance calculations of two types of bending to compare the conductance drop of an armchair nanotube and a metallic zigzag nanotube (Fig. 2-10). The first calculation was done to simulate an AFM-tip-deformation on a 2400 atom nanotube. The AFM-tip was modeled as a 15 atom Li needle initially aimed at the center of a hexagon in the middle of the tube. By displacing the Li needle a distance δ , the deformation angle could be calculated as $\Theta = \tan^{-1}(2\delta/L)$, where L is the undeformed length of the nanotube. To simulate bending, the two halves of the nanotube are rotated in equal and opposite angles about an axis perpendicular to and through the center of mass of an initially straight nanotube.

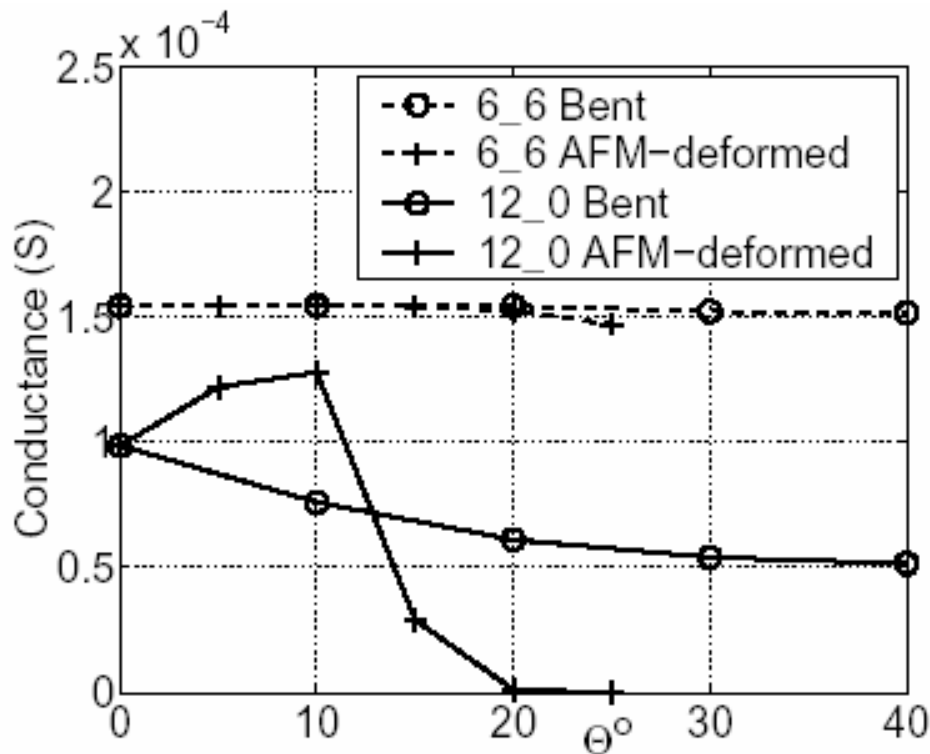


Figure 2-10. Conductance of armchair (dashed) and zigzag (solid) nanotubes under bending (circle) and AFM-tip deformation (cross) as a function of deformation angle [72].

CHAPTER 2 – CARBON NANOTUBES

Figure 2-10 displays that when a $(12,0)$ zigzag nanotube is subjected to a deflection angle of 25 degrees the conductance drop is more than four orders of magnitude.

Experimental results validated the theoretical predictions that large conductance drops can occur when a metallic zigzag nanotube is deformed. Tombler *et al.* [71] performed experiments which measured the change in conductance of SWNTs under mechanical deformation. The experiments were carried out using an AFM tip to deflect a suspended SWNT such that the deformations were reversible and the contact resistance was not altered (Fig. 2-11).

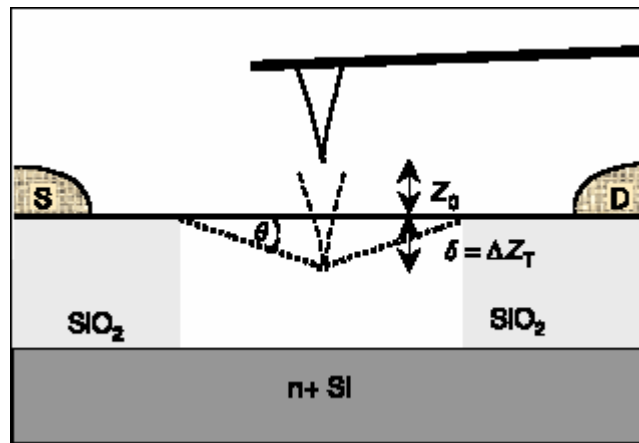


Figure 2-11. Schematic illustration of AFM tip deflection of SWNT [71].

The deflection angle in Figure 2-11 is found in the same manner as above. By displacing the AFM tip a distance ΔZ_c , the deformation angle could be calculated as $\theta = \tan^{-1}(2\Delta Z_c / L)$, where L is the undeformed length of the nanotube. Figure 2-12 displays the results of experiments. The vertical distance and corresponding deformation angle are displayed over the conductance drop. Figure 2-12c shows a conductance drop of two orders of magnitude when the deformation angle equals approximately 14 degrees.

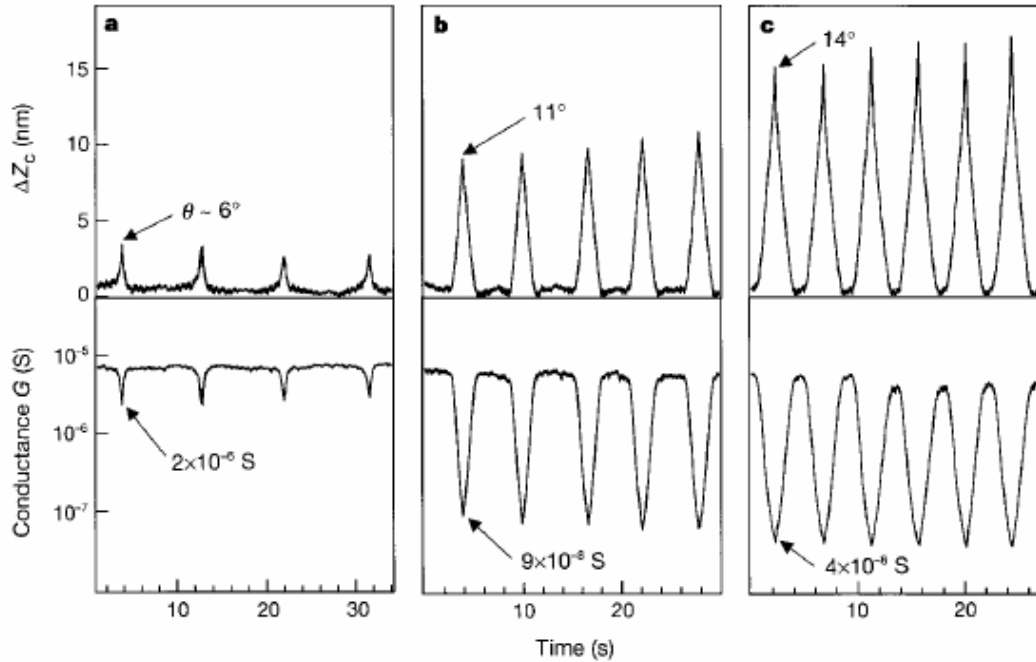


Figure 2-12. Experimental results of cyclic conductance drop due to AFM tip deformation [71].

2.3 Growth Techniques of MWNTs

Multi-walled nanotubes can be grown by a variety of methods depending on the desired product. These fabrication methods include, but are not limited to: carbon arc or arc-discharge, laser ablation or pulsed laser vaporization (PLV), and chemical vapor deposition (CVD). A short summary of each growth technique will follow.

Carbon arc, or arc-discharge, is a method in which carbon atoms are evaporated by a plasma of Helium gas that is produced by high currents passed through opposing carbon anode and cathode. This technique is capable of the production of high quality MWNTs and SWNTs by controlling the growth conditions, such as the pressure of the Helium and the arcing current (Fig. 2-13). MWNTs with lengths on the order of ten microns and diameters of 5-30 nm can be grown by this method [73].

Pulsed laser vaporization is a fabrication method used for producing SWNTs by evaporating a carbon target via a laser. The carbon target is placed in a tube-furnace which is heated to approximately 1200°C. During laser ablation, an inert gas is passed through the growth chamber to carry the SWNTs to a collector tip outside of the furnace.

CHAPTER 2 – CARBON NANOTUBES

The product is typically ropes of tens of individual nanotubes held together by van der Waals interactions [73].

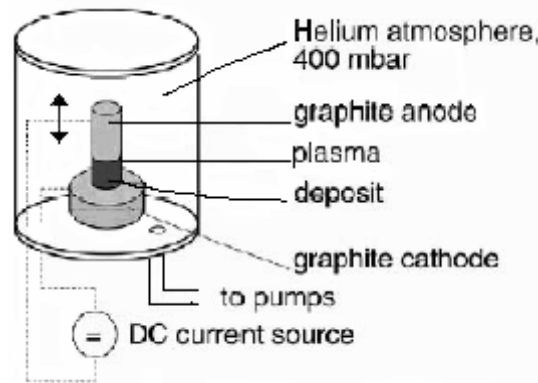


Figure 2-13. Schematic illustration of arc-discharge method [74].

Chemical vapor deposition methods have been in use for 10 – 20 years, successfully making carbon fiber, filaments and nanotube materials [73]. The method of using CVD for the growth of nanotubes involves heating a catalyst material to high temperatures (550 – 750°C) in a tube furnace and flowing hydrocarbon gas through the tube reactor (Fig. 2-14). The materials grown over the catalyst are collected when the system is cooled to room temperature. This procedure is capable of the growth of aligned arrays of MWNTs (Fig. 2-15) and bundles of SWNTs, but these tubes have high defect densities. While the nature of the defects is not thoroughly understood, one speculation is that the growth temperature is too low to provide sufficient thermal energy to anneal the tubes in to perfect structures [73].

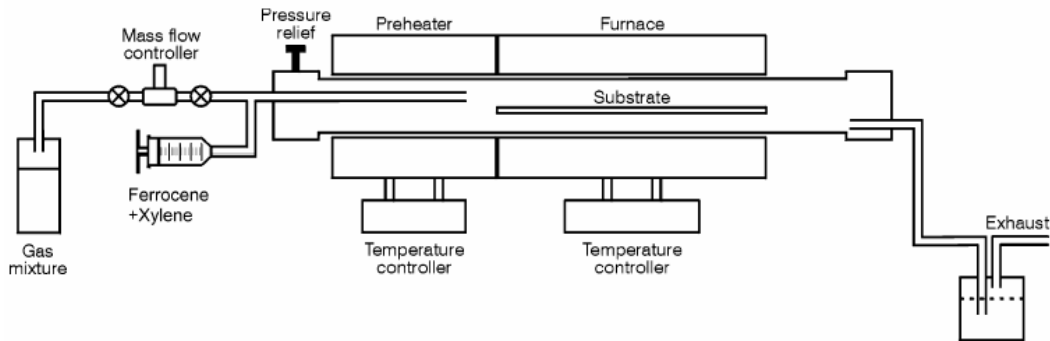


Figure 2-14. Schematic of CVD growth process [75].

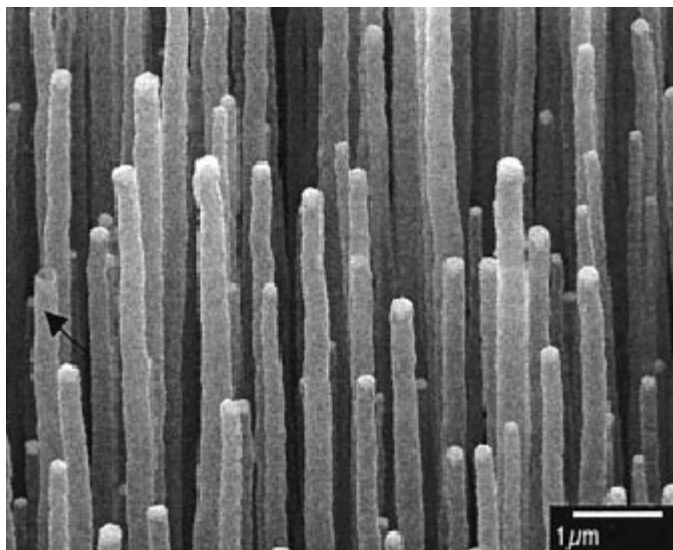


Figure 2-15. Scanning electron microscopy image of an array of aligned nanotubes [76].

3 FREESTANDING ARRAY OF MWNTS AS A C_f GAGE

3.1 Freestanding MWNT

The growth of multi-walled carbon nanotubes in structured arrays is of particular interest in designing an ultra-small gage to measure skin friction. If a freestanding nanotube is subjected to a velocity profile, a deflection will be induced by the resistive force, drag. Two possible techniques were explored which utilize the deflection of the nanotubes as the primary method of measuring skin friction. The first measurement technique is an electro-optical method which measures the change in the phase angle of the reflection coefficient of the nanotubes. The second method is a purely electrical method which uses a possible change in the resistance of the nanotubes when they are deflected.

3.1.1 Fluid Dynamics

A skin friction sensor using MWNTs was conceptually designed to measure wall shear in a flow of Mach 2.4. A suitable representative value of wall shear at this flow speed in the Virginia Tech Supersonic wind tunnel is approximately 250 Pa. The representative case in which the sensor would be tested is to measure the skin friction at a location on a flat plate. This case was crudely analyzed to quantify the boundary layer characteristics.

The Reynolds number for flow over a flat plate at Mach 2.4 is found using NACA 1135, Chart 25. The total temperature and total pressure for a typical test run at Mach 2.4 in the Virginia Tech Supersonic wind tunnel are 285 degrees Kelvin and 50 psia. Using these values, Re/l is found to be approximately $3.8 \times 10^7 \text{ m}^{-1}$. Multiplying this value by the length of the flat plate to the measurement location (15 cm) gives $Re_l \approx 5.7 \times 10^6$.

The calculated value of Re_l is greater than the typical transition Reynolds number for flow over a flat plate ($Re_{trans} \approx 2.5 \times 10^5$). This indicates that the boundary layer is turbulent in the vicinity of the analysis. This has been confirmed by past experiments in the supersonic wind tunnel [3,6,57].

The turbulent boundary layer consists of three main layers. The innermost region adjacent to the wall is known as the laminar sublayer (LSL) and constitutes

approximately $1/1000^{\text{th}}$ of the total boundary layer height. The flow in this region is assumed incompressible since $M < 0.3$. The inner region begins where the laminar sublayer ends and occupies approximately $1/10^{\text{th}}$ of the total height. The outer region begins at an unspecified point in the inner region and occupies the remaining length of the boundary layer. The region which the inner and outer layers share is called the overlap region [5].

The LSL is the region of the boundary layer of primary concern when analyzing the fluid dynamics around a freestanding nanotube. In this region the length and velocity scales are ν/u_* and u_* respectively [5]. These quantities are represented in Eqn. (3-1) and (3-2).

$$y^+ \equiv \frac{yu_*}{\nu} \quad (3-1)$$

$$u_* \equiv \sqrt{\frac{\tau_w}{\rho}} \quad (3-2)$$

where y is the vertical location in the LSL, τ_w is the wall shear, and ρ is the density of air. The length scale y^+ at the edge of the LSL ranges from 5 to 7 [5]. Using a value of y^+ in this range, a wall shear value of 250 Pa, and the kinematic viscosity at room temperature, Eqn. (3-1) can be solved for the height of the laminar sublayer, y_{LSL} . This value falls in the range of 5 – 8 microns. This height was calculated to enforce a length constraint on the nanotube such that it would stand entirely in the LSL region and simplify the fluid dynamics. Using the conservative estimation of $y_{LSL} \approx 5 \mu\text{m}$ the length of the nanotube used in the analysis is 5 microns.

In the region close to the wall, it can be assumed that $\tau = \tau_w$. From this assumption the velocity profile can be obtained by solving Eqn. (3-3) for $U(y)$.

$$\tau_w = \mu \frac{\partial U}{\partial y} \quad (3-3)$$

Integrating with respect to y yields

$$U(y) = \frac{\tau_w}{\mu} y \quad (3-4)$$

Substituting the values of wall shear and dynamic viscosity of air at room temperature yields the linear velocity profile $U(y) \approx 1.4 \times 10^7 y$. This velocity is a function of height and is valid for the entire height of the laminar sublayer region.

The flow regime of a single MWNT in the laminar sublayer region of the boundary layer can be quantified by the Reynolds number,

$$Re_D \equiv \frac{\rho U D}{\mu} \quad (3-5)$$

where D is the diameter of the nanotube. The range of the Reynolds number corresponds to the range of velocities since $\rho = const$. Using the velocity function, $U(y)$, the velocity is zero at the wall and increases linearly to approximately 68 m/s at the nanotube tip, where $y = 5 \mu\text{m}$. The Reynolds number of a nanotube with $D = 50 \text{ nm}$ in the range of velocities mentioned above is $0 < Re_D < 0.22$ (Fig. 3-1a).

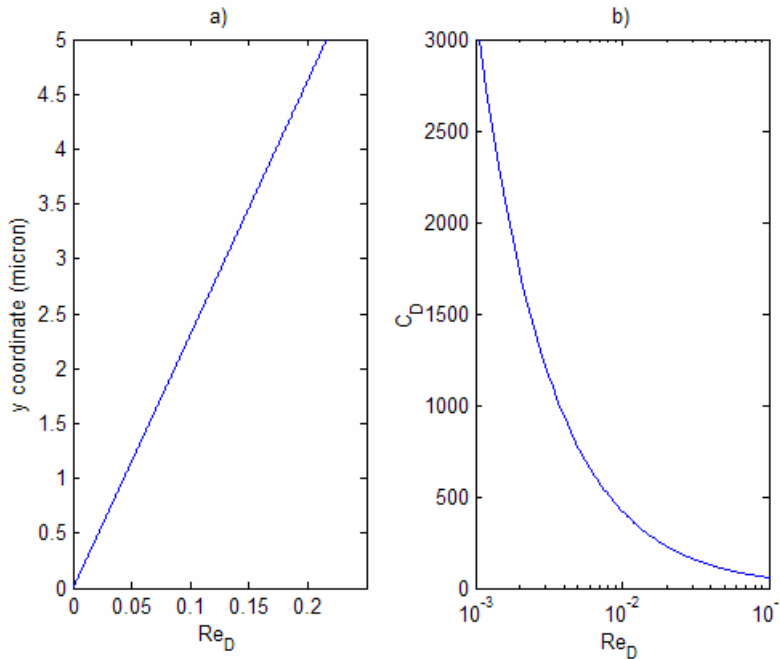


Figure 3-1. a) Plot of Reynolds number as a function of the y coordinates of a cylinder of $D = 50\text{nm}$. b) Plot of Reynolds number as a function of the drag coefficient of a circular cylinder (Eqn. 3-4).

The analysis of the fluid dynamics on a nanotube is now constrained to the non-separation regime where $0 < Re_D < 4-5$ [77]. In this regime the drag varies directly with velocity and thus directly with Re_D . In 1975 Sucker and Brauer [78] developed a

curve-fit formula (Eqn. 3-8) for the drag coefficient of a circular cylinder of infinite length, normal to the flow, as a function of Re_D . This formula is valid with good accuracy for $10^{-4} < Re_D < 2 \times 10^5$.

$$C_{D_{cyl}} \approx 1.18 + \frac{6.8}{Re_D^{0.89}} + \frac{1.96}{Re_D^{0.5}} - \frac{0.0004 Re_D}{1 + 3.64 \times 10^{-7} Re_D^2} \quad (3-6)$$

Equation (3-6) provides a method of obtaining a drag coefficient for the various Reynolds numbers of this flow. To ensure Eqn. (3-6) is not violated, the corresponding y -coordinate to the lower bounds of Re_D is found to be $y \approx 6$ nm. The drag below this y -coordinate is very small compared to the y stations above and thus is neglected without consequence. Figure 3-1b shows the relationship between Reynolds number and the drag coefficient for the range $10^{-3} < Re_D < 0.1$ for a circular cylinder with $D = 50$ nm (representative of a nanotube).

As previously mentioned Eqn. (3-6) gives the drag coefficient of a cylinder of infinite length normal to the flow as a function of Re_D . Due to the velocity gradient present in the laminar sublayer it is necessary to treat the cylinder as composed of many elements such that the Reynolds number of each element is constant. For this analysis the cylinder has been broken into 100 elements. The drag can then be calculated using:

$$D = \frac{1}{2} C_D \rho U^2 S \quad (3-7)$$

where S is the cross sectional area per unit length on which the drag acts. For our purpose, the drag was calculated per unit length so as to normalize the drag values of each element. The drag of each element was summed to obtain the total drag on the cylinder. The cylinder was split into a sufficient number of elements such that the total drag converged to a constant value of approximately 9.6 nN. The load intensity, q_o as a function of vertical coordinate of the nanotube is shown in Figure 3-2. For the purpose of subsequent analysis the load distribution is assumed to be linear.

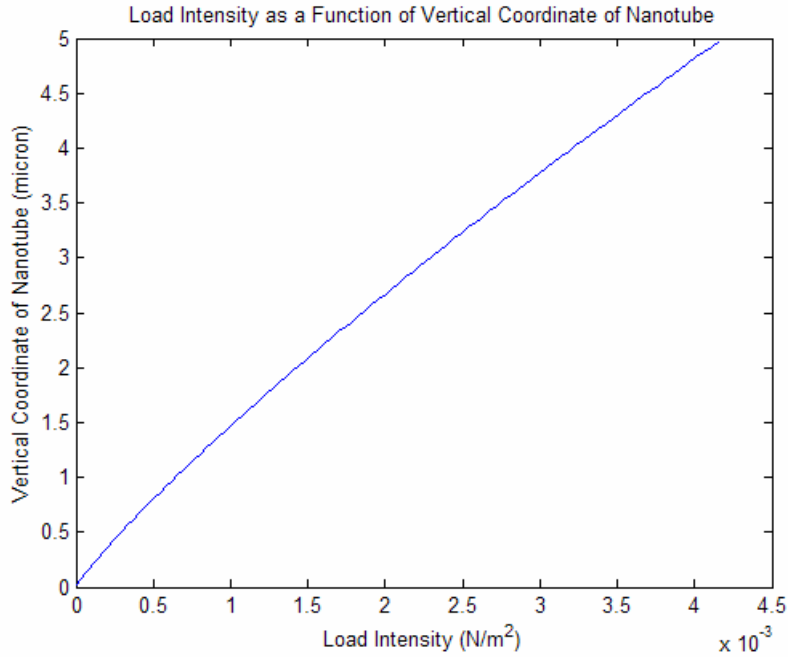


Figure 3-2. Plot of the load intensity as a function of vertical coordinate of a cylinder ($D=50nm$, $L=5\mu m$.)

3.1.2 Analytical Design

Once the load intensity over the length of the nanotube was calculated, the analytical solution of bending angle and deflection could be obtained using linear beam theory. Figure 3-3 is a schematic of a beam with a linearly distributed load and coordinate system used in the beam mechanics.

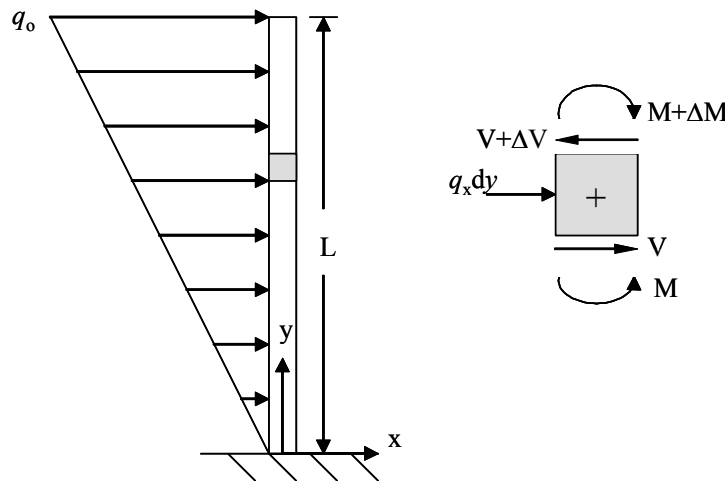


Figure 3-3. Schematic of a beam with distributed load and definition of the coordinate system.

From Figure 3-3 the differential equation for the shear can be obtained.

$$\frac{dV}{dy} - q_x = 0 \quad (3-8)$$

where $q_x = q_o \frac{y}{L}$. Integrating with respect to y and applying the boundary condition, $V=0$ at $y=L$ to solve for the constant, the shear force $V(y)$ is obtained.

$$V(y) = \frac{q_o}{2L}(y^2 - L^2) \quad (3-9)$$

From Figure 3-3 the differential equation for the moment can be obtained.

$$\frac{dM}{dy} - V(y) = 0 \quad (3-10)$$

Integrating again with respect to y and applying the boundary condition $M=0$ at $y=L$ to solve for the constant gives the moment $M(y)$.

$$M(y) = \frac{q_o}{6L}(y^3 - 3yL^2 + 2L^3) \quad (3-11)$$

The slope (v') and deflection (v) at each y coordinate are related to the moment by

$$EI \frac{d^2v}{dy^2} + M = 0 \quad (3-12)$$

where E is the modulus of elasticity and I is the area moment of inertia of a hollow cylinder given by $I = \frac{\pi}{64}(D_{outer}^4 - D_{inner}^4)$. The slope and deflection can be found by integrating Eqn. (3-12) once and twice, respectively, with respect to y and applying the appropriate boundary condition. For a cantilever beam, the boundary conditions imposed are $v'=v=0$ at $y=0$. Equations (3-13) and (3-14) give the slope and deflection of a cantilever beam under a linearly distributed load as a function of the y coordinate.

$$v'(y) = \frac{q_o y}{24EIL}(y^3 - 6yL^2 + 8L^3) \quad (3-13)$$

$$v(y) = \frac{q_o y^2}{120EIL}(y^3 - 10yL^2 + 20L^3) \quad (3-14)$$

Figure 3-4 displays the slope (a) and deflection (b) of a hollow cylinder with $L = 5 \mu\text{m}$, $D = 50 \text{ nm}$, $q_o \approx 4.3 \times 10^{-3} \text{ Pa}$, and $E = 1.25 \text{ TPa}$ as a function of vertical cylinder coordinate, y . It should be observed that the validity of linear beam theory begins to

deteriorate when tip rotations approach 10 degrees. If the tip rotations are larger than this value, non-linear beam theory must be used to obtain accurate results of rotations and deflections of the beam. It is important to note here that there is both experimental evidence and theory-simulations which suggest that nanotubes possess the ability to sustain significant nonlinear deformations without irreversible atomic rearrangements [79].

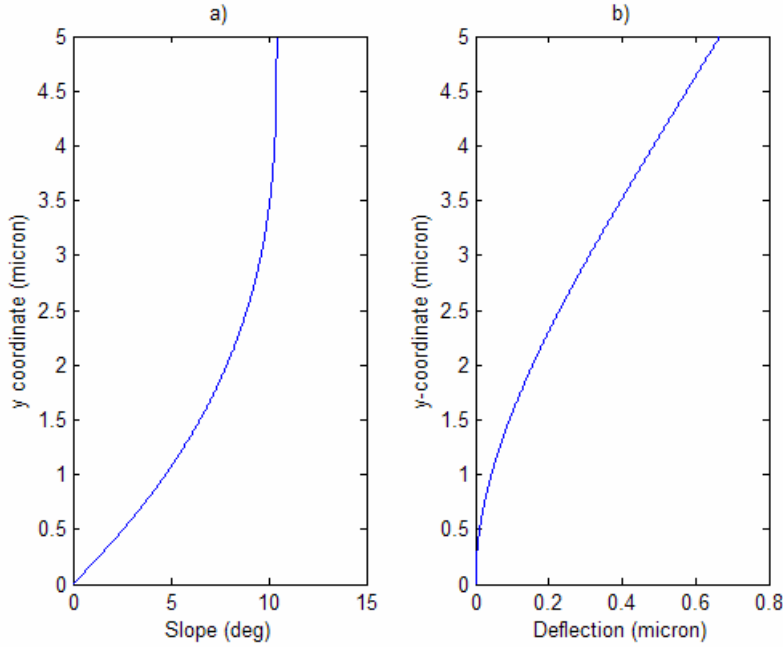


Figure 3-4. a) The rotation angle (a) and deflection (b) of a hollow cylinder ($L/D = 100$) subjected to a linearly distributed load as a function of the y coordinate.

Up to this point, it has been assumed throughout the fluid dynamic analysis that the cylinder is oriented normal to the flow. However, once the cylinder has been deflected as depicted in Figure (3-5), the previous assumption is no longer valid. To account for the change in the drag on the cylinder due to the bending, an iterative method was developed to calculate the drag component of each element depending on the rotation angle.

The velocity component normal to the element, V_n is found using,

$$V_n = V \cos \theta \quad (3-15)$$

where V is the freestream velocity and θ is the rotation angle. The Reynolds number and drag corresponding to V_n are found following the same method as above. Figure 3-5 is a

schematic representation of the velocity components and drag on an element in the bent section of the cylinder. Figure 3-6 is a plot which displays the convergence of the horizontal deflection of the nanotube through 5 iterations. Table 3-1 displays the values of both the tip displacement and tip rotation angle after each iteration.

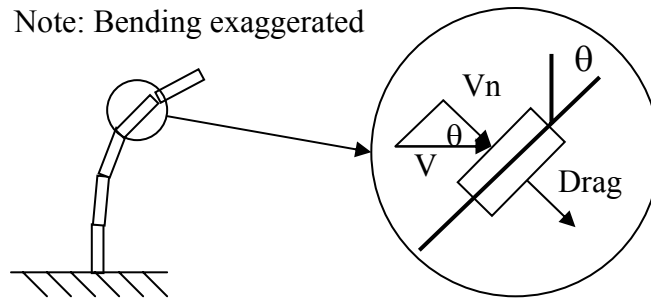


Figure 3-5. Schematic representation of the velocity components acting on an element at angle θ to the flow.

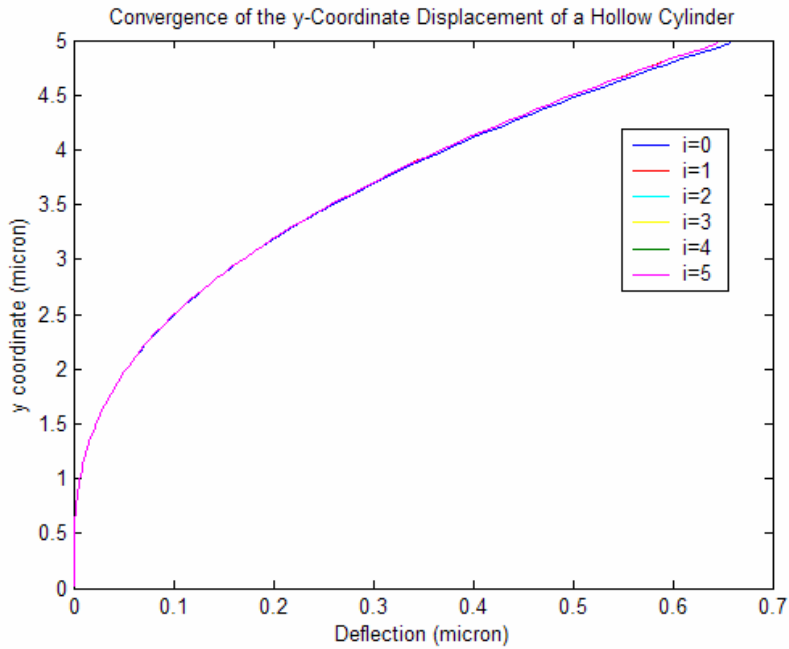


Figure 3-6. Iterative convergence (i) of the deflection of a hollow cylinder ($L/D = 100$) as a function of the y-coordinate.

Table 3-1. Convergence of values of tip displacement and rotation angle for a bent cylinder.

Iteration	Tip Displacement (nm)	Rotation Angle (deg)
0	658.2	10.36
1	645.4	10.15
2	645.9	10.16
3	645.9	10.16
4	645.9	10.16
5	645.9	10.16

As previously noted small deflection theory is limited to tip rotations of less than or approximately equal to 10 degrees. In this study, a freestanding nanotube was subjected to a linear velocity gradient given by a wall shear of 250 Pa. The case presented is the limiting case based on diameter for small deflection theory to be valid. The methods presented to calculate Re_D , C_D , etc. are constrained only by the range of Reynolds numbers for which Eqn. (3-6) is valid. If the beam mechanics of a nanotube of diameter less than 50 nanometers is desired, large deflection theory must be used. The text *Mechanics of Materials* [80] is an appropriate starting point to begin the large deflection analysis of a hollow cylinder subjected to a linearly distributed load.

3.2 Complications in the Fluid Dynamics

There are various complications present in the previous analysis of the fluid dynamics acting on a freestanding nanotube. These complications include the fluid dynamics of the presence of other nanotubes in the very low Reynolds number regime if an array of nanotubes is used, the wall region of the nanotube and the free-end region of the nanotube. A short discussion of the mentioned problems will offer explanations as to why this analysis can be deemed valid.

Flow where $0 < Re_D < 4-5$ is known as creeping flow or as a non-separation regime [77]. At low Reynolds number the creeping flow around a circular cylinder is completely laminar and there is no separation present. Analogous cases to a row of freestanding nanotubes are the cylindrical bristles of aquatic beetles. These beetles spread their cylindrical bristles on the trusting stroke to propel themselves forward. The thrust provided by the bristles is equal to the drag they would experience in a fixed

position in a fluid flow. The bristles account for two-thirds to three-quarters of the thrust and produce up to 54% as much thrust as would an equally broad solid surface [81]. These effects can become greater as the Reynolds number decreases. While a square array of nanotubes is not identical to a row of cylindrical bristles the underlying concept is the same. Thus, the deflection calculations previously made on a single nanotube are an underestimation of what an array of closely spaced nanotubes would experience.

The flow at various heights along a finite cylinder with a free end can be divided into three regions; the wall region, middle region, and free-end region (Fig. 3-7). The size of the wall region is dependent on the cylinder diameter and boundary layer thickness at the wall. An approximation of the span wise height of this region is $D/3$ [82] or about 17 nm using $D = 50$ nm for this analysis. Since this region occupies only 0.4% of the total nanotube height, the effects of the complex fluid dynamics on the deformation of the nanotube are neglected. The middle region of a finite cylinder appears for cylinders with aspect ratios greater than 5 [82]. This region represents a quasi two-dimensional flow and is dominant for cylinders with large aspect ratios. The cylinder of this analysis has a $L/D = 100$, thus it is assumed that the middle region dominates the flow, thus implying the majority of the fluid dynamics is two-dimensional. The third region, known as the free-end region, occupies from $0 < y/D < 2 - 3$ [82]. In this region the flow pattern is three-dimensional, making the loads on the tip difficult to calculate. The effects of this region are contained in the top 2 to 3% of the total cylinder length. For this reason the three-dimensional fluid dynamics effects in the free-end region were neglected [82].

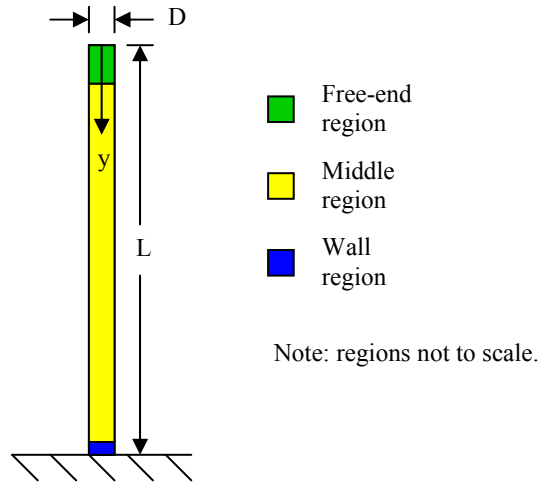


Figure 3-7. Schematic drawing of the three different flow regions of a finite cylinder with a free end.

3.3 Electro-Optical Measuring Technique

Optical properties of an array of carbon nanotubes may be utilized for skin friction measurements. When carbon nanotubes are deflected they experience changes in their electrical properties, particularly in conductance. This change in conductance influences the reflection coefficient Γ , of an optical beam incident on the nanotubes. The change in the phase angle of the reflection coefficient can be measured to predict the deflection angle of the nanotubes.

This concept employs using a fiber optic sensor, which detects a phase change in the incident signal as nanotubes deflect into the signal path. Figure 3-8 shows a schematic of undeflected nanotubes (solid) and nanotubes deflected into the signal path (dotted). The required deflection is induced by the drag the nanotubes experience in the LSL of the boundary layer of a flow.

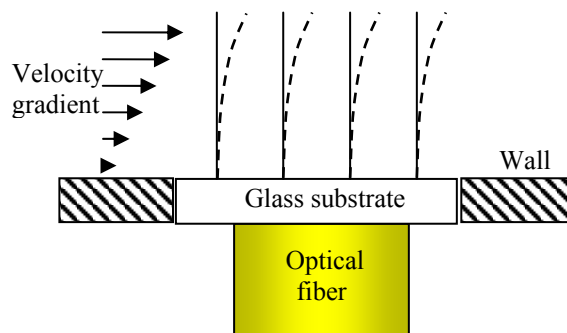


Figure 3-8. Schematic of optical viewing path of undeflected (solid) and deflected (dotted) nanotubes in the LSL.

A study of the reflection of light at the end of an optical fiber terminated into a carbon nanotube-loaded medium has been carried out [83]. The nanotubes in this study have outer diameters of 20 nanometers, lengths of 5 microns and have an average spacing between neighboring tubes of 20 to 50 nanometers. However, these results are consistent for a range of diameters and lengths as long as the scale of the nanotubes is smaller than the wavelength of the light λ , assumed to be in the range $0.8 < \lambda < 1.6$ microns. The nanotubes are considered highly conductive along the length of the tube. For this reason, the nanotube-loaded region was modeled as having anisotropic conductivity with parallel polarization where the electric field is aligned with the carbon nanotubes.

An optical fiber terminating into a carbon nanotube-loaded medium is modeled in Figure 3-9. The space in which $x' < 0$ is filled with a lossless isotropic dielectric material. The nanotubes occupy the space where $x' > 0$ and make an angle θ_0 with the x' -axis. At $x' = 0$ a uniform plane wave with parallel polarization is normally incident to the two regions mentioned above.

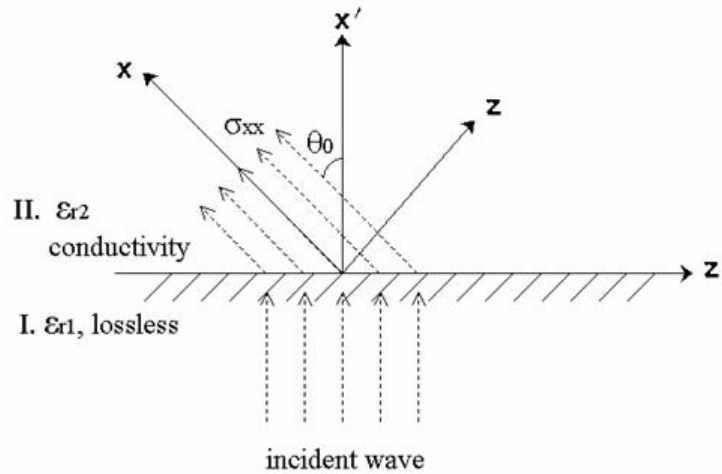


Figure 3-9. Schematic of an incident wave into a nanotube-loaded medium at a deflection angle θ_0 [83].

The incident wave shown in Figure 3-9 is partially reflected and partially transmitted into the nanotube-loaded medium. Beginning with the expressions for the incident, reflected, and transmitted waves one can show the complex reflection coefficient is expressed as:

$$\Gamma = \frac{\cos \theta_0 - \sqrt{\frac{\varepsilon_{r2}}{\varepsilon_{r1}}} / \sqrt{1 + \frac{\tan^2 \theta_0}{1 - \frac{j\sigma_{xx}}{\omega\varepsilon_2}}}}{\cos \theta_0 + \sqrt{\frac{\varepsilon_{r2}}{\varepsilon_{r1}}} / \sqrt{1 + \frac{\tan^2 \theta_0}{1 - \frac{j\sigma_{xx}}{\omega\varepsilon_2}}}} \quad (3-16)$$

where θ_0 is the deflection angle of the nanotubes, ε_{r1} is the relative permittivity of region I, ε_{r2} is the relative permittivity of region II, σ_{xx} is the conductivity constant along the axis of the nanotube length, and $\varepsilon_2 = \varepsilon_0 \varepsilon_{r2}$ [83].

Numerical results of the reflection coefficient were obtained by considering an example case where the incident wave is being produced by an optical fiber. The core refractive index, n_1 , of a typical glass fiber is 1.48. This leads to a relative permittivity of region I, $\varepsilon_{r1} = n_1^2 = 2.19$. Measurements of the optical properties of carbon nanotubes have been found by de Hear *et al.* [84] over a photon energy range of 1.5 eV to 5 eV. A photon energy of 1.5 eV gives a relative permittivity value of $\varepsilon_{r2}=1.8$ and $\sigma_{xx}/\omega\varepsilon_0 = 1.5$ [84]. Using these numerical values in Eqn. (3-16), the magnitude and phase of the reflection coefficient can be determined for various deflection angles. Figures 3-10 and 3-11 display the variations in the magnitude and phase angle of the reflection coefficient versus the deflection angle, θ_0 [83].

This concept employs detecting a phase angle change in the incident wave. Examining Figure 3-11, when θ_0 equals 15 degrees the phase angle of the reflection coefficient is approximately 10 degrees. This value of 15 degrees is a driving constraint for the minimum value necessary to produce a measurable phase angle of Γ .

Revisiting the previous analysis of a freestanding nanotube subjected to a velocity gradient, it can be shown that the drag on a cylinder with a diameter of 45 nm and a length of 5 microns will produce a tip deflection angle of 15 degrees. It should be observed that these dimensions have been obtained using small deflection beam theory, whose accuracy deteriorates rapidly for rotation angles greater than 10 degrees. Non-linear beam theory must be applied to achieve accurate estimations of the rotation angles.

CHAPTER 3 – FREESTANDING ARRAY OF MWNTS AS A C_f GAGE

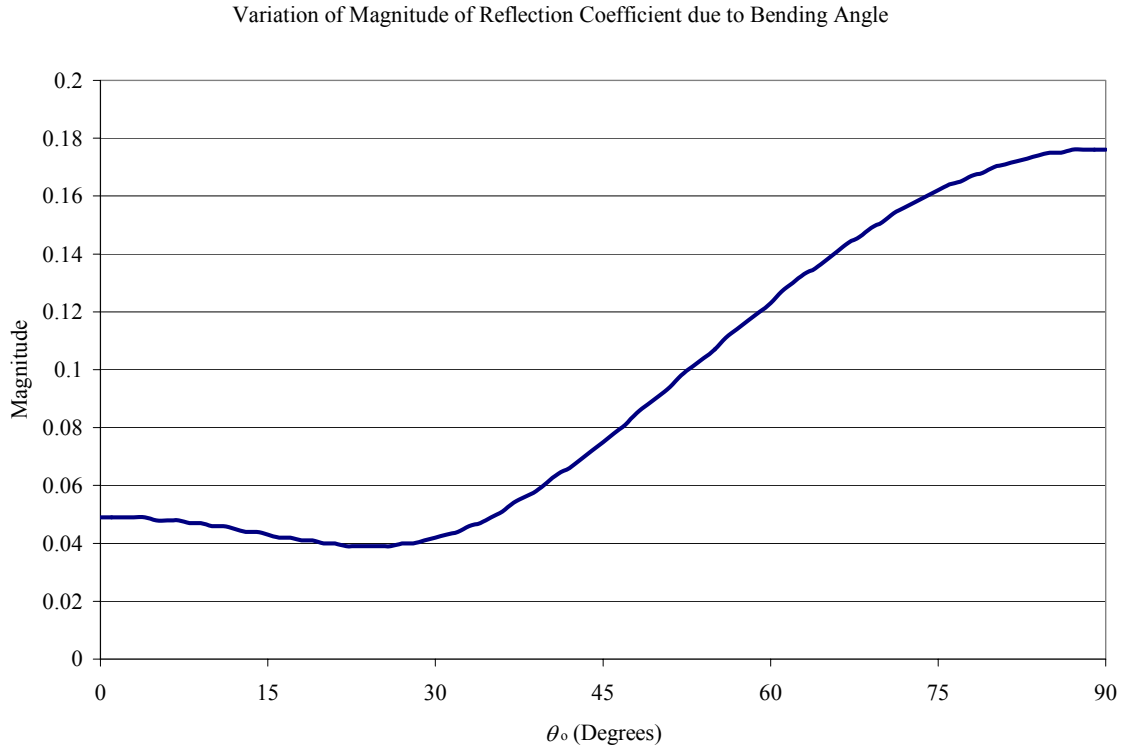


Figure 3-10. Variation of magnitude of reflection coefficient versus deflection angle [83].

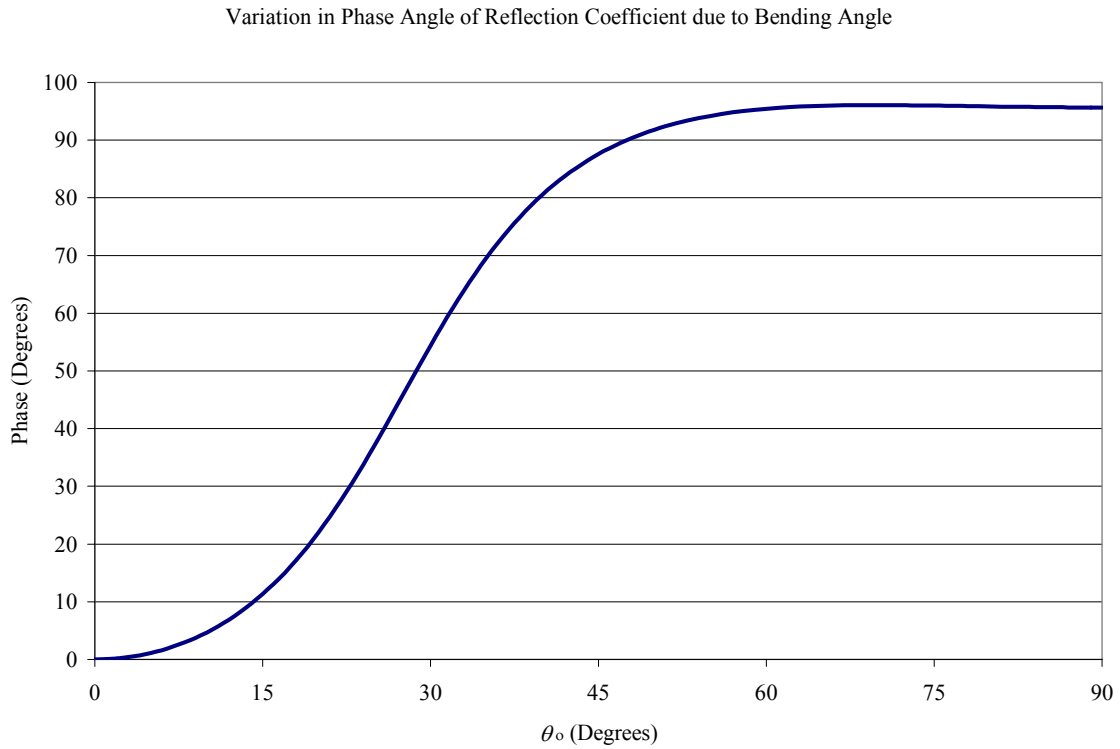


Figure 3-11. Variation in the phase angle of the reflection coefficient versus deflection angle [83].

4 TABLE TOP DESIGN UTILIZING MWNTS AS A C_f GAGE

4.1 Advantages of a Table Top Design

Carbon nanotubes were implemented into the design of a traditional skin friction sensor by replacing the flexure and supporting the sensing element on an array of nanotubes (Fig. 4-1). Two methods were explored to obtain skin friction measurements; an electromechanical method and a purely mechanical method. The background to this approach and the two measurement techniques are investigated in detail in the following sections.

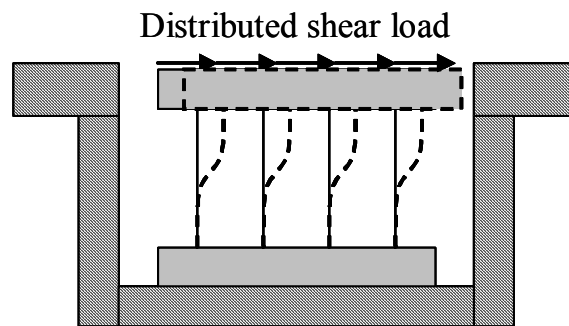


Figure 4-1. Schematic of undeflected (solid) and deflection (dotted) nanotubes supporting a sensing element. Note: deflection of nanotubes is exaggerated.

Utilizing this design concept, the sensor head would be the only surface in contact with the fluid medium. This is advantageous over an array of freestanding nanotubes in a flow because it replaces the need for a complex fluid mechanics and structural interaction analysis. In this design, small deflection beam theory can be used solely to predict the bending of the nanotubes. The trade off of using small deflection theory in place of a coupled fluid mechanics/structural problem is an accurate solution to a simple problem instead of an approximate solution to an intricate problem.

The use of an evenly distributed array of nanotubes supporting a sensing element provides resistance to the pressure gradient applied to the sensing element when a fluid moves past the gage (Fig. 4-2). The advantage is that the evenly distributed array would minimize any misalignment caused by the tilting of the sensor head, which contributes to the uncertainties of a skin friction measurement

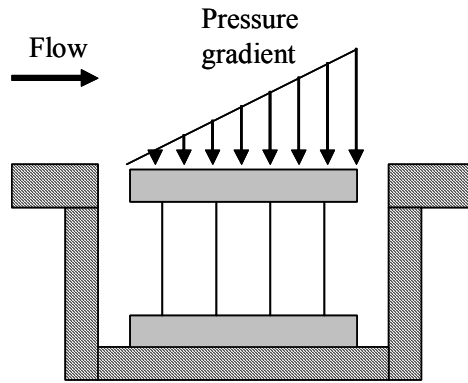


Figure 4-2. Schematic of pressure gradient applied to the sensing element.

4.1.1 Analytical Design

The analytical solution of the tip displacement and bending angle was developed for a single nanotube clamped at one end and constrained at the tip with a point force applied to the tip (Fig. 4-3a). Figure 4-3b displays defined positive moment and shear force direction used to arrive at the solution.

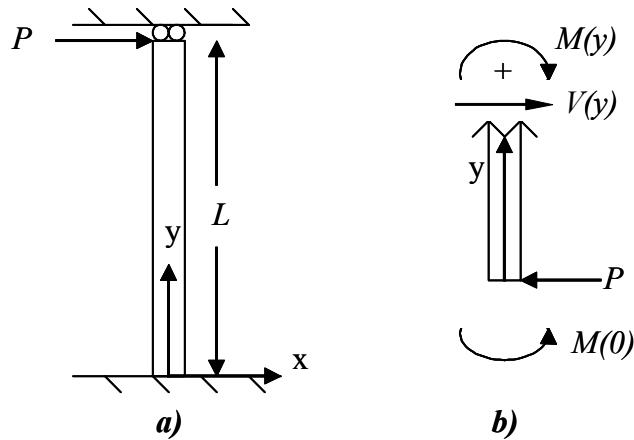


Figure 4-3. (a) Schematic of clamped-constrained nanotube with point load. (b) Free body diagram.

From Figure 4-3 equation (4-1) through (4-5) can be inferred:

$$v'(0) = 0 \tag{4-1}$$

$$v'(L) = 0 \tag{4-2}$$

$$v(0) = 0 \tag{4-3}$$

$$V(y) = P \tag{4-4}$$

$$M(y) = -M(0) + Py \quad (4-5)$$

where $M(0)=PL/2$. Substituting into Eqn. (4-5), the moment $M(y)$ is:

$$M(y) = -\frac{P}{2}(2y - L) \quad (4-6)$$

The bending angle (v') and deflection (v) at each y coordinate are related to the moment by Eqn. (4-7).

$$EI \frac{d^2v}{dy^2} - M = 0 \quad (4-7)$$

The bending angle and deflection can be found by integrating Eqn. (4-7) once and twice respectively with respect to y and applying the appropriate boundary condition. For a clamped-constrained beam the boundary conditions imposed are $v'(0)=v'(L)=v(0)=0$. Equations (4-8) and (4-9) give the bending angle and deflection as a function of the y coordinate of a clamped-constrained beam subjected to a point load at $y=L$.

$$v'(y) = -\frac{P}{2EI}(y^2 - Ly) \quad (4-8)$$

$$v(y) = -\frac{P}{12EI}(2y^3 - 3Ly^2) \quad (4-9)$$

The maximum bending angle occurs when $y=L/2$ and is given by:

$$v'(L/2) = \frac{PL^2}{8EI} \quad (4-10)$$

The maximum deflection occurs at $y=L$ and is given by:

$$v(L) = \frac{PL^3}{12EI} \quad (4-11)$$

Figure 4-4 is the analytical solution of the bending angle and deflection of a clamped-constrained hollow circular cylinder with a point force applied to the tip. The ordinate displays the y coordinate of the nanotube while the abscissa displays the bending angle or displacement. The inner and outer diameters of this case are 40 and 80 nanometers respectively. The cylinder has a length of 10 microns and the applied point load is 3.29×10^{-8} N. These values are used in the analysis because they are representative of the nanotube dimensions NanoLab (a nanotube supplier) is capable of

producing. The modulus of elasticity used in the analytical solution is 1.25 TPa due to it being the most agreed upon value in both theoretical and experimental studies [64-68].

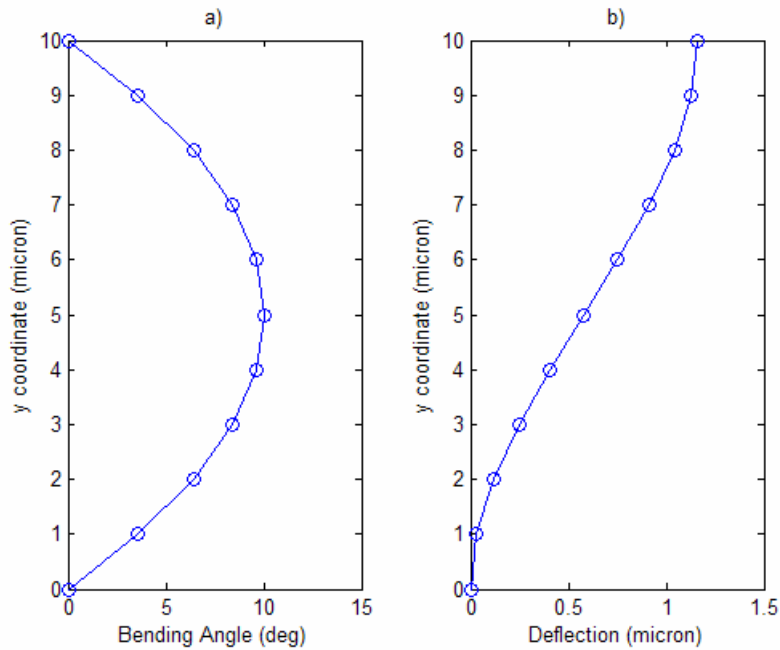


Figure 4-4. Analytical solution of a clamped-constrained hollow cylinder with point load at tip.

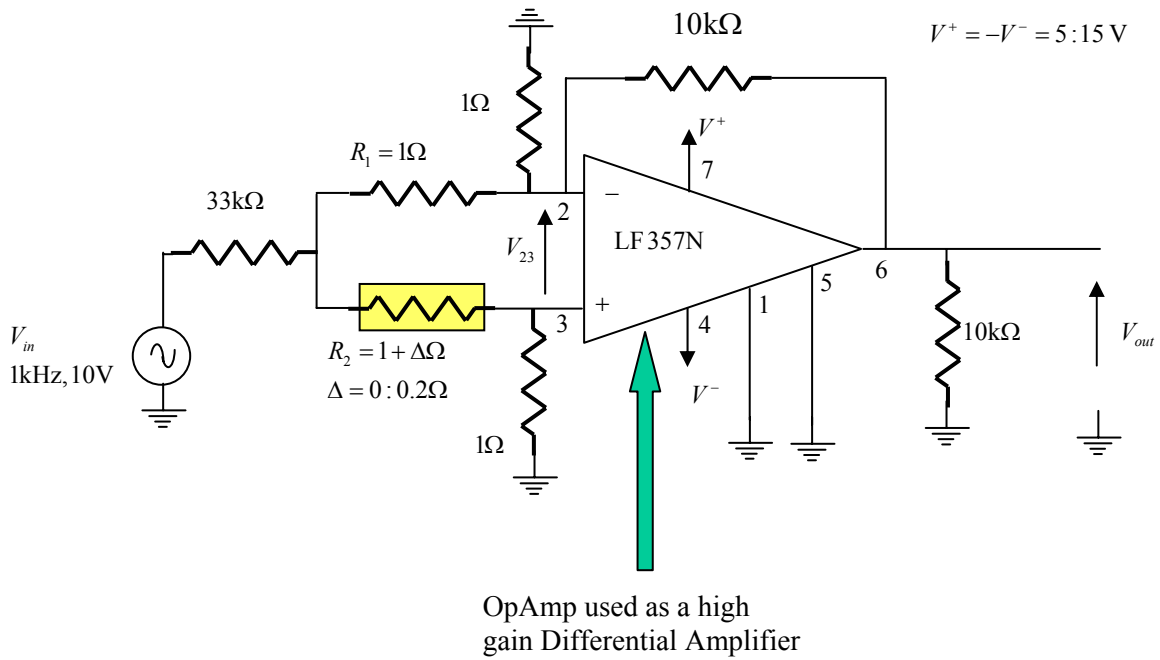
4.2 Electromechanical Measurement Concept

The basis for the electromechanical measurement concept lies in the assumption that the electrical properties of MWNTs change when they experience mechanical deformation. This mechanical deformation of the array of nanotubes is induced by the shear force applied to the sensor head as seen in Figure 4-1. The validity of the assumption is not certain since the previous studies, both theoretical and experimental, of the electromechanical properties were conducted on SWNTs [71,72]. However, since MWNTs are similar to many SWNTs of various diameters [85], the concept was pursued.

Figure 4-5 is a schematic representation of the circuit diagram which was designed to measure the change in resistance of an array of nanotubes subjected to mechanical deformation. This circuit was designed and built by Dr. Salem of the Electrical Engineering Department of Virginia Tech (Fig. 4-6). It was successfully tested to measurement a resistance change of 0.13 Ohms. The array of nanotubes were designed to have a change in resistance equal to or greater than this value when deflected. Figure 4-7 shows the output reading as seen on the oscilloscope of 1.2 Ohms (a) and 1.0

CHAPTER 4 – TABLE TO DESIGN UTILIZING MWNTS AS A C_f GAGE

Ohms (b). The difference between the two readings can clearly be seen in the variation of the amplitude of the two signals.



$$V_{23} = \frac{V_{in}}{33000(1/2 + 1/(2 + \Delta)) + 1/33000} \left(\frac{1}{2} - \frac{1}{2 + \Delta} \right) \quad \Delta = 0.2\Omega \Rightarrow V_{23} = 14.43\mu V \Rightarrow V_{out} \approx 150mV$$

Figure 4-5. Schematic of circuitry used to measure very small changes in resistance.

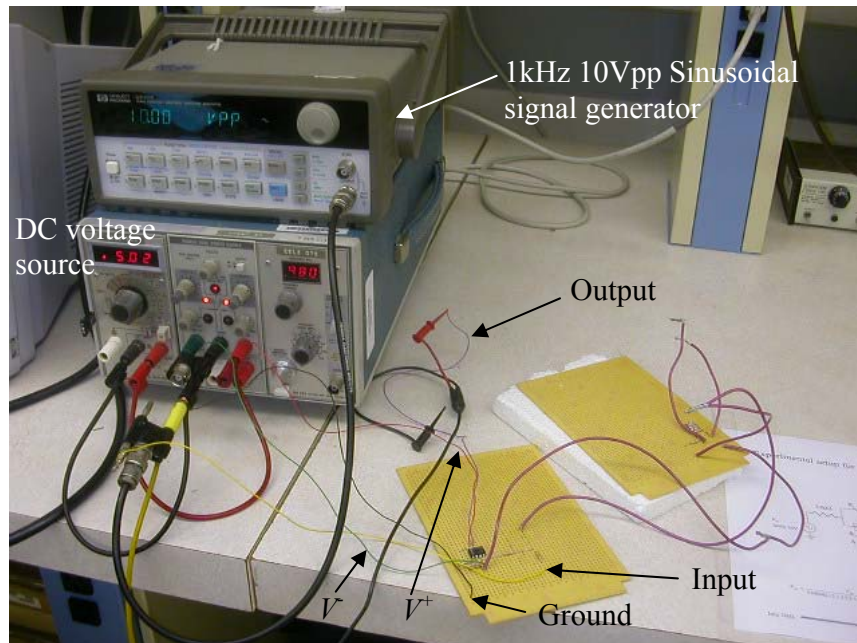


Figure 4-6. Photograph of experimental set up used to measure small changes in resistance.

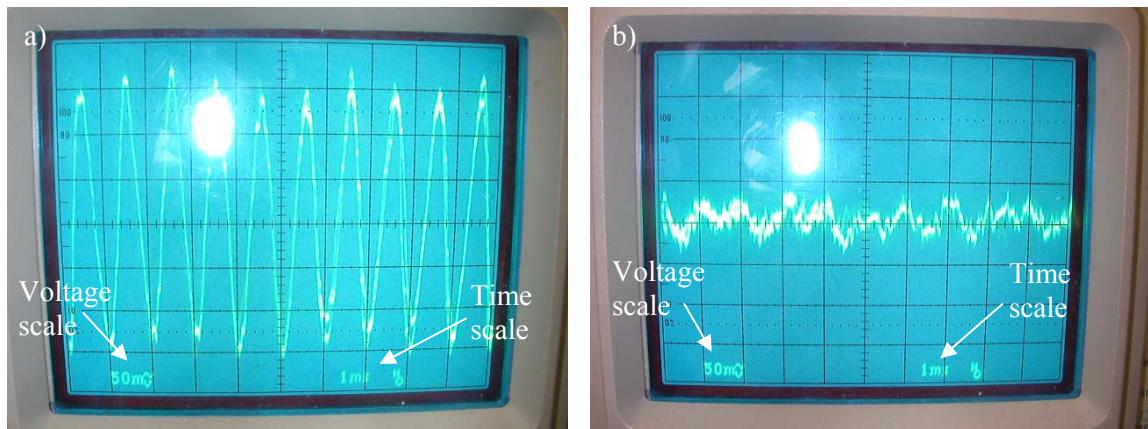


Figure 4-7. Photograph of oscilloscope display for 1.2 Ohms (a) and 1.0 Ohms (b).

4.2.1 Design of Sensor

The goal was to design a sensor which has a change in resistance greater than or equal to 0.13 Ohms when mechanically deformed due to shear. Figure 4-8 is a schematic illustration of the electrical pathway through the skin friction sensor. Theoretically, V_{out} before the deformation of nanotubes will be different than V_{out} after their deformation due to the change in resistance of the deformed nanotubes.

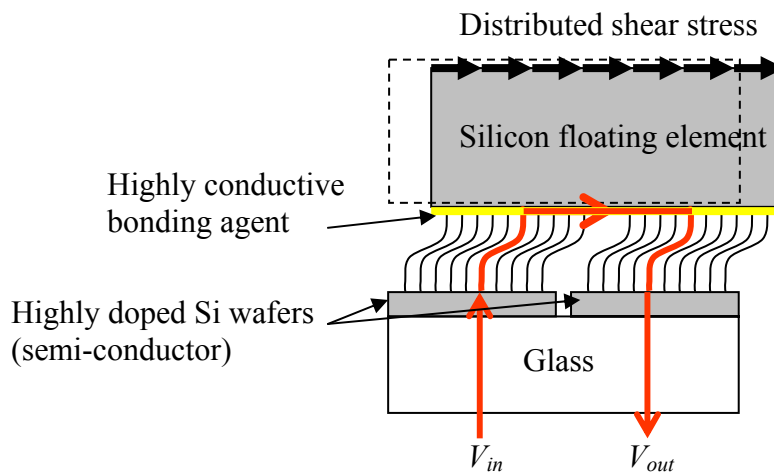


Figure 4-8. Schematic illustration of a skin friction sensor which utilizes the electromechanical measurement technique.

Figure 4-9 is a schematic illustration of the two substrates with wire leads, mounted to a glass slide. The two doped silicon substrates are $\frac{1}{2} \times \frac{1}{2}$ inch with nanotubes

grown on $\frac{1}{4} \times \frac{1}{4}$ inch areas. The nanotubes in each array are in parallel and the two arrays are in series. The total resistance of the system is calculated as follows:

$$R_{System} = R_{Arrays} + R_{Substrates} = \left(\sum_{j=1}^{N/2} \frac{1}{R_j} \right)^{-1} + \left(\sum_{j=1}^{N/2} \frac{1}{R_j} \right)^{-1} + R_{Substrates} \quad (4-12)$$

where N is the total number of nanotubes in the system, R_j is the resistance of the j^{th} nanotube and $R_{Substrates}$ is the added resistance of the two doped silicon substrates and the bonding agent.

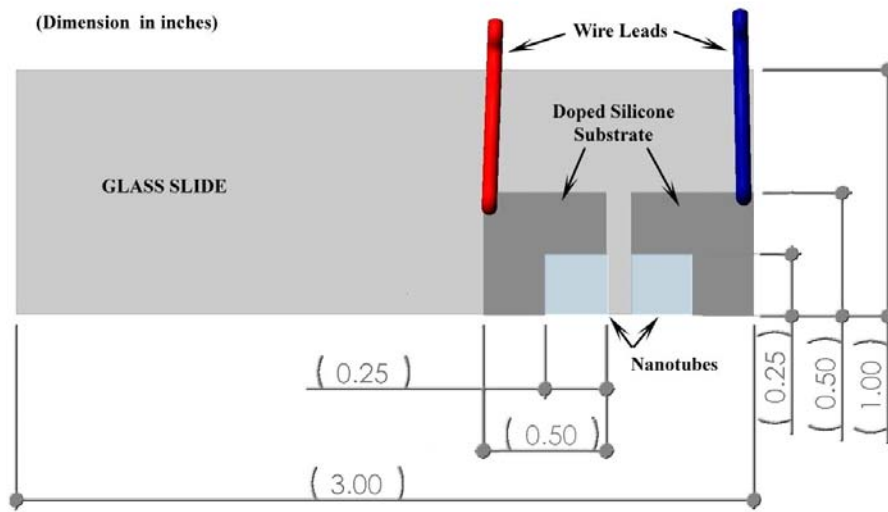


Figure 4-9. Schematic illustration of two silicon substrates bonded to a glass slide with wire leads attached.

In Chapter 2, the relationship between conductance and bending angle of SWNTs was introduced. This information is used to design the array such that the change in resistance meets the constraint of $\Delta R \geq 0.13 \Omega$. First, the constant resistance of the system ($R_{Substrates}$) must be calculated. Then, the nominal resistance of two arrays of nanotubes with lengths of 10 microns and outer diameters of 80 nm was calculated. These nanotube dimensions were given by NanoLab to be within their capabilities of growing vertically aligned arrays using an electrochemical growth method.

4.2.2 Resistance of Substrates

The last term in Eqn. (4-12) is the added resistances of the two substrates and the bonding layer. Assuming current travels through the entire silicon substrate, the conducting volume of each of the silicon substrates is $\frac{1}{2} \times \frac{1}{2}$ inches and 675 microns (0.0266”) thick. The resistivity of doped silicon ranges from 0.001 – 0.005 Ω -cm. Using

$$R = \frac{\rho L}{S} \quad (6-13)$$

where $\rho = 0.005 \Omega$ -cm, $L = 675$ microns and $S = 0.25$ square inches, $R = 2.093 \times 10^{-4}$ Ohms. The bonding agent is chromium based and is assumed to have a resistivity of approximately $1.29 \times 10^{-5} \Omega$ -cm. The conducting area is simply the area of the sensing element which is $0.55 \times \frac{1}{4}$ inches. The thickness (L) is estimated to be 1 micron. Again using Eqn. (4-13), $R = 1.454 \times 10^{-9}$ Ohms. Thus $R_{Substrate} = 4.186 \times 10^{-4}$ Ohms.

4.2.3 Nominal Resistance of Nanotube Arrays

The method of calculating a theoretical value for the resistance of an array of MWTNs was to use the range of resistances (5 – 15 k Ω) found experimentally by Collins *et al.* of single MWNTs at room temperature [69]. This range of values was used in Eqn. (4-12) as the parameter R_j to find the upper and lower resistance of the two arrays consisting of N total tubes.

The total number of nanotubes depends directly on the desired displacement and bending angle. To ensure that the array of nanotubes would not buckle due to the mass of the sensor head, the maximum bending angle was constrained to be 10 degrees. Converting to radians and using Eqn. (4-10) the tip load, P can be found. The force per nanotube to obtain a maximum bending angle of 10 degrees is 3.29×10^{-8} N. The total force applied to the array of nanotubes due to wall shear can be found using Eqn. (4-14),

$$P = \tau_{wall} S \quad (4-14)$$

where τ_{wall} is the shear level at the wall and S is the surface area of the sensor head. Using the value $\tau_{wall} = 250$ Pa to simulate a Mach 2.4 flow and $0.55 \times \frac{1}{4}$ inches for the surface area, $P = 0.022$ N. Dividing the total force by the tip load per nanotube gives the total

number of nanotubes (N) to be approximately 6.7×10^5 . This corresponds to a forest density of 7.6×10^5 NT/cm² or a spacing of 7.7 microns between neighboring tubes.

The critical load, P_{cr} was found to estimate if the forest of nanotubes would buckle under the weight of the sensor head.

$$P_{cr} = \left(\frac{\pi^2 EI}{L^2} \right) N \quad (4-15)$$

Solving for P_{cr} , it is found that the critical load of the nanotube forest is approximately 0.16 N. The weight of the silicon sensor head can be found using

$$W = \rho_{silicon} Vg \quad (4-16)$$

where $\rho_{silicon} = 2200$ kg/m³, V is the volume of the sensing head (3.32×10^{-8} m³) and g is the gravitational constant 9.817 m/s². Using these values $W = 7.17 \times 10^{-4}$ N, giving a factor of safety ($FOS = P_{cr}/W$) of greater than 200.

Substituting $N = 6.7 \times 10^5$ and the range $5 \leq R_j \leq 15$ k Ω into Eqn. (4-12) gives the range of resistances of the non-deformed arrays as $3.0 \times 10^{-2} < R_{Arrays} < 8.9 \times 10^{-2}$ Ω .

4.2.4 Theoretical Change in Resistance of Nanotube Arrays

As mentioned in Chapter 2, depending on the chirality of a single-wall nanotube, when subjected to deformation, the conductance can significantly decrease due to simple stretching of the nanotube. Table 4-1 summarizes the effect of bending angle on conductance of a (6,6) armchair nanotube and a (12,0) zigzag nanotube. The information presented indicates that the conductance of an armchair nanotube does not change when subjected to bending. The metallic zigzag nanotube, on the other hand, experiences a conductance drop, or resistance increase, of approximately 23% when the bending angle is 10 degrees. The range of resistances for a single metallic zigzag nanotube given previously as 5 – 15 k Ω , increases to 6.15 – 18.45 k Ω when the bending angle equals 10 degrees.

Table 4-1. Summary of conductance drop due to bending angle taken from Figure (2-10).

Bending Angle (deg)	Approximate Conductance Drop (%)	
	(6,6) Armchair	(12,0) Zigzag
0	0	0
5	0	12
10	0	23
15	0	30
20	0	36
25	0.25	41
30	0.5	46
40	1	50

The wrapping vector dictates if the nanotubes are metallic or semiconducting. If the wrapping vector occurs with equal probability, 1/3 of all SWNTs would be metallic and 2/3 semiconducting [85]. Referring to Figure 2-6, the percentage of all nanotubes which are metallic zigzag nanotubes is approximately 6%. Using the theoretical change in resistance of a metallic zigzag nanotube, the resistance of the two arrays with a bending angle of 10 degree can be calculated by

$$R_{System} = R_{Arrays} + R_{Substrates} = 2 \left[\left(\sum_{i=1}^{N_{metalliczigzag}/2} \frac{1}{R_i} \right)^{-1} + \left(\sum_{j=1}^{N_{armchair}/2} \frac{1}{R_j} \right)^{-1} \right] + R_{Substrates} \quad (4-17)$$

where $N_{metalliczigzag} = (0.0625)(N)$, $N_{armchair} = (0.9375)(N)$, $6.15 \leq R_i \leq 18.45$, and $5.0 \leq R_j \leq 15.0$. Substituting these values into Eqn. (4-17), R_{Arrays} ranges from 4.25 to 12.75 Ohms. Thus, the total change in the resistance of due the arrays being deflected 10 degrees is $4.4 \times 10^{-4} \leq \Delta R \leq 1.3 \times 10^{-3} \Omega$. This range of the theoretical change in resistance due to bending does not meet the constraint $\Delta R \geq 0.13 \Omega$.

One possible method to increase the change in resistance of the nanotube arrays due to bending is to electrically isolate a much smaller portion of the nanotubes. The system would retain the same mechanical behavior as before, while increasing the total resistance of the two arrays. It was proposed to mask two ¼” x 50 micron electrode strips on the substrate before the nanotubes where grown. The number of nanotubes in each of these electrode strips is approximately 2400 using the forest density given in Section 4.2.3.

The change in resistance due to bending of the two arrays can be recalculated using Eqn. (4-17) where $N = 4825$. By electrically isolating a much smaller number of tubes, the new range of values of the change in resistance is $0.06 \leq \Delta R \leq 0.18 \Omega$. This range of values is sufficiently close to meeting the constraint $\Delta R \geq 0.13 \Omega$.

4.3 Array of Nanotubes as a Flexure

The measurement technique of utilizing an array of nanotubes as a flexure to quantify values of skin friction was explored. The unique mechanical properties nanotubes possess lend themselves to the application of being used as a structure. An array of carbon nanotubes would be used to support a sensing head which would be exposed to the fluid flow in study as in Figure 4-1. A fiber optic displacement sensor would view the side of the sensor head and measure any movement due to wall shear.

The basic concept behind the fiber-optic interferometry system is that laser light propagates down an optical-fiber. Extrinsic Fabry-Perot interferometry (EFPI), invented by Murphy [57], relies on the formation of a low-finesse Fabry-Perot cavity in the gap between the end of the fiber and the reflective surface as shown in Figure 4-10. Some of the light is reflected at the end of the fiber and some travels through the end of the optical fiber and across a gap. The light reflected at the end of the fiber propagates back down to a spectrometer. The light not reflected passes through the end of the fiber, across a gap and hits an optically reflective surface (the sensor head in the present case). A portion of this light is returned to the core of the fiber and propagates back to the same spectrometer. The resulting fringe pattern, i.e. interference between the two reflections, can be processed to determine the distance between the end of the fiber and the reflector.

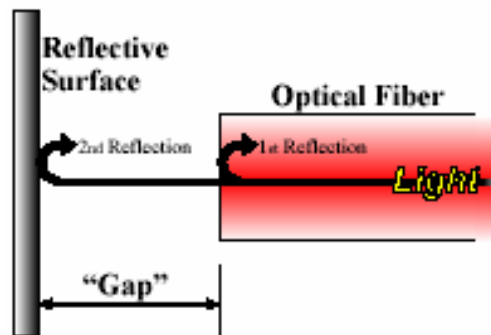


Figure 4-10. Schematic illustration of fiber optic displacement sensor [91].

Figure 4-11 illustrates the fiber-optic system used to measure the gap between the fiber and reflector. The outgoing signal is shown in the first portion of the figure. The light passes through the sensor, which consists of a fiber with a gap between it and a reflector. The light, which returns to the fiber core, is then measured by a spectrometer and the resulting fringe pattern is shown to the right in Figure 4-11 as the returned signal. The detailed definition of a fringe pattern can be found in [86]. This signal is then processed with a proprietary Luna Innovations' Algorithm, and the user receives a output of the gap between the fiber and reflector [57].

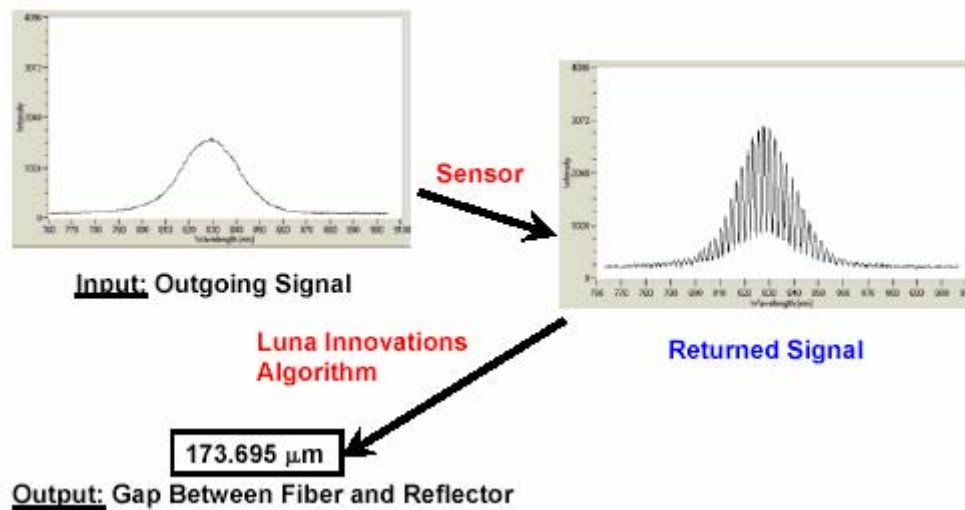


Figure 4-11. Diagram of Fiber Optic system used to measure gap distance [57].

Three possible variations of arrays of MWNTs were investigated; arrays of aligned MWNTs, aligned MWNT structures, and nanotubes grown by a ‘Lift-up’ technique.

4.3.1 Aligned MWNTs

The method of utilizing an array of vertically aligned MWNTs was first explored. A sensor was designed with two arrays of MWNTs with outer diameters of 20 nm and lengths of 20 microns. The nanotubes were to be grown on one ½ x ½ inch glass slide and supported a ¼ x 0.55 inch silicon sensor head.

The constraint on this array was again that the maximum bending angle did not exceed 10 degrees. Following the same procedure as in Section 4.1.1, the tip load per nanotube was found to be 3.21×10^{-11} N. Using this tip load in Eqn. (4-11) the maximum

deflection is 1.16 microns. If this load per nanotube is divided by the total force due to shear, the total number of tubes in the two arrays is calculated ($N = 6.91 \times 10^8$, or forest density = 7.81×10^8 NT/cm²). The spacing of the nanotubes is 340 nm from center to center.

To ensure the nanotubes did not buckle under the weight of the sensor head the critical load of the nanotube array was calculated using Eqns. (4-15) and (4-16). Using the values given above, $P_{cr} = 0.16$ N. The weight of the sensor head is the same as previously calculated, $W = 7.17 \times 10^{-4}$ N. The buckling load of the nanotube forest is greater than 200 times that of the weight of the sensor head.

4.3.2 Aligned MWNT Structures

Structures of MWNTs, grown in ordered arrays, were explored for use as flexures in a skin friction sensor. Figure 4-12a,b are SEM images of aligned MWNT structures grown by Dai *et al.* [87]. Each structure consists of many MWNTs which grow perpendicular to the substrate (Fig. 4-12c). They are grown from patterned iron squares on a porous silicon substrate (Fig. 4-12d). The base dimensions of the structures are controlled by the size of the openings in the shadow masks used to pattern the iron on the silicon. These structures can be grown in various heights from 10 – 240 microns. The MWNTs are held together via Van der Waals interactions.

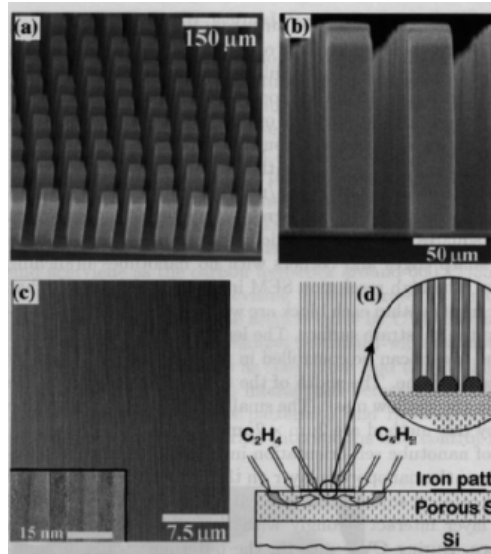


Figure 4-12. SEM images of aligned MWNT structures. (a) Oblique view. (b) Side view. (c) Detailed side view. (d) Schematic diagram of the growth process [87].

An array of MWNT structures can be designed to deflect a desired distance when subjected to a shear force. The analytical solution has been derived for a clamped-constrained beam previously in Section 4.1.1. However, the second moment of inertia, I is no longer that of a single MWNT. Figure 4-13 represents one MWNT structure, given that the nanotubes are of equal diameter and that no gaps exist between tubes.

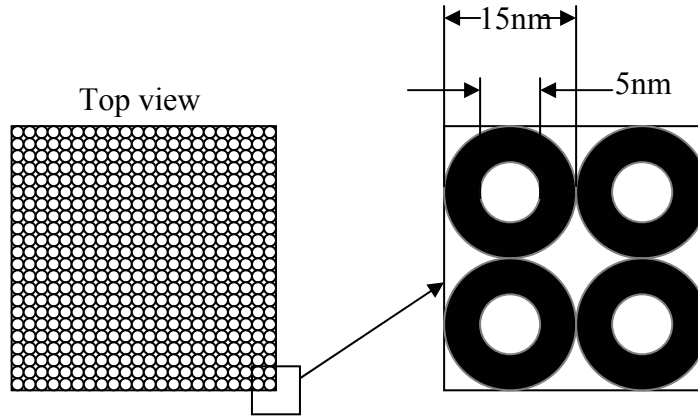


Figure 4-13. Representation of the top view of one MWNT structure (Dimensions obtained from Figure (4-12c)).

The contribution of each MWNT must be added to obtain the area moment of inertia of a single tower (Fig. 4-14). In this figure (x_j, y_i) is the (x,y) coordinate of the i^{th} nanotube in the j^{th} column.

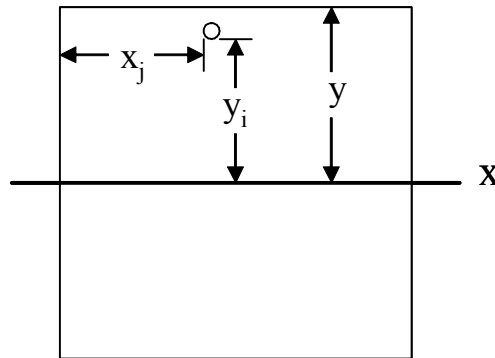


Figure 4-14. Representation of the contribution to the area moment of inertia of one nanotube in the j^{th} column a distance y_i from the neutral axis, X .

Equation (4-17) is the contribution to the second moment of inertia of each nanotube,

$$I_{xx_i} = y_i^2 S + \bar{I}_{xx_i} \quad (4-18)$$

where $y_i = y - (2i - 1)r_o$, $S = \pi(r_{outer}^2 - r_{inner}^2)$ and $\bar{I}_{xx_i} = \pi(d_{outer}^4 - d_{inner}^4)/64$. The total area moment of inertia is given by;

$$I_{xx} = \sum_{j=1}^{\#columns} \left(2 \sum_{i=1}^{\#rows} (y_i)^2 S + \bar{I}_{xx_i} \right) \quad (4-19)$$

where j goes from 1 to the number of columns and i goes from 1 to the number of rows of nanotubes in each structure.

A variety of designs of arrays of aligned MWNT structures supporting a sensor head of radius 1.0 mm which gave desired displacements (>200 nm) were obtained. Since the base dimensions are controlled by the design of the shadow mask and the height is controlled by the growth duration, there are a number of designs. For our purposes, an array of four MWNT structures supporting the sensor head was selected. The structures had dimension of 5 x 20 x 150 microns. This predicted a displacement of approximately 300 nm.

The buckling load of one tower can easily be calculated using the values of the parameters given above. From Figure 4-14, $x = 20$ microns and $y = 2.5$ microns, giving the number of columns to be 1333 (x/d_{outer}) and the number of rows to be 166 (y/d_{outer}). The area moment of inertia for this geometry is approximately $145.4 \mu\text{m}^4$. Substituting these values into Eqn. (4-15) $P_{cr} = 0.32$ N. The weight of the sensor head is negligible ($W = 2.37 \times 10^{-5}$ N) compared to P_{cr} .

4.3.3 'Lift-Up' Growth Technique

A method exists which has a controlled synthesis of vertically aligned carbon-nanotube patterns. Nanotubes are grown under patterned metal layers on silicon substrates by combining chemical-vapor deposition and conventional lithography. It has been demonstrated that metal patterns are lifted up by vertically aligned nanotubes during growth (Fig. 4-15). This lift-up growth links the thin-film metal patterns and the silicon substrate via nanotube assemblies, giving the possibility of creating nanotube architectures in three dimensions [88].

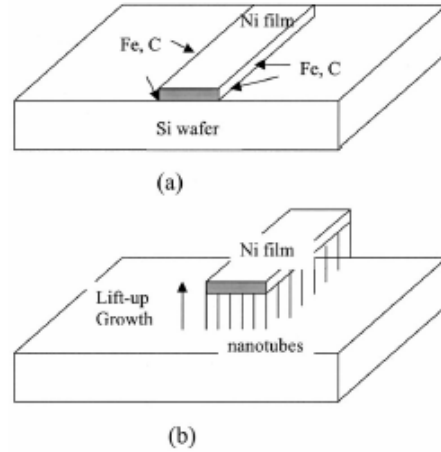


Figure 4-15. Schematic illustration showing the growth of aligned nanotube films, leading to the lift up of metal films [88].

Using conventional lithography, 15 – 100 nm thick Ni films are patterned on to a silicon substrate. Similarly to the MWNT structures, the pattern under which the nanotubes are grown is dictated by the user. The nanotubes have an average diameter of 20 – 40 nm and the lengths are variable between 50 – 100 microns by the growth process. Information was provided by the author of Ref. [88] that the density of the nanotube forest in these structures is approximately 2×10^{10} NT/cm², which corresponds to a spacing of 50 nm between neighboring tubes.

Based on the dimensions of the sensor head (2 x 2 mm), the shear load, and the information concerning the nanotubes, a pattern was designed that gave a tip deflection of 1 micron. Using Eqn. (4-11), the tip load per nanotube, P can be solved for by setting $L = 50$ microns and I equal to the second moment of inertia for a nanotube with an outer diameter of 30 nm. The total number of nanotubes needed in the array is known by dividing the total shear force by the load per nanotube, which gives N to be 4.5×10^8 . The Ni patterns chosen were circles with diameters of 15 microns. The spacing between the edges of the circular patterns is 10 microns. This array is termed 80 x 80 due to the number of patterns per row and column.

Substituting the necessary values to Eqn. (4-15), the buckling load for this arrangement is calculated to be approximately 0.08 N. The weight of the sensor head ($W = 3.28 \times 10^{-5}$ N) is again negligible when compared to the buckling load of the forest.

4.4 Potential Uncertainties

The calculations performed throughout this chapter make a few non-trivial assumptions concerning an array of MWNTs. This analysis has been conducted treating the nanotubes as perfect circular cylinders. Exact spacing and geometry of the array of nanotubes, along with uniformity of the individual nanotubes has been assumed. A short discussion on the impacts of these assumptions will follow.

Perhaps the largest leap of faith when conducting this analysis of an array of nanotubes supporting a sensor head is that the nanotubes are assumed to be perfect cylinders. Any defects in the arrangement of the carbon atoms can affect both the electrical and mechanical properties. Defects such as pentagons, heptagons, vacancies, or dopant are found to drastically alter the electrical properties of these nanosystems [89]. Figure 4-16 displays the electron density of states for an ideal nanotube and a highly defective tube. There is one post-treatment method which removes many of the structural defects. The nanotubes are heated in an inert atmosphere to a temperature in the range 1800 – 2600°C [75]. However, the extent to which the defects are removed is unknown, leaving a level of uncertainty.

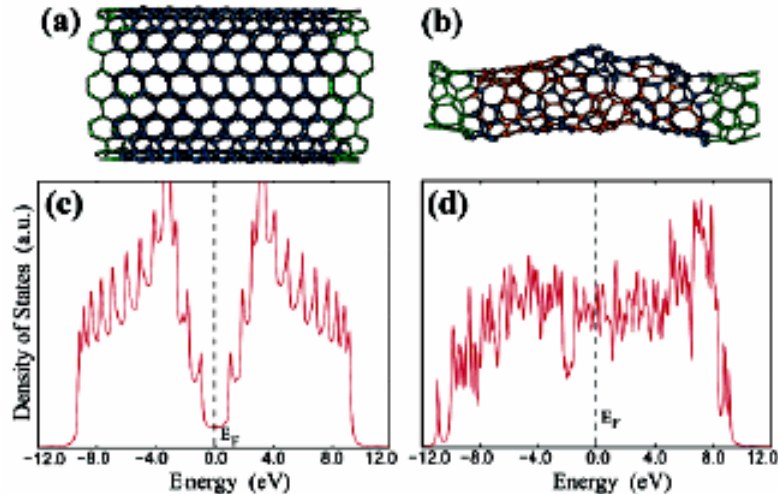


Figure 4-16. Surface reconstruction of (a) a (10,10) single-wall carbon nanotube ($\phi = 1.36$ nm) after a random extraction of 200 carbon atoms along the entire tube surface. Although the reconstructed surface is highly defective (b), the carbon system is still a rough cylinder, the diameter value of which is ~ 0.7 nm, containing 15 5/7 pair defects (in light brown). The corresponding electronic DOS are illustrated in (c) and (d) respectively [89].

Throughout the analysis of an array of nanotubes for skin friction measurements it has been assumed that the arrays of nanotubes are ordered in perfect geometry (Fig. 4-

16). It is possible to grow highly ordered arrays of nanotubes; however, some disorder will surely exist. Figure 4-17 displays the assumption where the geometry of the each nanotube is identical. It is widely known that the number of concentric shells and the outer diameters can vary from tube to tube. This assumption of r_{outer} equals $0.5r_{inner}$ was adopted as a medium between the two extreme cases where the nanotube is a thin hoop and the case where the thickness of the shell approaches r_{outer} . A similar reasoning is made with the using the average of the nanotube diameters. The one assumption which is a bit more difficult to validate is that the nanotubes are all equal length. This is not always the case. Accordingly, some of the shorter nanotubes would not be bonded to the sensor head. This would affect the electromechanical method in a positive manner by reducing the number of nanotubes in the electrical circuit. It could adversely affect the mechanics of the system by underestimating the maximum deflection of the sensor head.

All of these potential uncertainties were realized at the onset of the analytical design of both measurement techniques. Due to non-existent methods of avoiding these uncertainties the calculations were carried out using the mentioned assumptions.

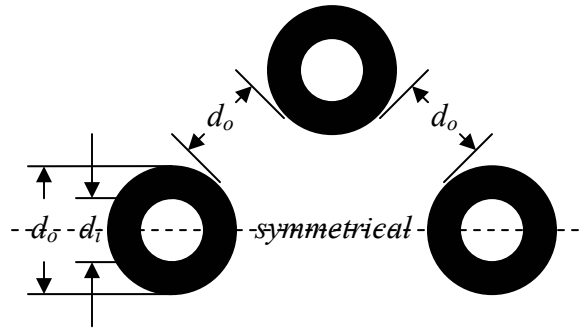


Figure 4-17. Schematic representation of perfectly spaced nanotubes with identical geometries.

5. FABRICATION OF TABLE TOP DESIGNS

This chapter informs the reader of the fabrication process of each design concept that was proposed in Chapter 4. Some of the information such as bonding agents and bonding techniques are proprietary, thus details are not supplied in this thesis.

5.1 Electromechanical Measurement Design

5.1.1 *First Concept Attempt*

The fabrication of a shear sensor which utilizes the electromechanical properties of carbon nanotubes was first attempted. The sensor was designed to have two arrays of nanotubes grown on $\frac{1}{4} \times \frac{1}{4}$ inch silicon substrates. The dimensions of the nanotubes ordered (D=80 nm, L=10 μ m) were found in Chapter 4 to produce a measurable change in resistance. These substrates containing the arrays of nanotubes were then to be bonded to glass. The electrochemical method of growing arrays of aligned MWNTs that NanoLab suggested requires a growth temperature of 600°C. Due to such high growth temperatures, the silicon wafers can no longer be bonded to glass because these bonds are designed to withstand temperatures of 300°C. Quartz was chosen as a replacement for the glass slide.

Three independent approaches were taken. The first was to test the bond between silicon and quartz by heating the sample to the growth temperature of the nanotubes, 600°C. The second advance was to grow nanotubes on diced silicon wafers and then attempt to bond them to glass or quartz. The last approach was to bond the silicon wafer to quartz using Ionically Self Assembled Monolayer (ISAM) technique.

From this three pronged approach, the most practical of the methods is growing the nanotubes on diced silicon first and bonding them to quartz second. When the test samples on quartz were heated to 600°C the bonds failed just as in the silicon on glass case.

Two identical samples were then sent to Applied Nanotechnologies for the sensor head attachment. Attempts were made to bond a 0.25" x 0.55" x 0.5 mm piece of silicon to the tips of the aligned nanotube arrays. This is a proprietary technique, and the details are unavailable. Of the two samples, one attempted bond was successful, and one was unsuccessful. The unsuccessful bond failed and the sensor head broke off upon removal

CHAPTER 5 – FABRICATION OF TABLE TOP DESIGNS

from the oven. Figure 5-1 displays SEM images of the successful bond. It appears as though the nanotubes are supporting the silicon sensor head. An approximate thickness of the bond was found using the SEM to be 25 microns. This is much greater than was anticipated. All SEM images were taken at Virginia Tech using a LEO 1550 Scanning Electron Microscope. LEO 1550 is a high performance Schottky field emission SEM a resolution of 2 – 5 nm depending on the sample.

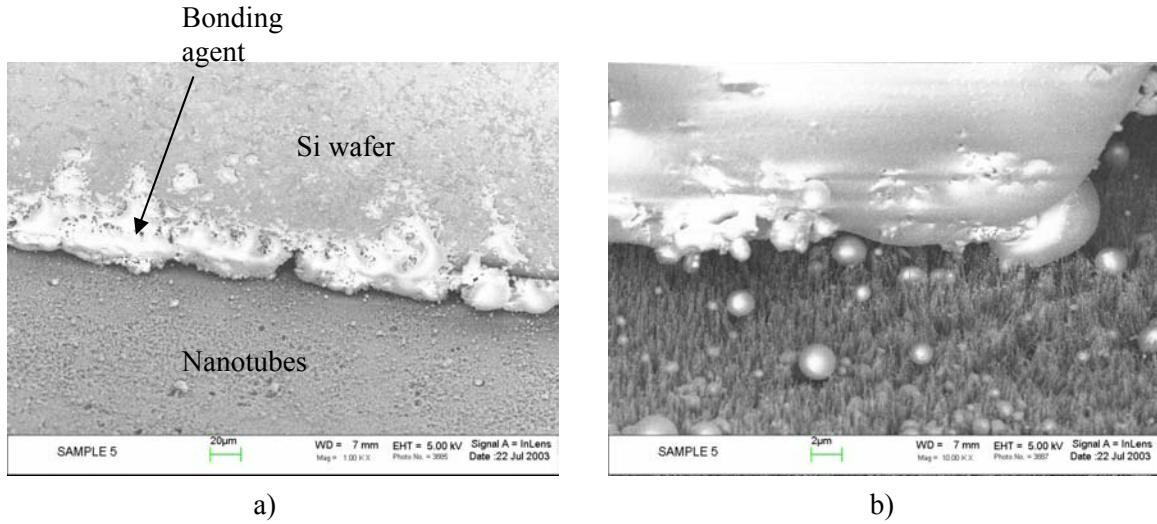


Figure 5-1. SEM images of successful sensor head bond at magnifications of 1Kx (a) and 10Kx (b).

After SEM images were taken of the successful bond, a bench test was conducted at Luna Innovations to determine if the sensor head was free to displace. A schematic and photograph of the setup can be seen in Figure 5-2. The sensor was secured to a fixed positioning stand between two optical fibers and a capillary tube. The two optical fibers were secured to fixed positioned stages. One fiber interrogates the sensing element while the second monitors the silicon substrate base. The two-fiber setup will give a displacement relative to the substrate. A quartz capillary tube with inner and outer diameters of 320 microns and 426 microns was mounted to a tri-axis linear positioning stand.

A microscope (50x) was used to align the capillary tube with the sensor head. The capillary tube was then slowly positioned so that a force was applied to the sensor head. A free-floating sensor head would be free to displace under the applied load. Figure 5-3 is a photograph taken of the capillary tube applying a force to the sensor head. As seen the capillary tube is buckling, indicating the sensor head is not free to displace.

CHAPTER 5 – FABRICATION OF TABLE TOP DESIGNS

This leads one to conclude that the attempted bonding of the sensor head to the nanotubes was not successful in producing a free-floating sensing element.

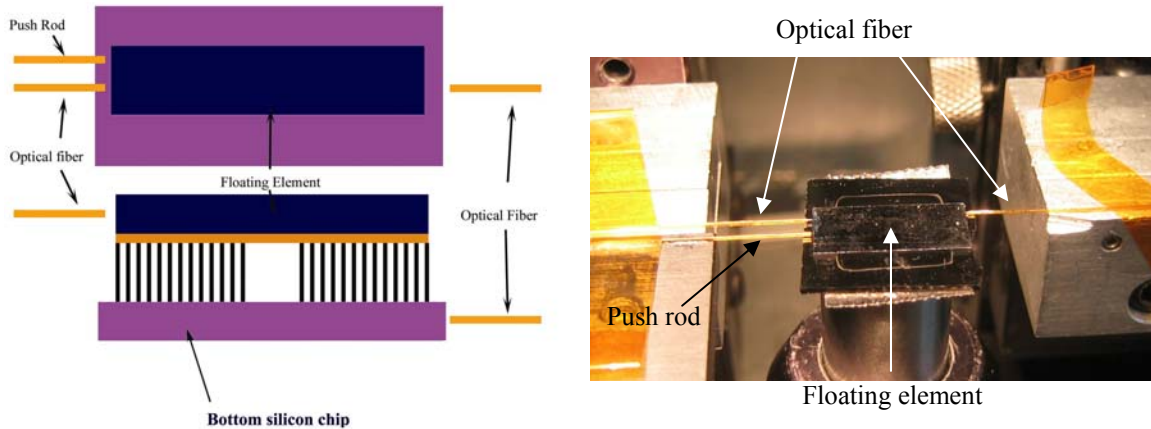


Figure 5-2. Schematic illustration and photograph of bench test to determine if sensing element is free to displace.

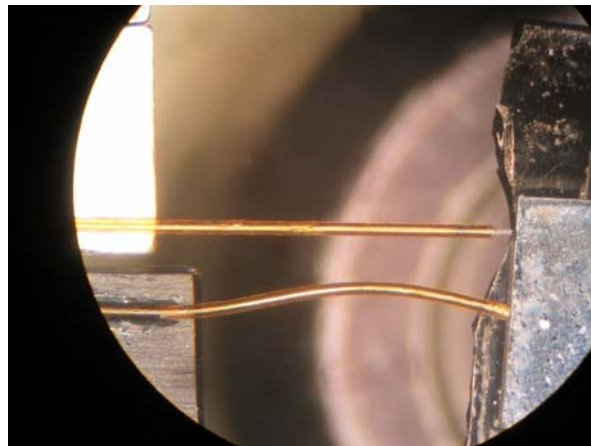


Figure 5-3. Photograph of optical fiber monitoring sensor head and buckled quartz capillary tube.

5.1.2 Second Concept Attempt

A chromium electrode mask was designed and laid onto a glass substrate by NanoLab to electrically isolate a small number of the nanotubes (Fig 5-4). Only nanotubes grown on the chromium electrode strip would electrically participate in the system. The side chromium deposit in contact with the electrode strip is used to connect the wire leads to the rest of the circuit. The center chromium deposit is 0.25 x 0.25

inches and was masked because nanotubes have better growth on chromium than bare glass. Nanotubes are grown on the translucent peach pattern of the substrate.

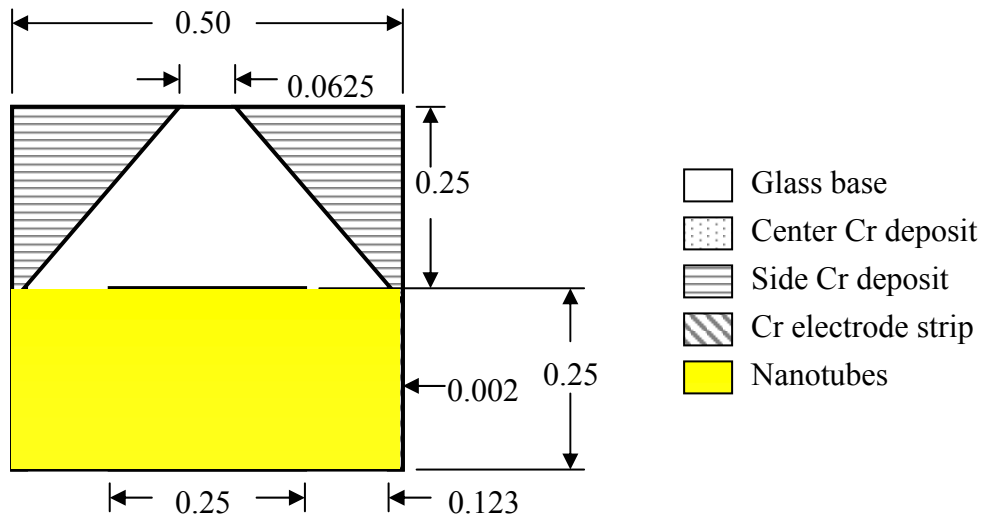


Figure 5-4. Schematic drawing of the electrode mask on glass to electrically isolate nanotubes.

This mask was then sent to NanoLab to grow an array of nanotubes using the electrochemical technique. Again, the dimensions of the nanotubes ordered were found in Chapter 4 to produce a measurable change in resistance. The nanotubes are grown on the front 0.5 x 0.25 inch section, indicated in translucent peach. SEM images were taken of the masked sample with nanotubes before the attempt was made to bond a sensor head (Fig 5-5). From Figure 5-5a it can be seen that the electrode strip is 100 microns wide. This is twice the thickness of the strip indicated in the above drawing. A SEM image of the forest of nanotubes grown on the electrode strip is displayed in Figure 5-5b. The forest is of poor quality, because the nanotubes are not straight or completely aligned. The spacing between neighboring tubes is also much closer than what was requested.

Several unsuccessful attempts were made at Luna Innovations to bond a sensor head to the 0.5 x 0.25 inch array of nanotubes. In each case, the bond did not secure the sensor head to the tips of the nanotubes. Due to problems of bonding a silicon wafer to the tips of an array of carbon nanotubes, this measurement method was abandoned.

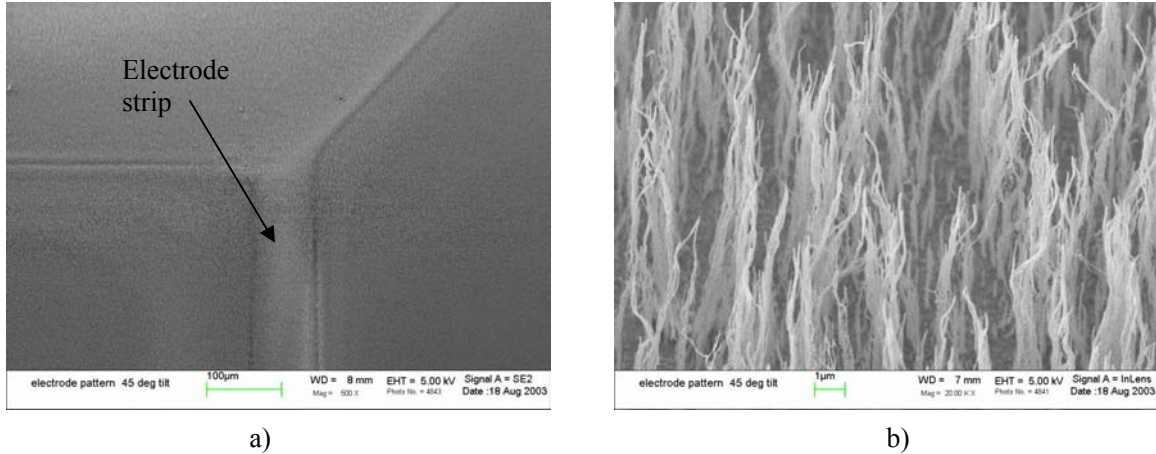


Figure 5-5. SEM images of the patterned electrode strip (a) and the nanotube forest grown on the electrode strip (b).

5.2 Mechanical Measurement Design

5.2.1 Aligned MWNT Concept

The mechanical measurement technique of using an array of aligned carbon nanotubes as a flexure was investigated. Due to problems with bonding as indicated in the electromechanical measurement section, this measurement method was not pursued further.

5.2.2 Aligned MWNT Structures

Upon contacting Dai (the author of Ref. [88]), it was learned that he no longer grows such structures as his research has lead him in other directions. This method of measuring skin friction was then abandoned here. It should be noted that these structures looked very promising to the application of measuring skin friction due to the ability to precisely control the dimensions in a variety of patterns.

5.2.3 ‘Lift-Up’ Growth Concept

A circular piece of silicon with a radius of 2” and thickness of 1 mm was ordered by Luna Innovations. It was decided to dice the piece of silicon into 1 x 1 cm squares to produce 60 total substrates. The circular Ni patterns would be masked in a 2 x 2 mm area in the center of the substrate. Figure 5-6 displays the plans for dicing and masking the patterned Ni on to the individual silicon substrates. According to the theoretical

CHAPTER 5 – FABRICATION OF TABLE TOP DESIGNS

calculations, the maximum displacement of an 80 x 80 array is approximately 300 nm under a 250 Pa shear load. Given the uncertainty in the calculations, four different array patterns were designed to increase the chance of fabricating a reliable skin friction sensor. Table 5-1 lists the theoretical displacements for each array.

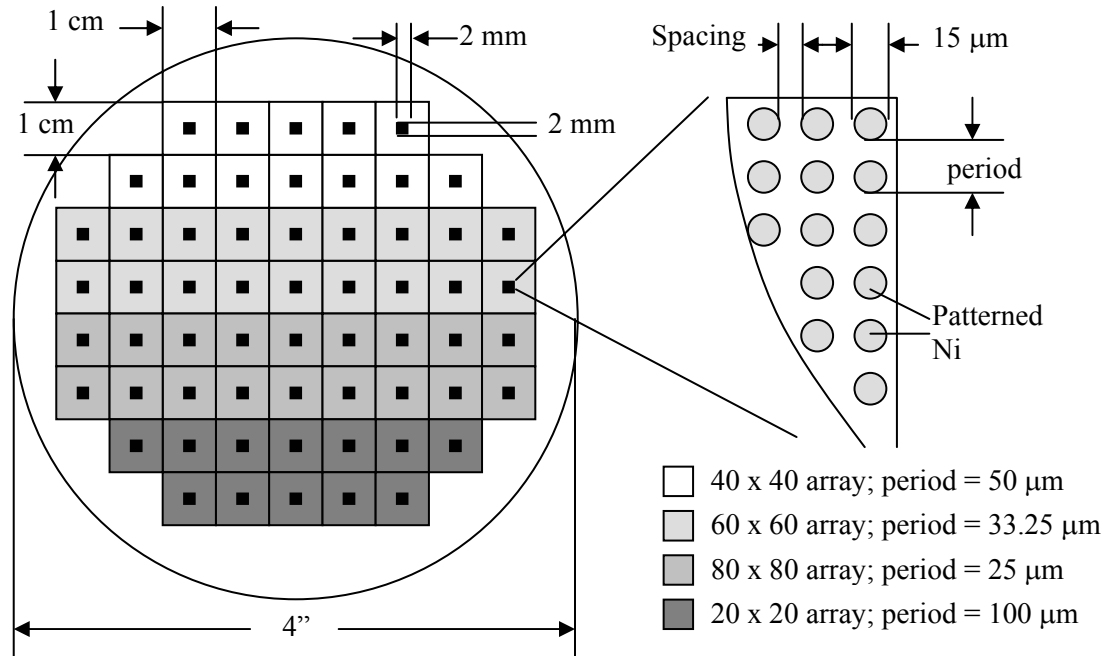


Figure 5-6. Dimensions of diced wafers and Ni film to be patterned on wafers.

Table 5-1. Theoretical displacements based on array size.

Array Size	Period (μm)	Spacing (μm)	Displacement (nm)
80 x 80	25	10	495
60 x 60	33.25	18.25	875
40 x 40	50	35	2000
20 x 20	100	85	7900

The fabrication process of patterned arrays of aligned MWNTs began at Microtronics located in Newtown, Pennsylvania. Microtronics produced a mask given the dimensioned drawings (Fig. 5-6) of the pattern on which the Ni film is to be laid on the 1 x 1 cm silicon substrates. The mask was then sent to Shipley, located in Blacksburg, Virginia, who exposed the mask and patterned the Ni film on the silicon via conventional photolithography (Fig. 5-7). After this was complete, the piece of silicon

was diced into sixty 1 x 1 cm squares. Shipley also diced and polished the edges of the 2 x 2 mm silicon sensor head such that the pieces would reflect light from the fiber optic system. The masked substrates along with the 2 x 2 mm silicon sensor heads were then sent to Dr. Wei at Louisiana State University for nanotube growth.

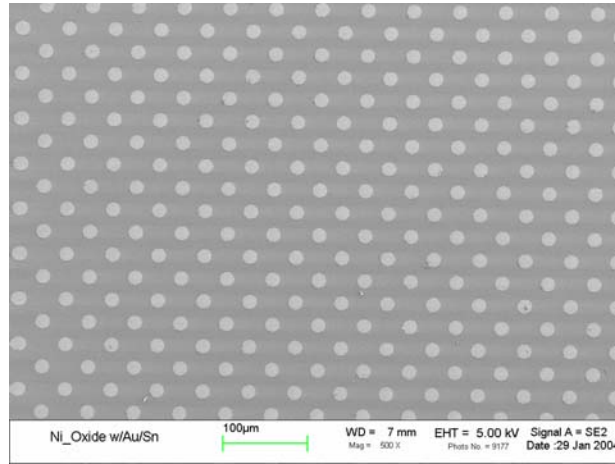


Figure 5-7. SEM images of patterned Ni film with spacing of 35 microns from edge to edge (500 x). Green scale is 100 microns in length.

Once the mask reached Shipley an alteration was made in the metal selection to pattern. Due to bonding issues between Ni and silicon, it was suggested that three different metal patterns be laid; Ni + oxide, Ni + oxide with Au/Sn, and Cr + Ni on oxide. This advice was followed.

The silicon substrates were received from Dr. Wei along with a summary of the carbon nanotube growth. Seven attempts were made to grow aligned nanotubes via CVD on four types of substrates (the three mentioned above and on bare silicon chips). A brief summary of the results follows:

5.2.3.1 Ni + oxide Substrate

It was noted by Dr. Wei that upon arrival, the substrates contained many impurities (Fig 5-8a). An attempt was made to remove the impurities by a sonication process in acetone for approximately 5 minutes. This sonication process failed to cleanse the substrates, and it also partially detached the Ni layer from the silicon. Runs at two

temperatures (770°C and 730°C) were conducted. During both runs the patterns melted into small blocks, and no nanotubes were grown (Fig. 5-8b).

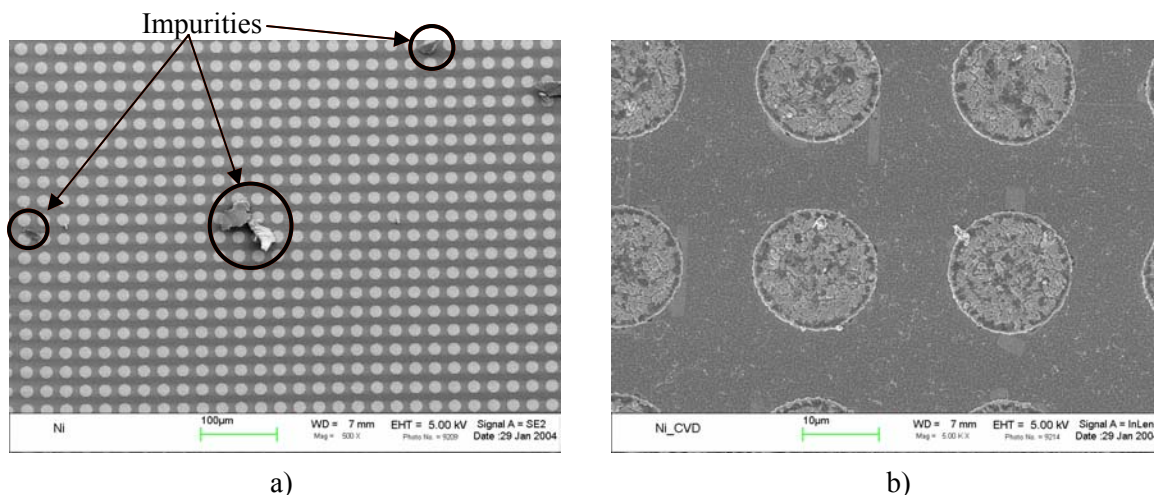


Figure 5-8. SEM images of Ni + oxide samples (a) with impurities before growth (500x) and (b) after CVD growth process (5Kx).

5.2.3.2 Ni + oxide with Au/Sn Substrate

Some nanotube bundles grew on the Ni + oxide with Au/Sn samples. One of these bundles can be seen in Figure 5-9. The structure is not aligned vertically with the substrate. The other patterns in the background of the figure have little or no growth. One suggested possibility of the poor growth is that the layer of Au/Sn laid on top of the Ni is too heavy for the nanotubes to lift up.

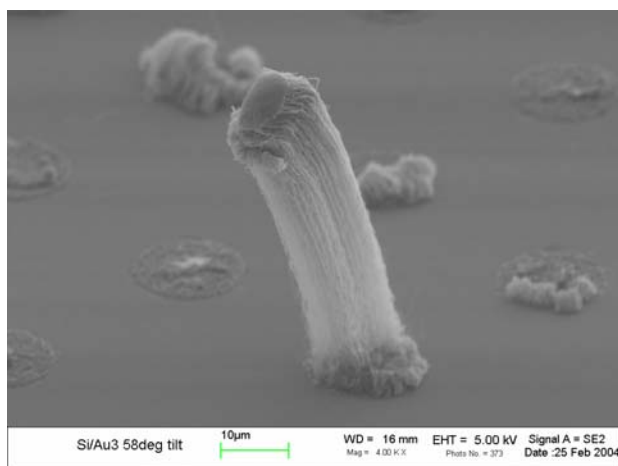


Figure 5-9. SEM image of a bundle of nanotubes grown on the Ni + oxide with Au/Sn sample (1.5 Kx magnification).

CHAPTER 5 – FABRICATION OF TABLE TOP DESIGNS

5.2.3.3 Cr + Ni + oxide Substrate

No aligned nanotube structures grew from the patterned Cr + Ni on oxide samples for unknown reasons (Fig 5-10). A few stray bundles of nanotubes were grown which lay flat on the substrate.

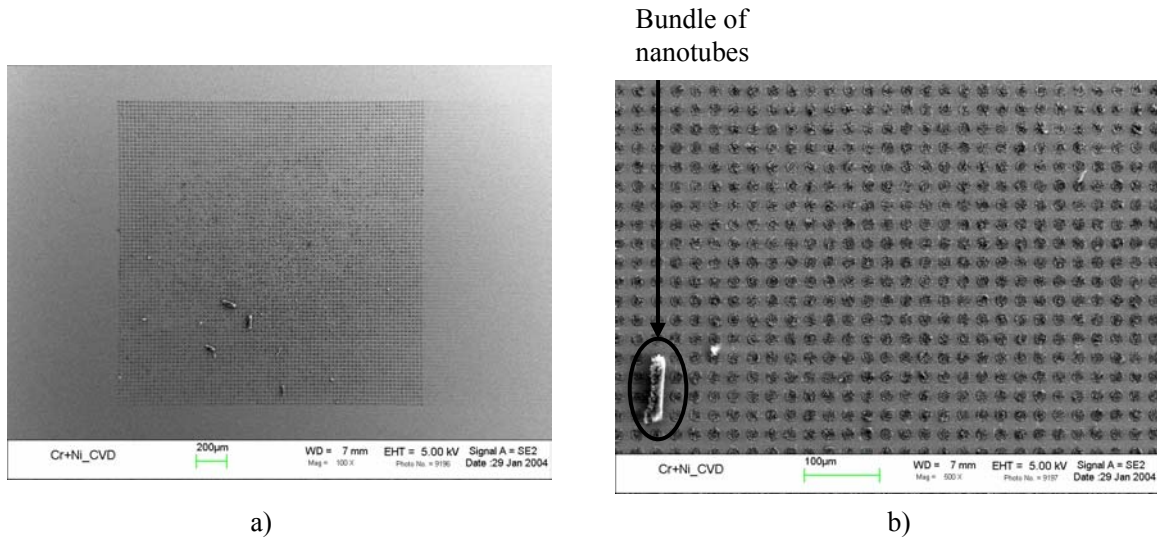


Figure 5-10. SEM images of Cr + Ni on oxide samples (a) at 100x and (b) 500x magnification.

5.2.3.4 Bare silicon chips

Nanotubes were grown on the 2 x 2 mm silicon chips with no pattern. The nanotubes are aligned and under a layer of amorphous carbon (Fig. 5-11a). Figure 5-11b shows a side view of the aligned nanotubes which grew to a height of 75 microns.

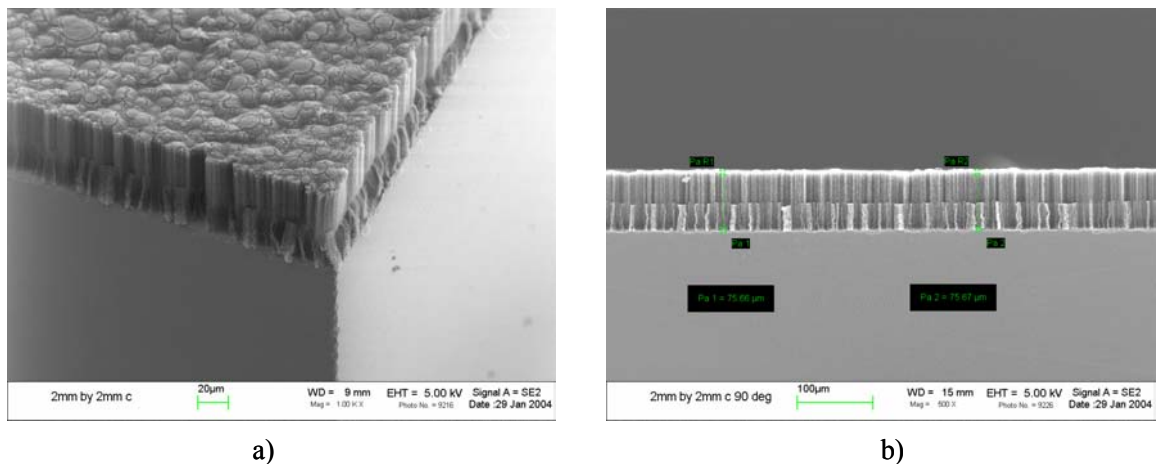


Figure 5-11. SEM images of (a) oblique view (1Kx) and (b) side view (500x) of aligned nanotubes grown on bare silicon chips. The height of the aligned nanotubes is approximately 75 microns.

CHAPTER 5 – FABRICATION OF TABLE TOP DESIGNS

The details of why aligned nanotubes grew on the bare silicon chips are unclear. However, it was stated that the feed gas used in the CVD growth process did contain Fe particles which are necessary for nanotube growth. It should be noted that it was not intended to grow nanotubes on the 2 x 2 mm silicon chips. These chips were the sensor heads to be bonded to the patterned arrays of nanotubes which grew on the 1 x 1 cm substrates. Since the other samples failed to produce aligned nanotube architectures, the fabrication process continued with these chips.

The next step in the fabrication of a nanotube shear sensor was to bond the amorphous layer of carbon to a bare 1 x 1 cm silicon substrate (Fig 5-12). This layer of carbon provides a semi-solid surface to bond to instead of bonding to the tips of the nanotubes. A proprietary bond technique with a strain gage epoxy was used to complete this process. Figure 5-13 is a SEM image of the nanotube array bonded to the silicon substrate

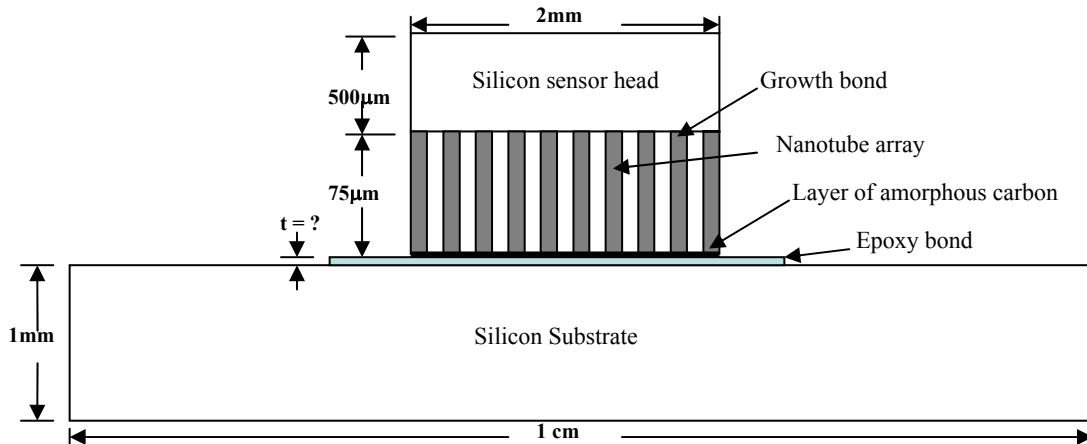


Figure 5-12. Schematic illustration of product after bonding process.

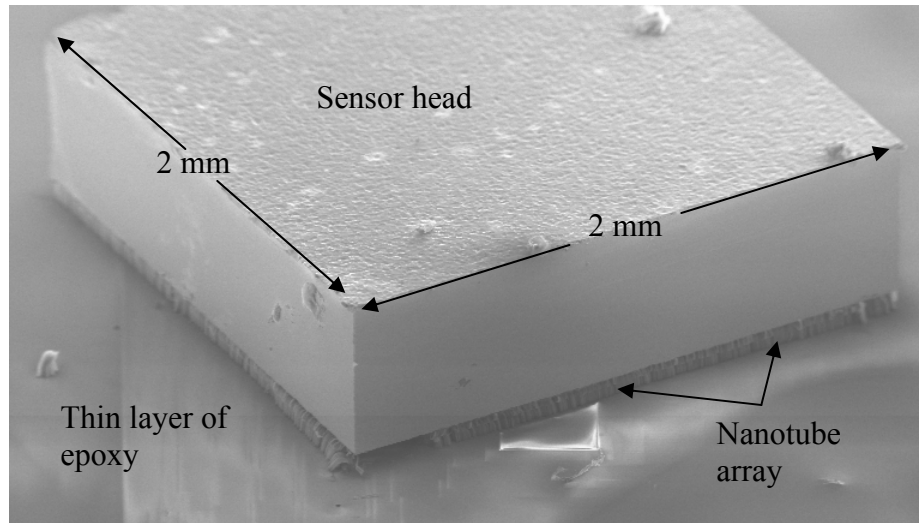


Figure 5-13. SEM image of the carbon nanotubes bonded to a silicon substrate with a strain gage epoxy.

After the bonding process was complete an optical fiber was attached to the silicon substrate to monitor the sensor head displacement (Fig. 5-14). This fiber would then measure any gap changes of the sensor head relative to the silicon substrate. The fiber was bonded with Litton Poly Scientific 222-4 epoxy so that the measured gap distance was in the optimal range of the fiber optic interferometry system (50 – 125 μm). The bond was then cured at temperature for duration of time while monitoring the gap so that it did not drift beyond the above range or sacrifice the quality of the fringe pattern. Once the bond cured, a robust juncture between the optical fiber and silicon substrate remained.

5.3 Sensor Housing Design

It is necessary to design a means by which the fabricated sensor can be introduced into the wind tunnel. This was done by designing a plug which holds the sensor and housing for the plug which attaches to the test section floor plate of the facility (Fig. 5-14). Using existing plug housing and floor plate, the sensor plug was designed. Figures 5-15 through 5-17 are dimensioned drawings created in Mechanical Desktop of the existing plug housing and floor plate, and the designed sensor plug. All machined components are constructed from aluminum and were machined at the Aerospace Engineering machine shop at Virginia Tech.

CHAPTER 5 – FABRICATION OF TABLE TOP DESIGNS

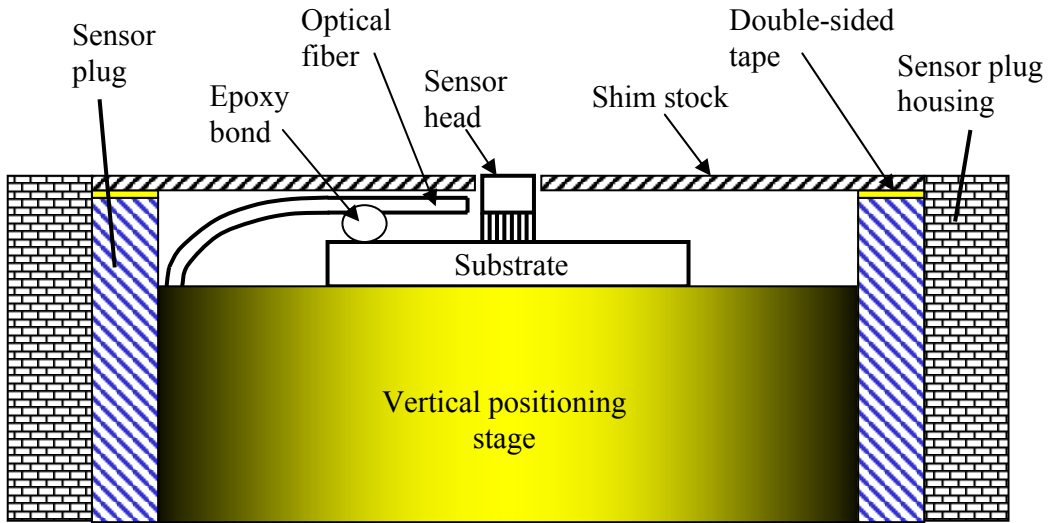


Figure 5-14. Schematic of sensor in the wind tunnel housing arrangement. Note: not to scale.

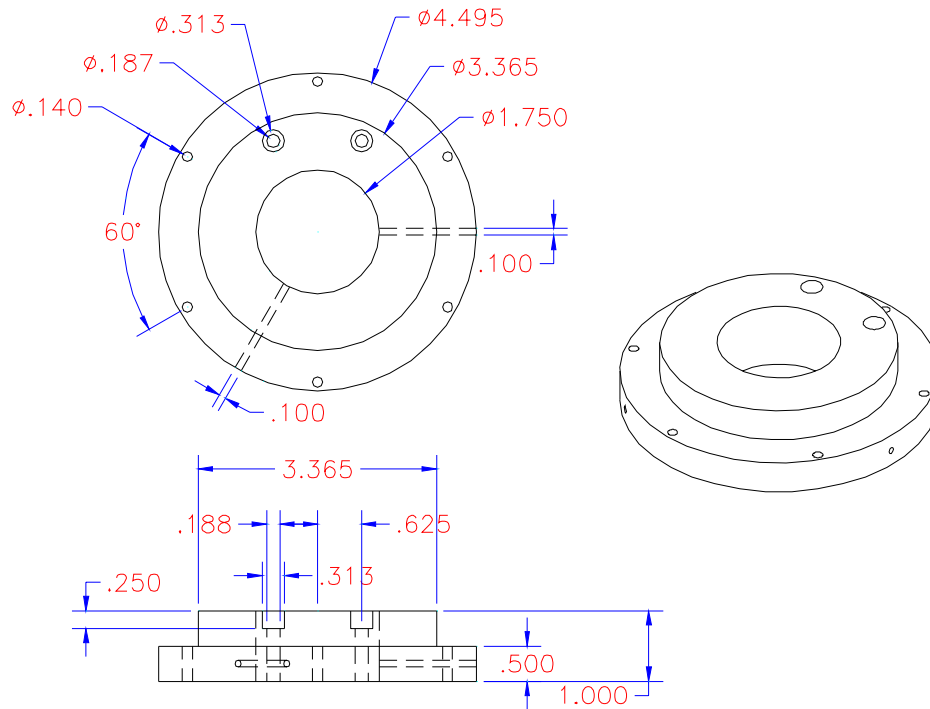


Figure 5-15. Drawing of sensor plug housing (Dimensions in inches).

CHAPTER 5 – FABRICATION OF TABLE TOP DESIGNS

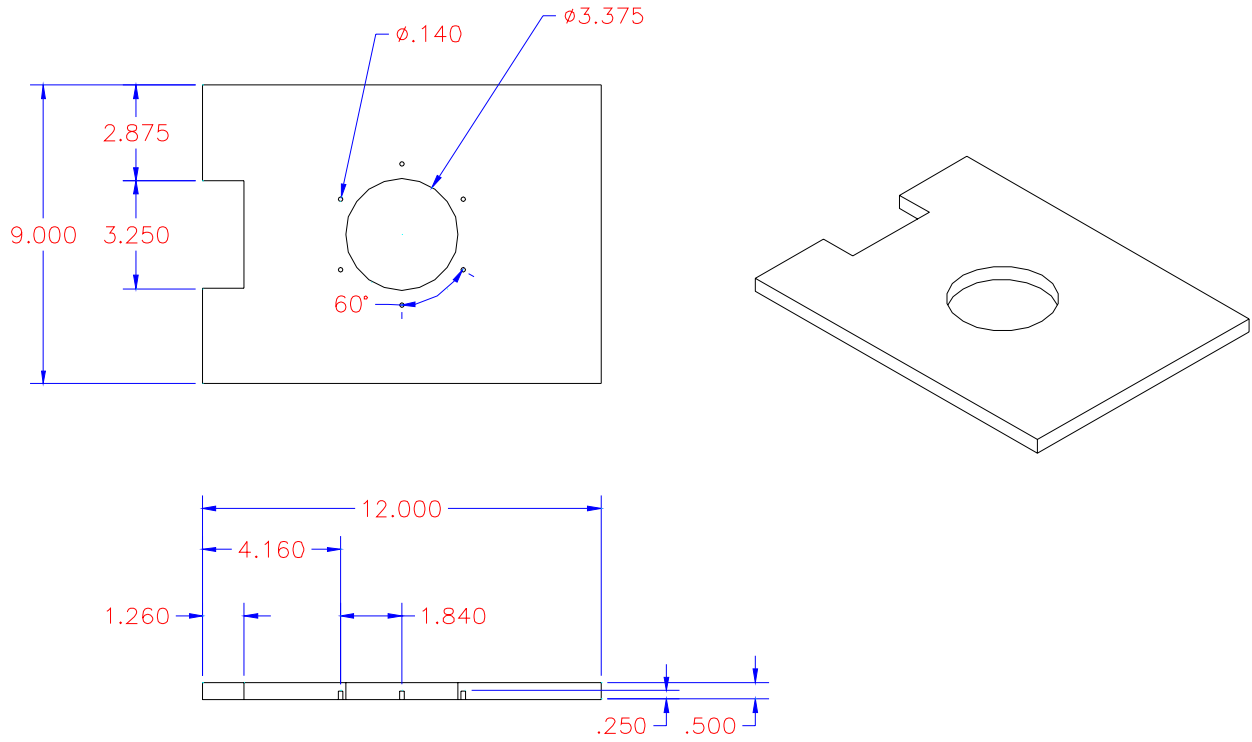


Figure 5-16. Drawing of test section floor plate (Dimensions in inches).

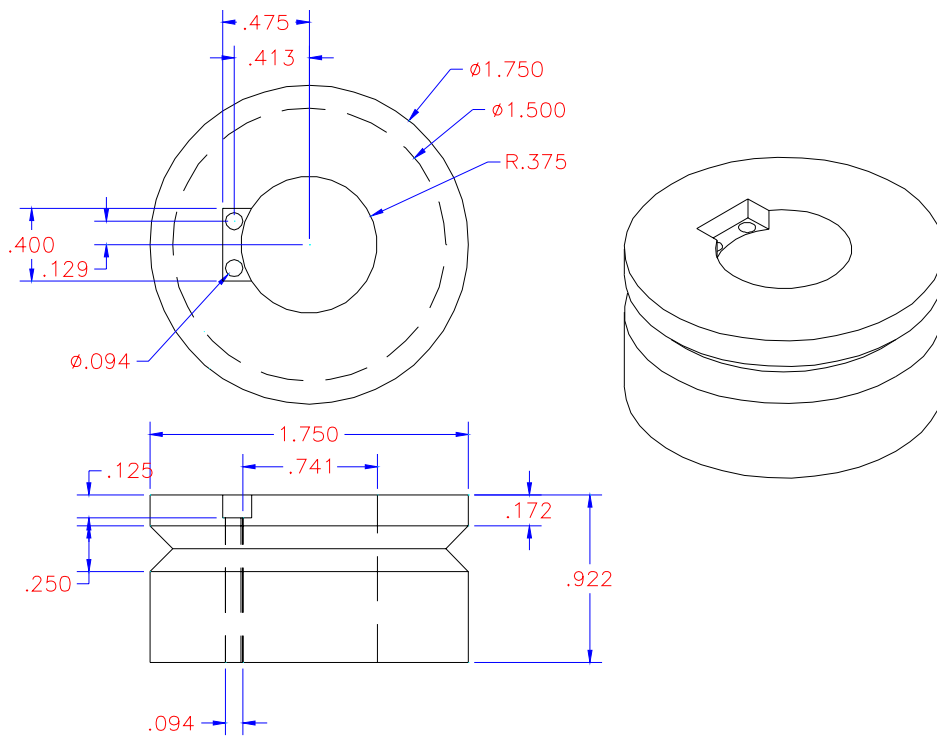


Figure 5-17. Drawing of sensor plug (Dimensions in inches).

CHAPTER 5 – FABRICATION OF TABLE TOP DESIGNS

Figure 5-18 is a photograph of all the components needed to integrate the sensor into the wind tunnel. The components are the positioning system, the shaft, sensor plug, plug housing and bolts. The positioning stage used in this assembly is a model UMR5.25 single-axis linear positioning stage made by Newport Corporation. It is capable of 20 mm of travel and positioning accurate to ± 10 microns (± 0.0004 ”). This allows precise alignment of the sensor head height after the gage is assembled.

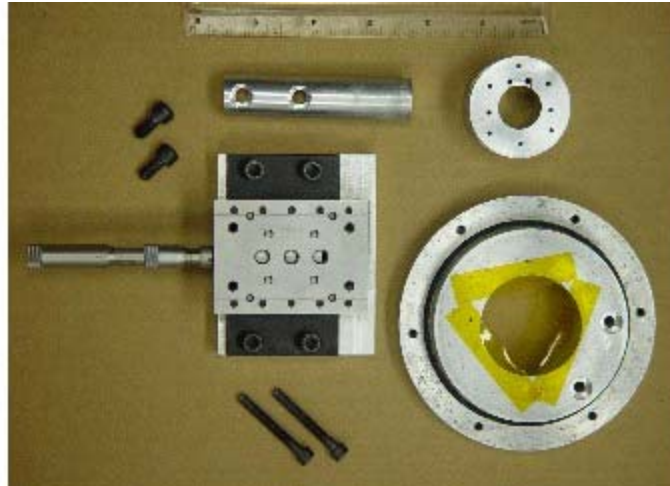


Figure 5-18. Photograph of gage components with 6” scale.

To create a flush surface between the sensor head and sensor plug housing, 0.005 inch thick stainless steel shim stock was cut into circular templates (Fig. 5-19). The pieces were cut with a 100 Watt CO₂ laser in the CPES Power Electronic Integrated Packaging Lab of The Bradley Department of Electrical Engineering at Virginia Tech. To have flexibility in the positioning of the shim stock in case the sensor head is not exactly centered with the sensor plug, the pieces were cut with a diameter of 1.5 inches instead of 1.75 inches. In the center of the piece a 0.088 x 0.088 inch hole is cut for the sensor head. This gives an allowance of 0.004” on each side of the sensor head. After the pieces are cut any roughness along the edges are eliminated with 400 grit sandpaper. Figure 5-20 is a photograph of the final shim stock product.

CHAPTER 5 – FABRICATION OF TABLE TOP DESIGNS

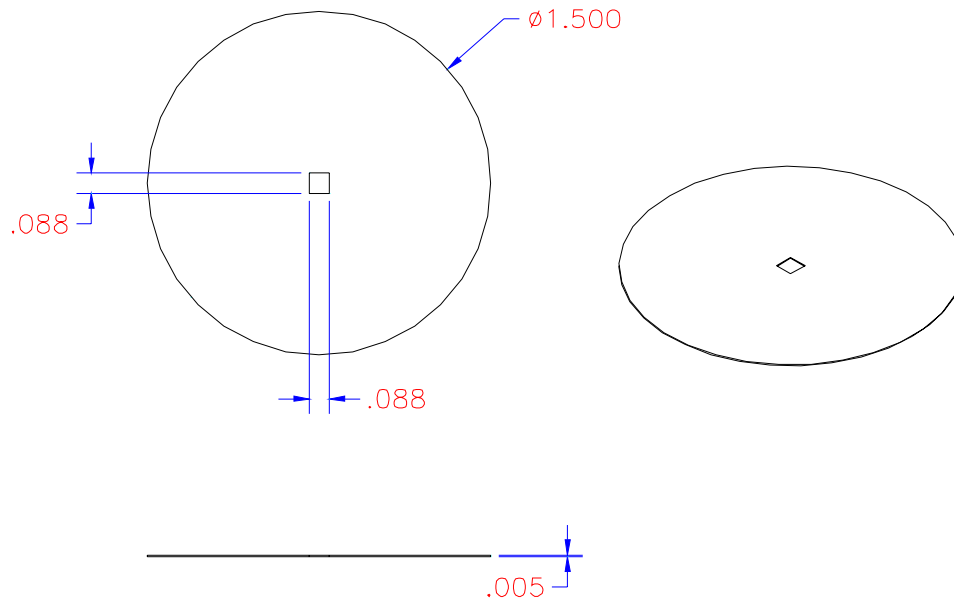


Figure 5-19. Drawing of shim stock (Dimensions in inches).

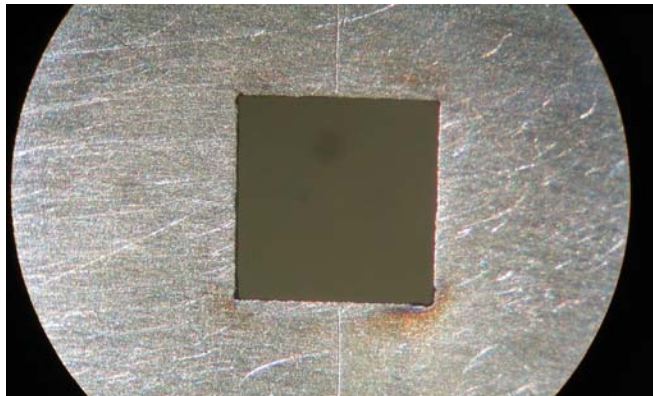


Figure 5-20. Photograph of shim stock taken through a 50x microscope.

The steps taken to assemble the vertical positioning stage, plug housing and sensor plug are described below:

1. Secure the positioning stage to the housing mount with four $\frac{1}{4}$ x $\frac{1}{2}$ inch socket head cap screws.
2. Fasten the 0.75" diameter shaft to the positioning stage with two $\frac{1}{4}$ x $\frac{1}{2}$ inch socket head cap screws.
3. Mount the positioning stage with shaft to the plug housing with two #10-32 x 1.5" socket head cap screws (Fig 5-21a).

CHAPTER 5 – FABRICATION OF TABLE TOP DESIGNS

4. Apply 3-in-1 oil to rubber gasket of sensor plug. Slide sensor plug into plug housing such that it is recessed approximately 0.005". Leave pointed set screws loose so that height of sensor plug can be altered after shim stock is fastened (Fig. 5-21b).
5. Using a lint free task wipe and Isopropyl alcohol, thoroughly cleanse top of the shaft and bottom of silicon substrate.
6. Fix sensor to shaft with double sided tape (~0.005" thick) using tweezers so that adhesive is not handled.
7. Using a lint free task wipe and Isopropyl alcohol, thoroughly cleanse top of sensor plug and shim stock.
8. Apply double sided tape to the top of sensor plug using tweezers so that adhesive is not handled. Double sided tape was chosen to secure the shim stock to the plug housing over epoxy do to the consistent thickness of the tape.

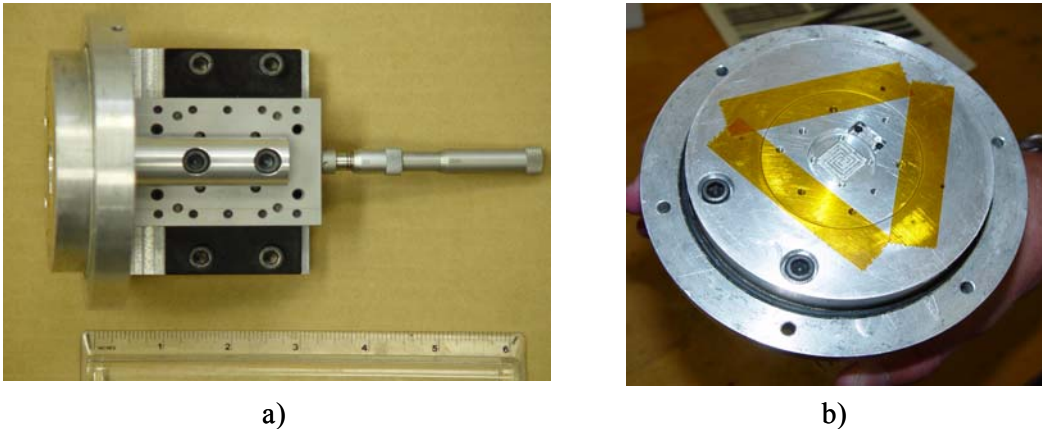


Figure 5-21. Photograph of gage assembly after (a) steps 1-3 (b) step 4.

9. Using a microscope (50x) the shim stock is secured to the sensor plug so that there is equal clearance on each side of the sensor head (Fig. 5-22).
10. Adjust sensor plug (without twisting) in plug housing so that the shim stock is flush with the plug housing. This can be checked using a straight edge. Tighten the two pointed set screws using a 0.05" Allen key. It is important to tighten the set screws equally since this could potentially alter the clearance of the sensor head/shim stock.

CHAPTER 5 – FABRICATION OF TABLE TOP DESIGNS

11. Fill in gap between shim stock and the plug housing with a hard wax that becomes pliable when handled. Fill the two holes on top of plug housing used to secure positioning system. With a razor blade, remove excess wax so that all surfaces are flush to the touch (Fig 5-23).
12. Fill in two holes in sensor plug for optical fiber and temperature sensor with a 5 minute epoxy. Ensure no leaks exist as they will allow outside air to funnel into test section during the wind tunnel testing.

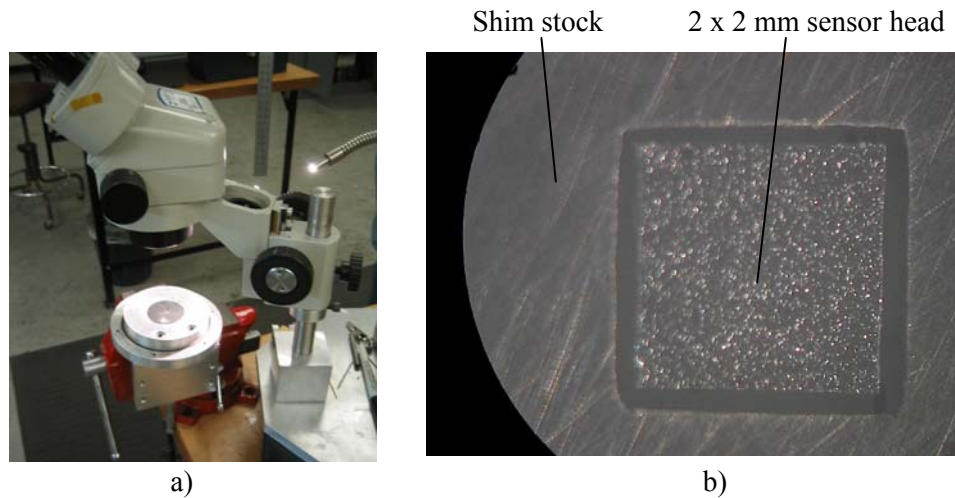


Figure 5-22. (a) Setup used to apply shim stock to sensor plug using microscope. (b) Photograph taken through microscope (50x) of clearance around sensor head (~0.003”).

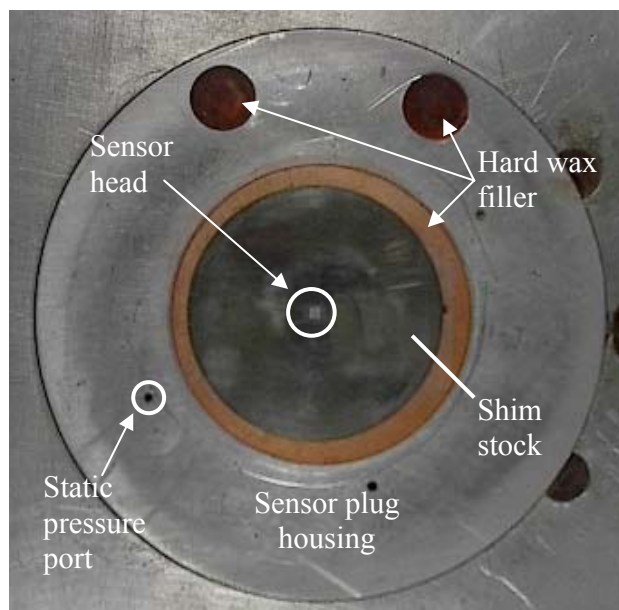


Figure 5-23. Photograph of the top view of the completed assembly.

5.4 Sensor Calibration

5.4.1 Displacement Sensor

The calibration process involves hanging known masses from the sensor head and measuring the resulting displacements. Six sensors were calibrated in the Optics Laboratory at Luna Innovations. Five of the sensors were calibrated before placement in the gage assembly. The sixth sensor was calibrated while in the gage assembly. It should be noted that calibrating the sensor once in the gage assembly is a time saving method because it skips intermediate steps in the setup of the calibration process. It also minimizes the handling of the sensor which decreases the probability of damaging the device. One additional sensor without nanotubes was calibrated to ensure that all measured displacements are due to the nanotubes bending and not shearing of the epoxy bond.

The setup of the calibration process was the same for each sensor. The sensor was bonded to a stage which was capable of rotating 360 degrees. Various methods of bonding were explored. These methods included using super glue, Phenyl Salicylate, and double-sided tape. Bonding the sensor to the stage using super glue is not recommended because it requires the use of acetone for removal. Two sensors were destroyed during their removal due to the nanotubes being exposed to the acetone. The Phenyl Salicylate is easily removed by heating the stage to the agents melting temperature (60°C). However, there is excess agent leftover which makes for a time consuming clean up. The preferable bonding method is double-sided tape because the adhesive bond is strong enough to hold the sensor throughout the calibration. The calibrated sensor is easily removed and cleaned after the process with a razor blade and Isopropyl alcohol on a lint free task wipe.

Once the sensor was secured to the stage a string was bonded to the sensor head using Phenyl Salicylate. The agent was heated to temperature and a small amount was applied to the string using a soldering iron. The string was then lightly touched to the sensor head so that the string was fastened. Extreme care was taken to not press the string against the sensor head since these devices are delicate. The other end of the string was fastened to a paper cone using fiber optic tape. The sensor was then tilted 90 degrees so that the cone hung perpendicular to the floor (Fig. 5-24).

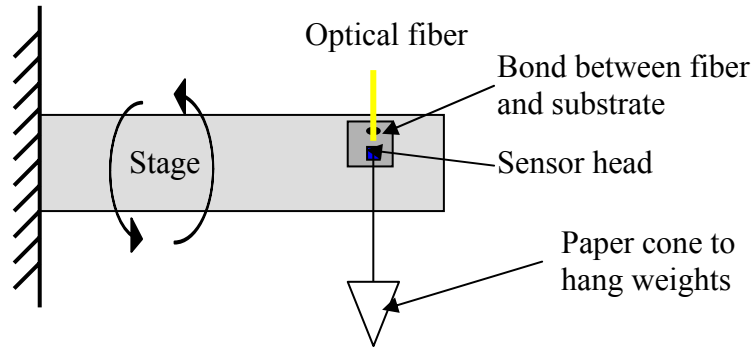


Figure 5-24. Schematic illustration of the calibration setup.

The equipment used in the data acquisition is a 533 MHz laptop and a Fiber Pro USB developed by Luna Innovations (Fig. 5-25). The Fiber Pro USB measures the absolute gap between the fiber and sensor head. Once the system is setup the user begins to save data. While the system logs the gap distance, known masses are placed in the paper cone. This data is saved to the laptop for analysis.

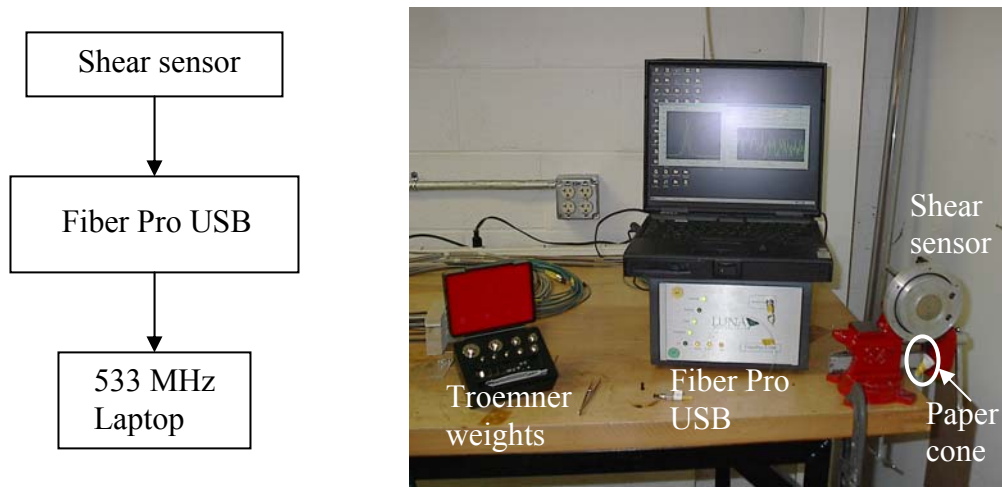


Figure 5-25. Diagram and photograph of calibration setup.

The weights used to calibrate the sensor are Troemner’s Alloy 8 Analytical style weights and range from 1mg – 100g. Only masses between 5 mg and 200 mg were used in the calibration process, with the total masses in the cone never exceeding 1g. A mass of 100mg corresponds to a shear level of approximately 250 Pa. The sensors were calibrated through several runs while varying the order of the masses applied to have a sufficient number of points. Table 5-2 displays the calibration points of one sensor. Four

CHAPTER 5 – FABRICATION OF TABLE TOP DESIGNS

separate runs were conducted to ensure the largest diversity of points. Figure 5-26 is a graphical representation of the calibration points from runs 1 – 4. The value R^2 is the coefficient of determination and is equal to:

$$R^2 = 1 - \frac{SSE}{SSM} \tag{5-1}$$

where, SSE is the sum of squared the errors (residuals) and SSM is the sum of squares about the mean [90].

Table 5-2. List of calibration run number, masses applied, and measured displacements ($R^2=0.98$).

Run Number	Mass (mg)	Averaged Gap (nm)	Force (N)	Shear (Pa)
1	0	-7.69144E-12	0	0
	5	2.844231064	0.000049085	12.27125
	15	8.880525604	0.000147255	36.81375
	35	20.08897167	0.000343595	85.89875
	55	28.93869273	0.000539935	134.98375
	95	56.24580131	0.000932615	233.15375
2	0	2.29446E-11	0	0
	45	21.49055847	0.000441765	110.44125
	95	48.79158929	0.000932615	233.15375
	115	59.51022588	0.001128955	282.23875
	135	69.0330578	0.001325295	331.32375
	145	75.36982372	0.001423465	355.86625
3	0	6.16697E-12	0	0
	45	32.1530872	0.000441765	110.44125
	55	36.80299358	0.000539935	134.98375
	105	64.3111569	0.001030785	257.69625
	110	67.57292572	0.00107987	269.9675
	130	77.98222404	0.00127621	319.0525
4	0	-1.26319E-11	0	0
	45	26.69587719	0.000441765	110.44125
	65	36.89020833	0.000638105	159.52625
	70	40.11833333	0.00068719	171.7975
	90	51.24157658	0.00088353	220.8825
	140	77.6578839	0.00137438	343.595
150	82.06960094	0.00147255	368.1375	

Averaged Gap Distance as a Function of Mass

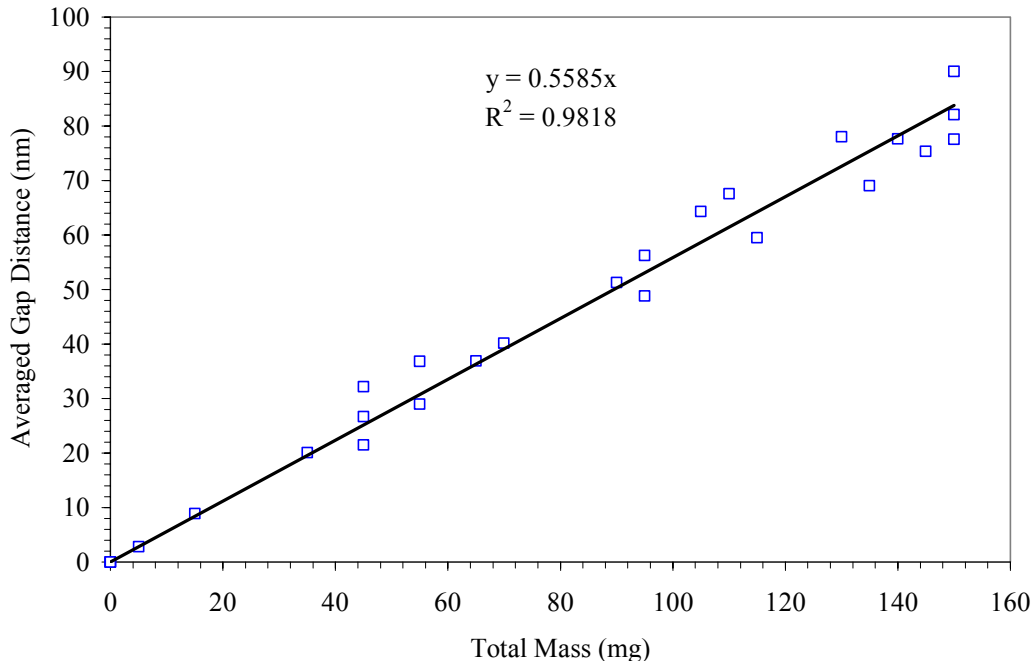


Figure 5-26. Plot displaying applied mass and measured displacement during calibration.

Once the calibration of the shear sensor was completed it was necessary to perform the same procedure on a sensor without an array of nanotubes. The 2 x 2 mm sensor head is bonded to the 1 x 1 cm silicon substrate using an identical procedure and bonding agent (Fig. 5-27). Figure 5-28 compares two sets of data for the bond calibration. During the run labeled ‘Applied masses’, masses of 1g, 500mg, 200mg, 200mg and 100mg were added every four seconds over the 20 second time interval. It can be seen that the two sets of data are equally random with no noticeable gap distance between the two. This indicates that the bond does not contribute to the distance the sensor head displaces.

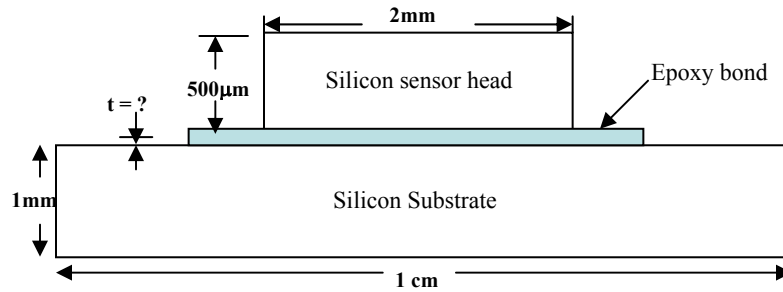


Figure 5-27. Schematic illustration of sensor without nanotubes.

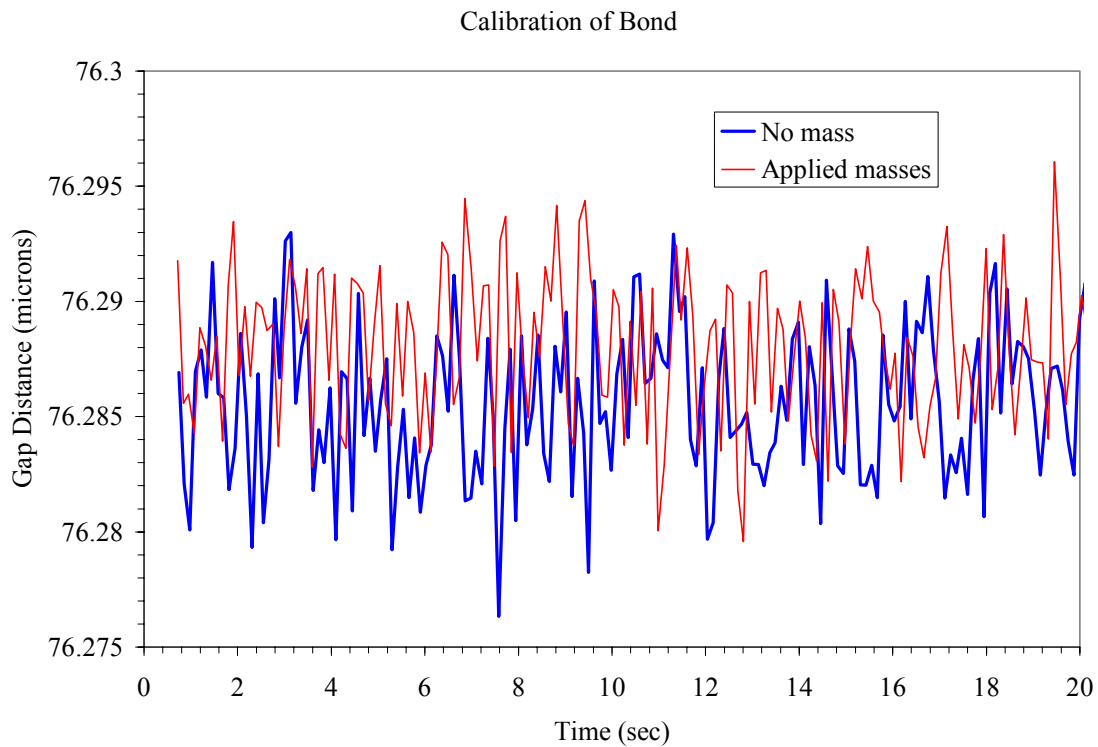


Figure 5-28. Plot displaying gap distance during calibration of sensor without nanotubes.

After the calibration process the string attached to the sensor head must be removed. This proved to be a difficult task, destroying three of the six sensors. The process was done in reverse. A soldering iron was heated to temperature and placed very close to the string/sensor head bond. This required a steady hand since any contact from the soldering iron to the sensor head could cause damage. Once the Phenyl reaches a certain temperature the string can be removed. If an attempt is made to remove the string prior to the Phenyl melting, the sensor head is ripped off. Any excess bonding agent on

the sensor head is removed by placing the soldering iron in close proximity to the residue. A small piece of a lint free task wipe is used to wick the excess agent off. Figure 5-29 is a photograph taken at 50x of the sensor head after the string and bonding agent removal.

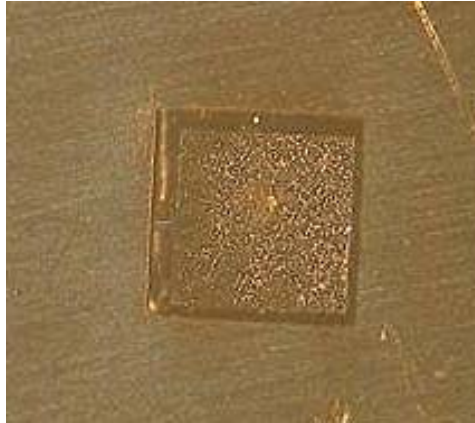


Figure 5-29. Photograph of sensor head positioned in shim stock after excess bonding agent was removed (50x).

5.4.2 Temperature Sensor

The temperature in the Virginia Tech Supersonic Wind Tunnel varies during a test run. These variations in temperature can directly affect the gap distance being measured by the displacement sensor. To compensate for possible temperature affects on the displacement measurements, a temperature sensor is incorporated into the design. The sensor is an EFPI Surface-Attachable/Embedment Temperature Gage with part number ET-TA-HA-01M-BP (Fig. 5-30).

The temperature sensor is mounted on the silicon substrate approximately 2 mm from the sensor head. It is bonded with Litton Poly Scientific 222-4 epoxy. Extensive care is taken to ensure no bonding agent came in contact with the sensing element or displacement sensor. Figure 5-31 is a photograph of the displacement sensor, temperature sensor, and sensing element. The calibration of the sensor took place at Luna Innovations using the same data acquisition setup as the displacement sensor.

CHAPTER 5 – FABRICATION OF TABLE TOP DESIGNS

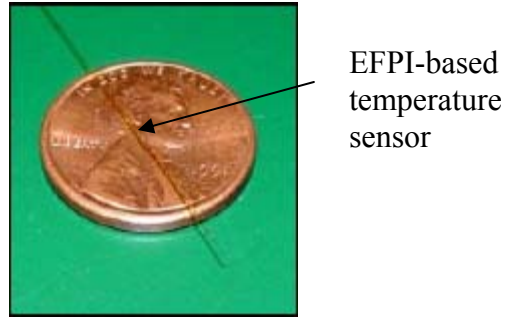


Figure 5-30. The EFPI Surface-Attachable/Embedment Temperature Gage [91].

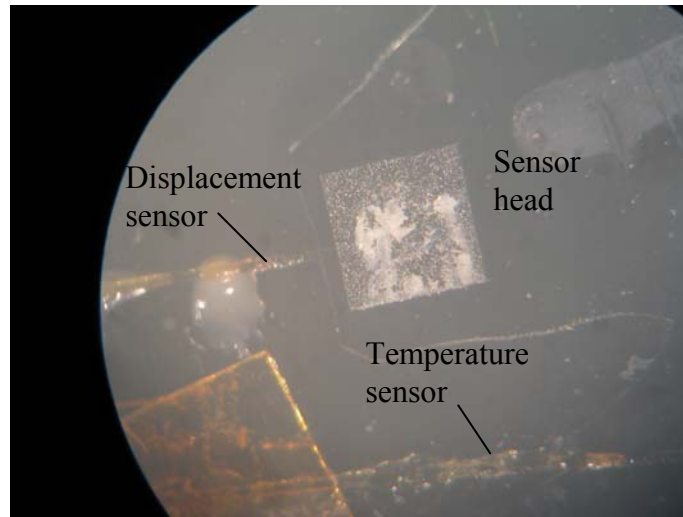


Figure 5-31. Photograph of displacement sensor, temperature sensor, and sensor head taken through 50x microscope.

6 SUPERSONIC WIND TUNNEL TESTING

6.1 Components of Supersonic Wind Tunnel Testing

6.1.1 *Supersonic Wind Tunnel*

The Virginia Tech Supersonic Wind Tunnel was used to test the performance of the skin friction gage (Fig. 6-1). This facility is a cold-flow wind tunnel which operates at a total temperature of approximately 300 Kelvin. A short description of the various components of the facility is presented below.

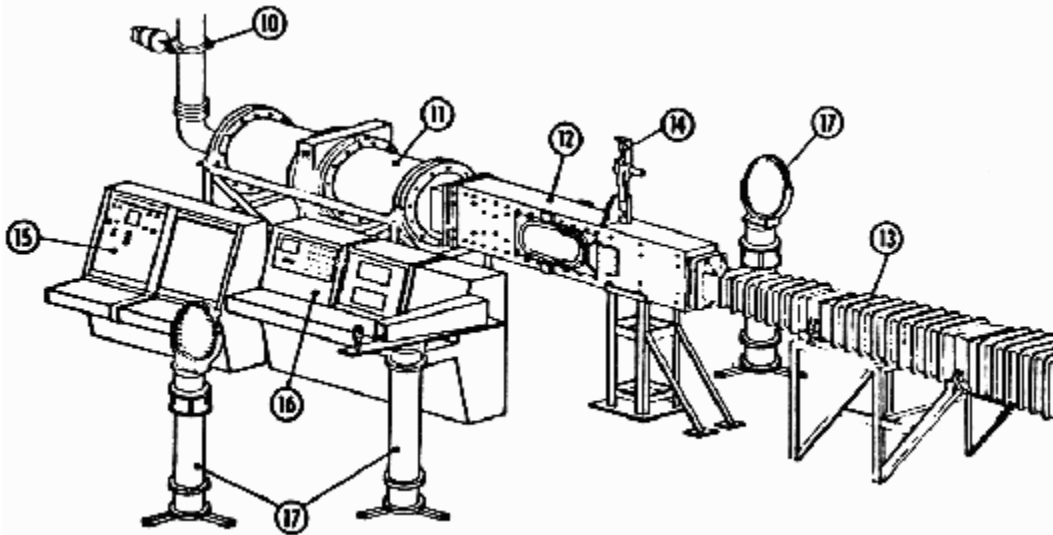


Figure 6-1. Virginia Tech Supersonic Wind Tunnel layout. 10 – Pressure Regulator, 11 – Settling Chamber, 12 – Test Section, 13 – Diffusor, 15 – Tunnel Control Panel, 16 – Measurement Panel [92].

The air storage system consists of two tanks with a total volume of 23 cubic meters. These storage tanks can be pressurized up to 51 atm by an air pumping system consisting of an Ingersoll-Rand Type 4-HHE-4 4-stage reciprocating air compressor driven by a 500 hp, 480V Marathon Electric Co. motor. Once the tanks are pumped to the desired pressure the airflow is controlled by a quick opening butterfly valve and a hydraulically actuated pressure regulating valve with a 30.5 cm diameter. The settling chamber contains a perforated transition cone, several damping screens, and probes used to measure the stagnation pressure and temperature [92].

The main pressure measuring system includes a PSI Model 780B electronically scanned pressure system. The system is IBM PC computer controlled and presently can handle 32 pressure inputs (0 to 1 atm) simultaneously but, if a need arises, it can be

CHAPTER 6 – SUPERSONIC WIND TUNNEL TESTING

expanded up to 512 pressure inputs. Pressure data rate is up to 20,000 measurements per second and the accuracy is 0.1% of span. In addition to the electronically scanned pressure system, there are two Scanivalve systems available, each allowing to record up to 48 pressures (0-3 atm) during a run of a few seconds duration. Temperature measurements can be made using an automatic multipoint thermocouple reference system and high-speed potentiometric recorders [92].

The data acquisition system consists of a 450 MHz PC with National Instruments 16 bit data acquisition card and multiplexer. This allows up to 32 channels at a sampling rate of up to 500 Hz. The data acquisition card used is the National Instruments NI 6031E. This PC is also responsible for controlling the wind tunnel and recording the pressure and temperature data using LabView software [92].

The test section has a 23 x 23 cm cross section with removable floor plate to provide testing capabilities to a wide range of models. The test section is sealed via two large doors containing windows to ensure optimal viewing. The flow conditions through the test section can be altered by changing the nozzle chamber and total pressure of the wind tunnel. The tunnel is equipped with three steel nozzle chambers to produce flows of Mach 2.4, 3.0 and 4.0. The stagnation pressure in the tunnel is variable between 3 – 20 atm. The length of test run is also variable depending on Mach number and static pressure.

6.1.2 Fiber-Optical Data Acquisition

The data acquisition used in the wind tunnel test is similar to that used in the displacement and temperature sensor calibrations. The 4 Channel Fast FiberScan system was used instead of the Fiber Pro USB so both sensors could be used simultaneously. This system measures the gap distance of the EFPI based displacement and temperature sensor. A 1.6 GHz Dell PC with Fiber Pro USB software logs the data at a sample rate of 900 Hz.

6.1.3 High-Speed Camera

A high-speed video camera was used to monitor the sensing element and visualize the tunnel starting throughout the wind tunnel testing (Figure 6-2). The camera is a

CHAPTER 6 – SUPERSONIC WIND TUNNEL TESTING

Phantom 4 produced by Vision Research Inc., used in conjunction with a 2.0 GHz laptop with Phantom software. It has operating limits of 1 – 30,000 pictures per second (pps). For the entirety of the wind tunnel tests performed, the operating speed of the camera was fixed between 200 – 500pps to ensure optimal quality and viewing window of the sensor. Figure 6-3 is a single frame taken during the initiation of flow through the test section.

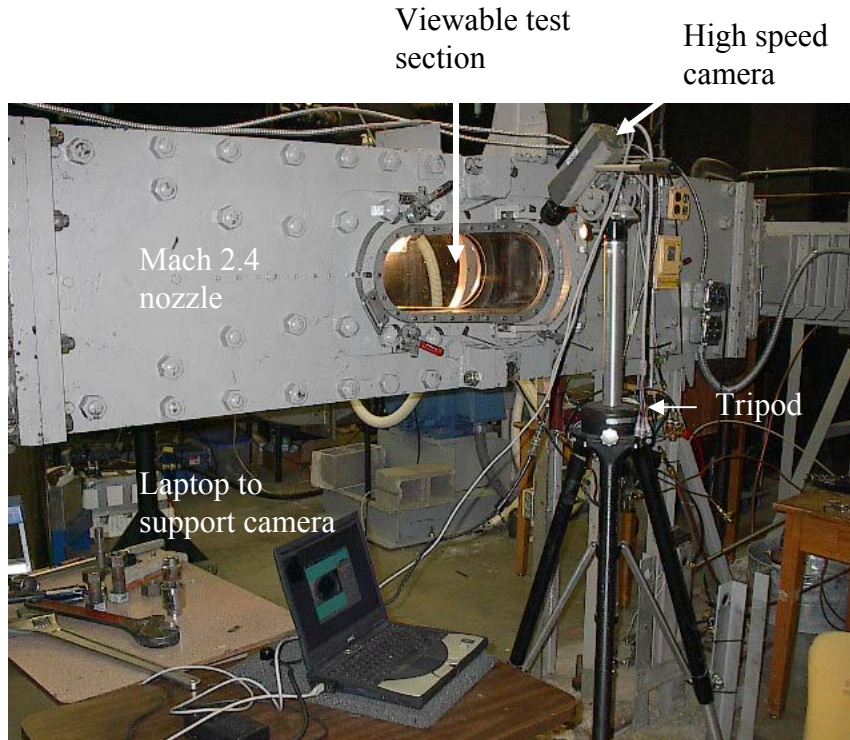


Figure 6-2. Photograph of high-speed camera setup.

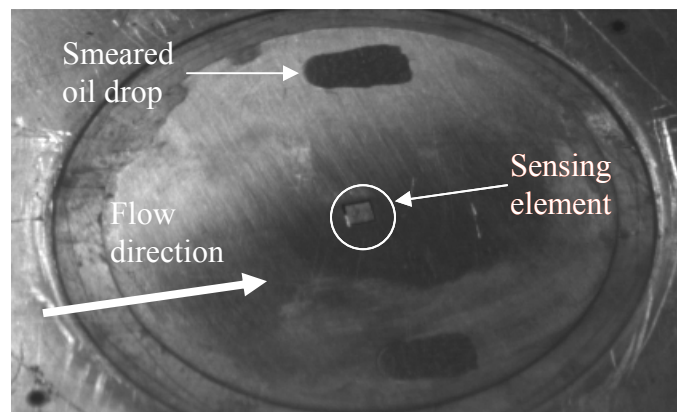


Figure 6-3. Single frame captured by high speed camera operating at 500pps during the start of the tunnel.

6.2 Test Setup

The Virginia Tech supersonic wind tunnel was used to evaluate the performance of the wall shear gage in a known flow. The wall shear ranges from approximately 150 – 300 Pa at Mach 2.4, depending on the total pressure of the tunnel. The most widely used flow conditions consist of a nominal Mach number of 2.4, a total pressure of 50 psia, a static pressure of approximately 4 psia, and a total temperature of 300 Kelvin. There is a large amount of experimental results from other wall shear gages in these flow conditions, which will serve as a method of comparison [3, 39, 43 – 46, 48, 93 – 95]. Also wall shear values have been documented in detail using both direct and indirect measurement methods [6, 49, 54, 57, 96 – 98]. For these reasons the gage will first be tested in the conditions listed above. The setup remains consistent regardless of the total pressure in the tunnel or the nozzle chamber.

The first stage in the test setup is securing the removable floor plate in to the test section of the wind tunnel (Fig. 6-4). The floor plate is a 12 x 9 x ½ inch piece of stainless steel which can be seen with dimensions in Figure 5-9. Although variations in the temperature will be small ($\Delta T \sim 30$ K) during testing, both the sensor plug housing and sensor plug are also stainless steel so that wall temperature variations are minimized. Four #¼ -20 socket head cap screws hold the floor plate by the corners in the test section.

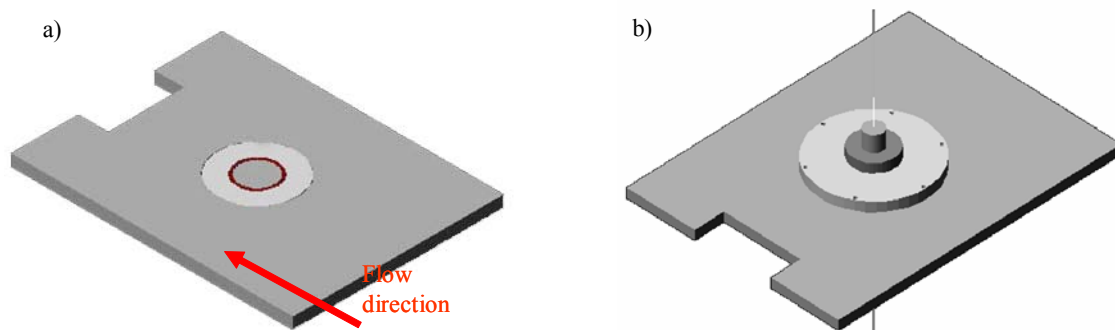


Figure 6-4. Top (a) and bottom (a) views of removable floor plate.

There is a large difference in the static pressure in the tunnel and the ambient pressure outside the tunnel ($\Delta P \sim 10$ psia) when in operation. Every effort was made to ensure no leakage took place into the test section which would alter the flow field. This was done by sealing the bottom of the floor plate to the test section with a 100% silicon rubber sealant. A minimum of 12 hours was given between the application of the sealant

CHAPTER 6 – SUPERSONIC WIND TUNNEL TESTING

and testing to ensure the sealant had set up. Any irregularities in the floor plate were eliminated using 250 grit multi-purpose sandpaper or filled with a pliable hard wax.

The second step was inserting the sensor plug housing/sensor plug/sensor into the floor plate. This was done using six #6-32 x $\frac{3}{4}$ inch socket head cap screws. The bolts were tightened until the sensor plug housing was flush with the floor plate. The silicon rubber sealant was not used since the tolerances between the two pieces were small (± 0.0005 inches) and no leaks were present. A detailed dimension drawing of the sensor plug housing can be seen in Figure 5-8. Figure 6-5 is a photograph of the test section after the installation process was complete. The final step is setting up the data acquisition equipment for the temperature and shear sensor as mentioned above.

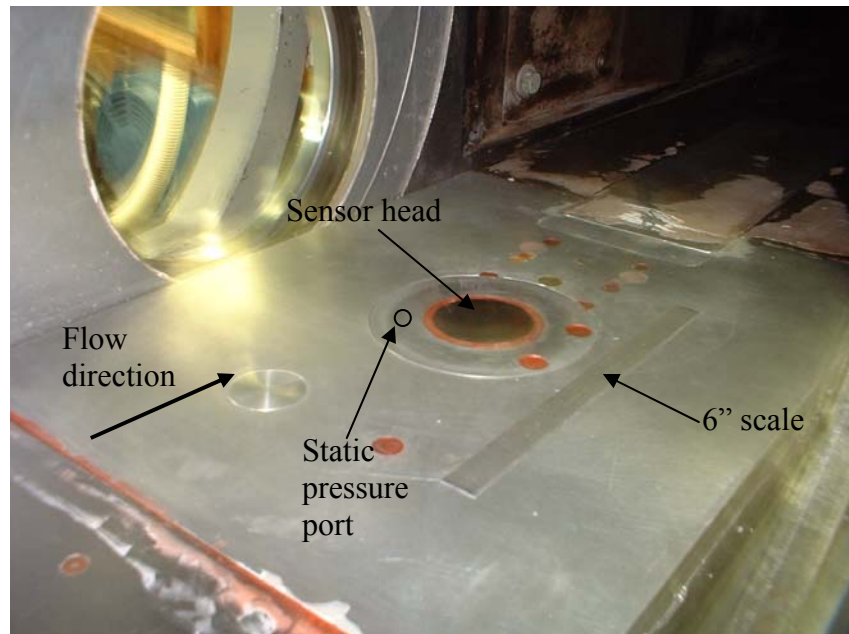


Figure 6-5. Photograph of floor plate, sensor plug housing, shim stock and sensor in the test section. Scale on tunnel floor is 6" in length.

6.3 Supersonic Wind Tunnel Test Results

6.3.1 Initial Testing at Mach 2.4

The large number of sensor heads that detached during calibration due to growth bond failure caused concern about the survivability of the gage in wind tunnel tests. As mentioned previously, there is a non-trivial pressure variation during the starting of the wind tunnel. For Mach 2.4 tests the pressure difference is approximately 10 psia. This

pressure difference is even more substantial at Mach 4.0 where $\Delta P = 12$ psia. The time over which these pressure differences occur is approximately 0.5 seconds. Initial test runs of a sensor without the fiber-optics were conducted to investigate the survivability of the gage.

Figure 6-6 displays the tunnel conditions for the initial test runs conducted at Mach 2.4. The quick decrease in static pressure (P_{static}) from an ambient pressure of about 14 psia to 4 psia can be seen.

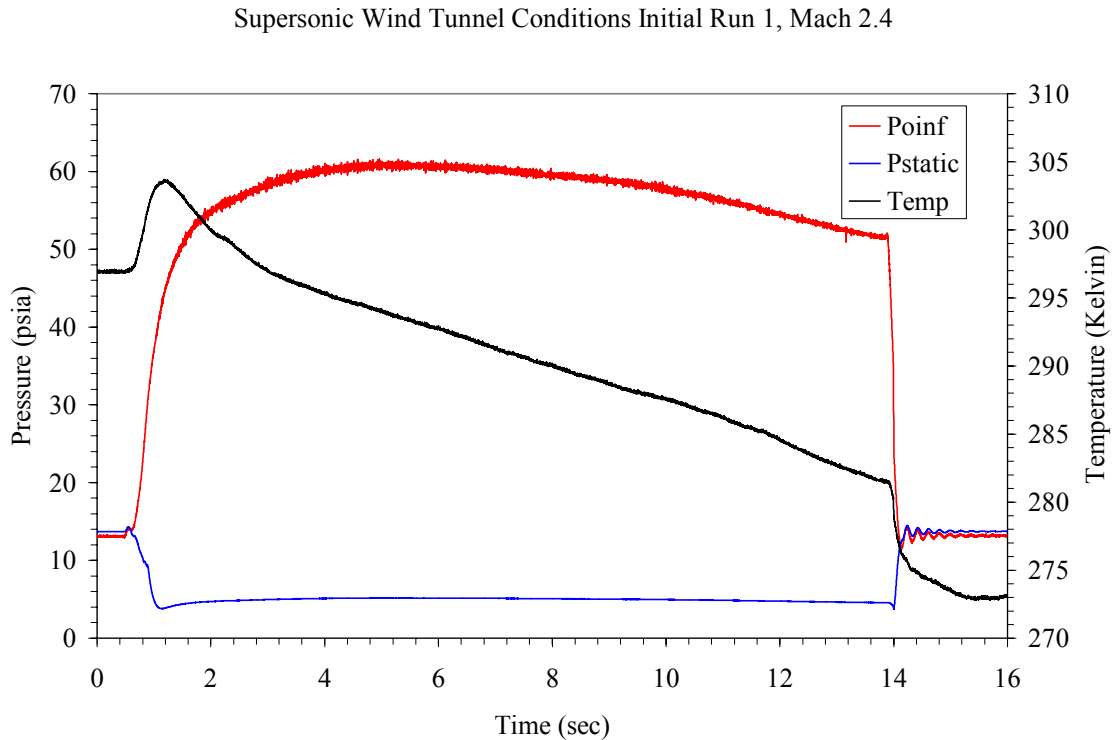


Figure 6-6. Tunnel conditions for initial test run 1 at nominal Mach 2.4.

During the starting of the wind tunnel of the initial testing (Run 1), the sensor head did not survive. Figure 6-7 is a photograph taken by the high speed camera of the sensor head traveling down the tunnel after failure. Upon inspection of the substrate it was clear that the nanotube growth bond had failed. This was indicated by the black layer left on the 1 x 1 cm silicon substrate. Had the epoxy bond been the mode of failure, no black residue would be left on the substrate.

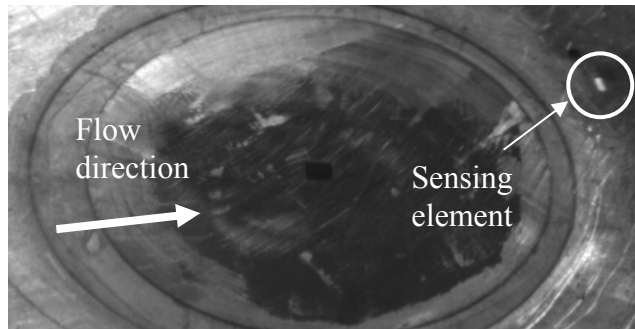


Figure 6-7. Single picture captured by high speed camera operating at 500pps after sensor head failure.

6.3.2 Vacuum Test of Sensor

The array of carbon nanotubes is not a solid element. Within the array of nanotubes pockets of air exist. It was suggested that when the wind tunnel starts these pockets of air evacuate the array. In this evacuation process, a large amount of the air attempts to escape by exiting through the gap around the sensor head creating a normal force on the head (Fig 6-8). A pressure difference of 10 psia corresponds to a force of 0.28 N. This force is approximately 280 times greater than the shear force applied to the sensor head.

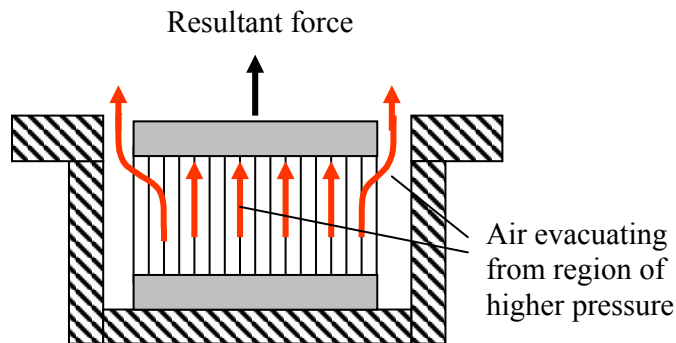


Figure 6-8. Schematic illustration of air pockets in nanotube array evacuating region of high pressure to region of lower pressure, creating a normal force on the sensor head.

To test this hypothesis an experiment was set up which simulated the sensor being subject to a sudden change in pressure equal to that in the wind tunnel. A sensor identical to the one which failed in the wind tunnel was placed in a 300 mL airtight beaker. The beaker was hooked to a vacuum pump and pressure transducer via a ‘T’ connector. An

CHAPTER 6 – SUPERSONIC WIND TUNNEL TESTING

on/off valve was positioned between the vacuum pump and beaker (Fig. 6-9). The vacuum pump was turned on such that the pressure in the chamber was approximately 2 psia. When the valve was switched to allow flow through, the air at ambient pressure in the beaker instantly evacuated. The pressure transducer does not measure the exact pressure of the beaker. However, it was placed as close to the beaker as possible to ensure the most accurate pressure measurements were taken.

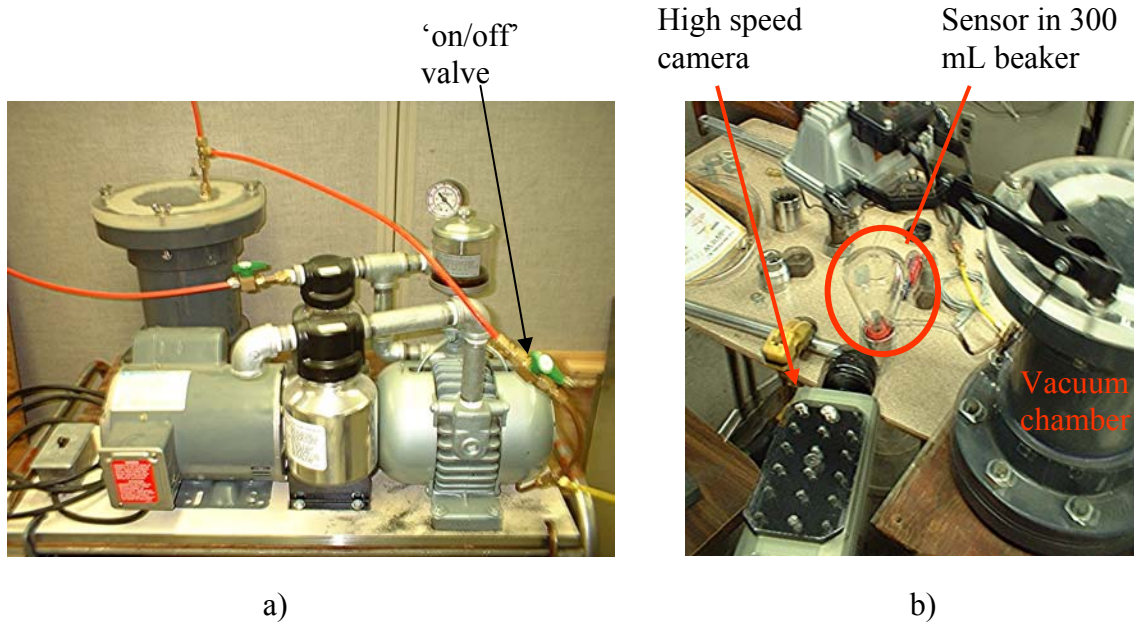


Figure 6-9. Photographs of the vacuum pump (a) and of the experimental setup (b).

Figure 6-10 displays the pressure in the beaker and the ambient pressure. The pressure in the beaker drops from 13.8 to 2.15 psia in 1.05 seconds. Comparing the beaker pressure in Figure 6-10 to the static pressure in Figure 6-6, it can be seen that this experiment closely simulates the change in pressure the sensor experiences in the wind tunnel. However, the venting of the air pockets in the experiment is not constrained to exit a small gap surrounding sensor head. An additional experiment should be performed which more closely constrains the air to vent through a small gap surrounding the sensor head.

After this conclusion was made the video taken by the high speed camera during the initial wind tunnel testing was revisited. In the video it was noticed that after the sensor head detached the shim stock began to buckle. This indicated that ambient air was

being sucked in to the test section of the tunnel. Upon inspection of the sensor housing and plug, a leak was found where the optical fibers entered the sensor plug. This leak acted like a small jet, funneling air from the room through the hole and into the test section of the wind tunnel. The leak was sealed using a 5-minute epoxy, and a second sensor was tested in the wind tunnel. The test conditions are represented in Figure 6-6. In this initial run the sensor head stayed attached throughout the entire test. One more run was successfully conducted which led to the conclusion that the problem was fixed.

Vacuum Test of Sensor

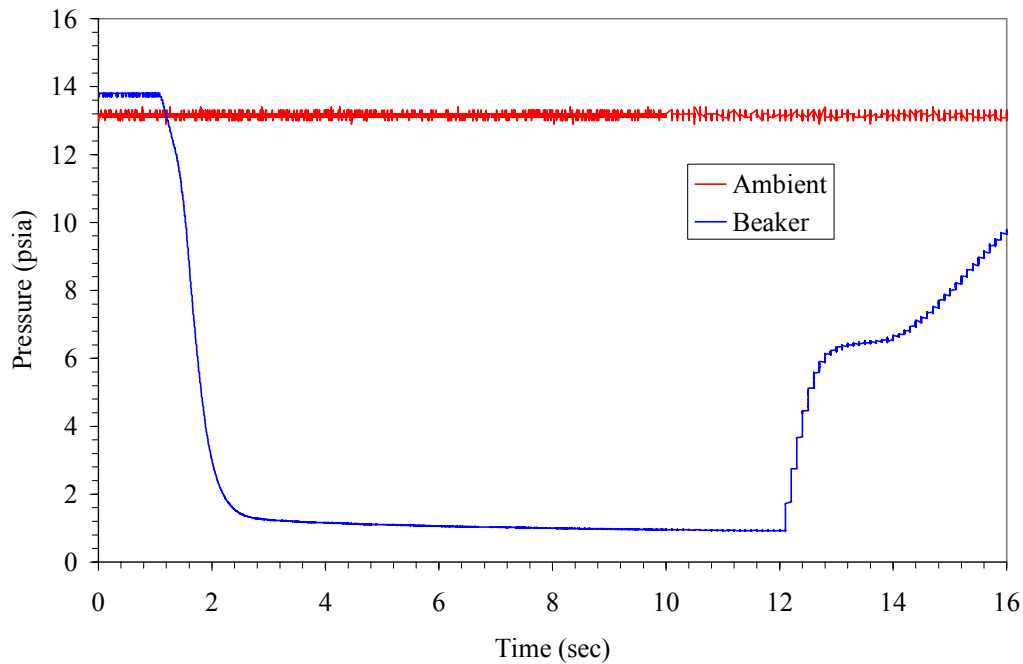


Figure 6-10. Measured ambient pressure and pressure in beaker through vacuum test to simulate starting of Mach 2.4 wind tunnel.

6.3.3 Mach 2.4 Results

Six test runs were conducted at Mach 2.4. The tests were run so that the gap change would increase when the sensing element was displaced. Throughout the first set of test runs conducted at Mach 2.4 the total pressure was altered to document the gages response to various shear levels. Table 6-1 displays the various test runs and the recorded tunnel pressures.

Figure 6-11 is a representation of the tunnel conditions throughout the wind tunnel testing. The total pressure is indicated in red, the static pressure in blue and the

CHAPTER 6 – SUPERSONIC WIND TUNNEL TESTING

total temperature in black. This figure is characteristic of all test runs performed at Mach 2.4. The total pressure rises to the value the user sets when the wind tunnel starts then levels out and becomes fairly constant after approximately one second. The static pressure decreases to a constant value over approximately half a second and remains at this value until the tunnel unstarts. The total temperature increases 5 degrees Kelvin during the starting of the wind tunnel. It then decreases in a nearly linear fashion until the tunnel unstarts. The actual Mach number is obtained by finding the ratio of the static pressure to the total pressure once the values are steady (between 4 – 12 seconds). This ratio gives a Mach number of approximately 2.29.

Test Run #	Mach	Ptotal (psia)	Pstatic (psia)
1	2.28	52	4.3
2	2.29	55	4.5
4	2.31	70	5.5
5	2.30	68	5.5
6	2.32	88	6.8
7	2.31	89	7.0
8	2.29	70	5.7

Table 6-1. Test runs conducted on 05-27-04 at a nominal Mach number of 2.4.

Supersonic Wind Tunnel Conditions Run 02, Mach 2.4

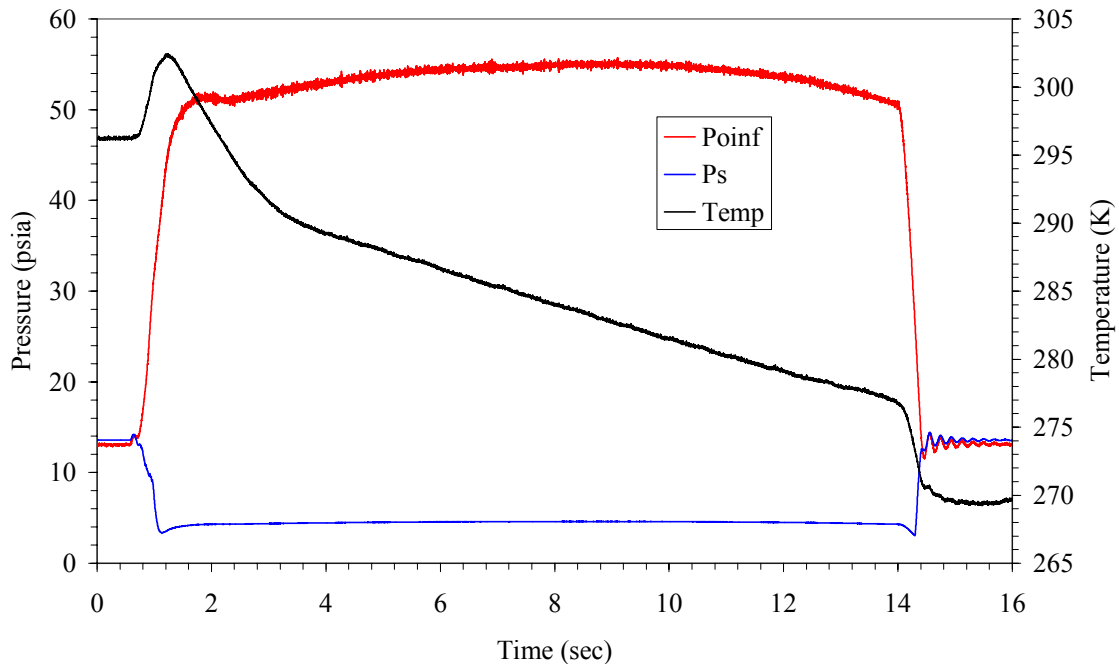


Figure 6-11. Representative tunnel conditions for nominal Mach 2.4.

The shear and temperature measurements, indicated in blue and red respectively, for Run 02 are presented in Figure 6-12. The gap distance of the fiber optic shear sensor is labeled on the left hand scale in microns, and the temperature scale in Kelvin is located on the right hand side of the plot. Before the wind tunnel starts the average gap distance of the shear sensor is 113.730 microns. The violent starting of the wind tunnel can be seen in the jagged peaks in the data due sudden loads being exerted on the gage. Once the starting process is over, the gap distance settles to a constant value between 18.3 and 18.9 seconds. The average value in this time span is 113.743 microns. The total gap distance change is 12.7 nm. Using the calibration equation in Chapter 5, this corresponds to a wall shear value of approximately 134 Pa. The wall shear can be non-dimensionalized by the dynamic pressure (Eqn. 6-1) to obtain the skin friction coefficient,

$$q = \frac{1}{2} \rho U_e^2 = \frac{1}{2} \gamma P_s M^2 \tag{6-1}$$

where γ is the ratio of specific heats of air, P_s is the local static pressure and M is the Mach number. For this case the values of these parameters are 1.4, 31kPa (4.5 psia), and 2.29 respectively, yielding the result $C_f = 0.00119$.

Supersonic Wind Tunnel Test Run 02, Mach 2.4

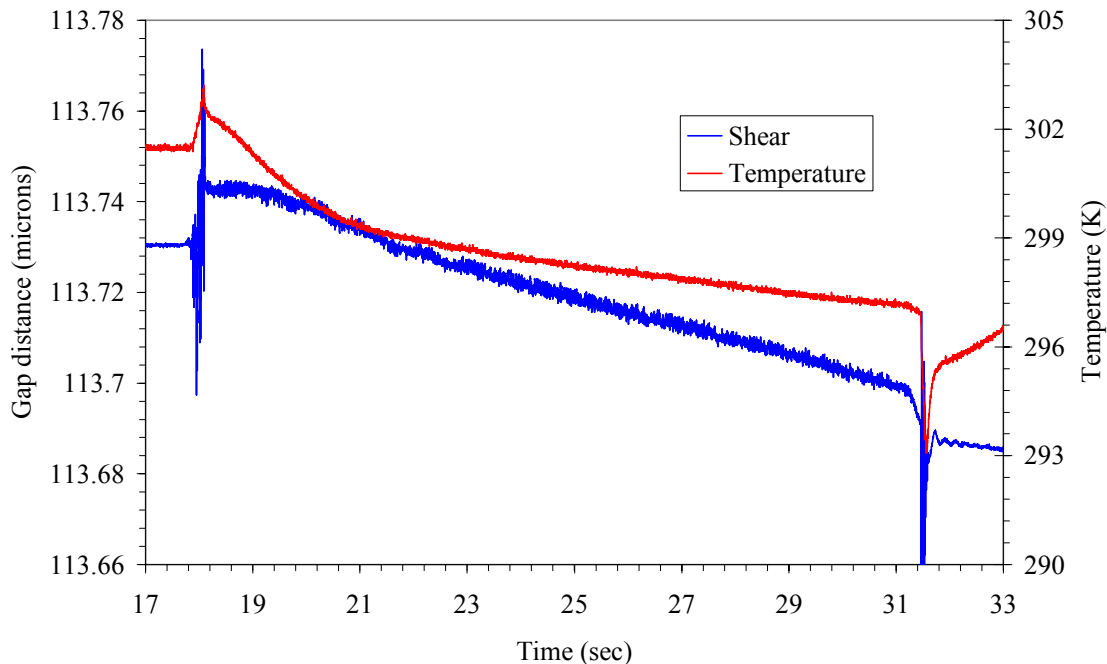


Figure 6-12. Shear and temperature measurements of Run 02 at Mach 2.4.

CHAPTER 6 – SUPERSONIC WIND TUNNEL TESTING

After the initial displacement of 12.7 nm, the gap began to decrease in a near linearly fashion. Upon comparison with the displacement measurements, it is observed that the temperature data responds in a similar fashion. A constant value of temperature is seen prior to the wind tunnel starting. Once the wind tunnel starts a sudden increase in temperature occurs. The temperature then decreases for the duration of the test run. It can be seen in Figure 6-12 that the drift in the gap distance follows the decrease in static temperature. This drift in the gap distance can be accounted for in a post calibration. This static calibration involves varying the temperature measuring the corresponding change in gap distance.

Once the wind tunnel unstarts the sensor has a second gap change of approximately -11.6 nm. The second gap change is within ~10% of the initial displacement. This indicates that the sensor responded to an initial shear force by a positive gap change and returned to within 10% of that gap change once the shear force was removed.

Before Run 03 was conducted it was noticed that the sensing element appeared to be recessed a small distance below the shim stock. This was verified by placing a piece of paper over the shim stock and recessed sensing element and shining a light at the recessed area. To compensate, the element was raised vertically via the vertical positioning stage and monitored with the paper and light. Once the recessed area disappeared, the sensing element was flush with the shim stock. The distance raised was not recorded.

Test Run 03 was performed at similar test conditions as seen in Figure 6-11. The shear and temperature measurements for Run 03 are shown in Figure 6-13. The beginning of Run 03 behaves almost identical to Run 02. The gap distance is constant until the wind tunnel starts, at which point the gap jumps violently due to the sudden load on the gage. Once the process of the tunnel starting subsided, the gap distance had increased approximately 14.5 nm, corresponding to a wall shear of 153 Pa. Substituting the appropriate values in to Eqn. (6-1), yields $C_f = 0.00132$.

Two distinct anomalies occur during Run 03. The first irregularity occurs between 15 and 16 seconds when the gap distance suddenly increases 5 nm. It is expected that after the initial gap change, the gap distance would decrease as the

CHAPTER 6 – SUPERSONIC WIND TUNNEL TESTING

temperature decreases. This indicates an event occurring which produced a relatively large gap change that cannot be accounted for. The second anomaly occurs during and after the unstarting of the wind tunnel. As seen in the figure, the gap changes violently over a time span of 4 seconds. This is drastically different from Run 02, in which the gap changes dramatically for the duration of 0.1 seconds. After the 4 seconds elapsed, the gap distance suddenly increases. This is opposite behavior of what is expected, since the gap should decrease after the load has been removed. It is assumed the gage was damaged during this run.

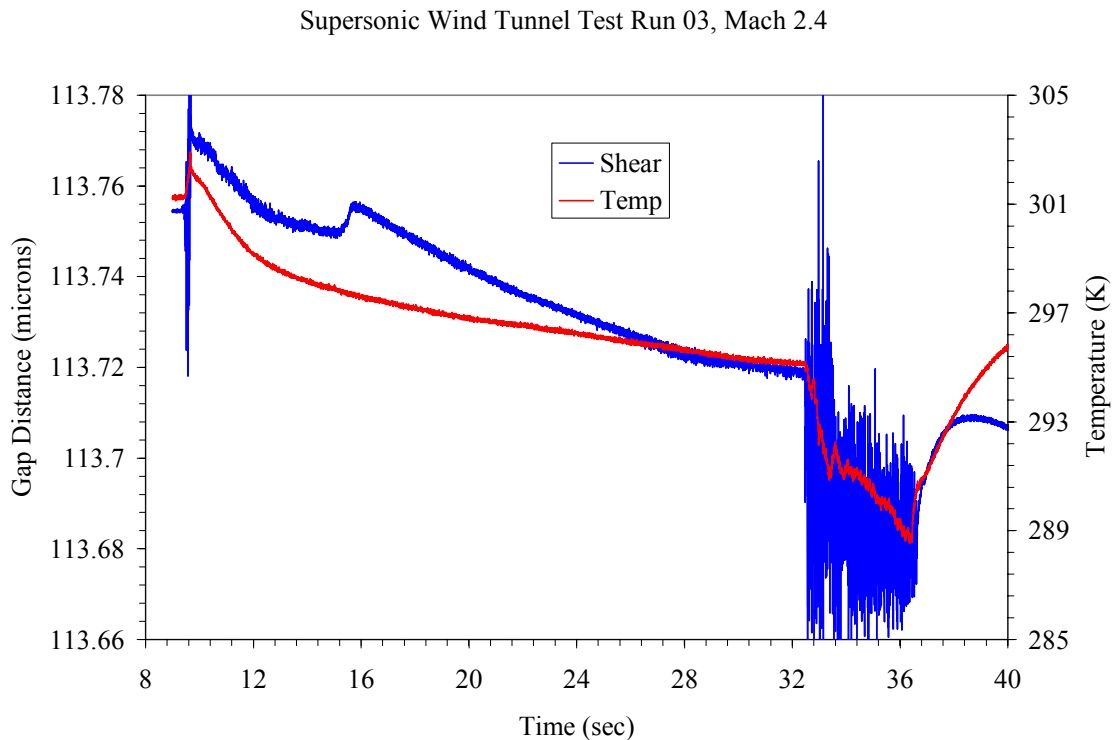


Figure 6-13. Shear and temperature measurements of Run 03 at Mach 2.4.

The following run was conducted in slightly different wind tunnel conditions by increasing the total pressure to 70 psia. Increasing the total pressure directly increases the wall shear stress in the wind tunnel. Theoretically, the sensor will respond to the larger shear level by displacing a greater distance. Figure 6-14 displays the shear and temperature data for Run 04. In this test run the initial gap change is approximately 3 nm, corresponding to 32 Pa. The shear data supports the assumption that the sensor was damaged in Run 03.

Supersonic Wind Tunnel Test Run 04, Mach 2.4

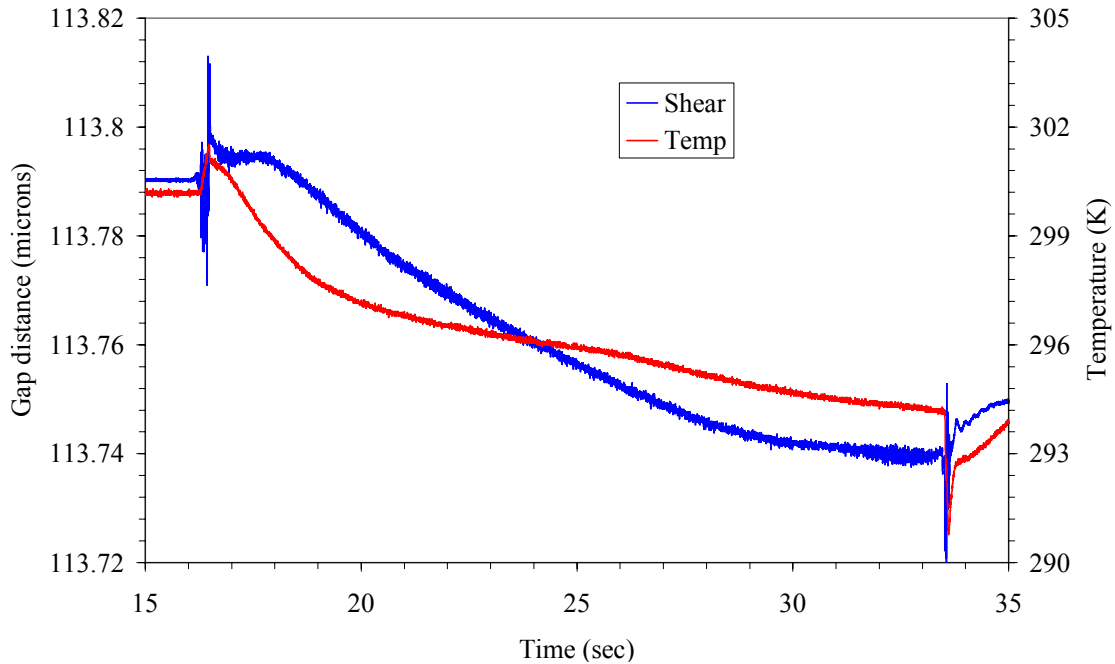


Figure 6-14. Shear and temperature measurements of Run 04 at Mach 2.4.

To validate the assumption that the sensor was damaged a recalibration was attempted at Luna Innovations. The sensor was setup for calibration in the housing used for wind tunnel tests. Upon the application of the string to the sensor head, it detached from the silicon substrate. The 2 x 2 mm black residue (nanotubes) left on the silicon substrate indicated that the growth bond was the mode of failure.

6.3.4 Comparison of Results

A boundary layer survey has been previously carried out by Orr [57] in which experimental results of the boundary layer thickness were obtained at these nominal tunnel conditions. From these results a Reynolds number based on the boundary layer thickness is calculated. Using the Reynolds number in an incompressible, flat-plate skin friction formula, values for C_f were found. The Van Driest II incompressible-to-compressible correction factor for C_f for Mach 2.4 was found in Figure 10-7 of Ref. [5] to be

$$\frac{C_{f,compress}}{C_{f,incompress}} = 0.66 \quad (6-2)$$

A second method of calculating an incompressible-to-compressible correction factor for C_f is the reference temperature method [57].

$$\frac{C_{f,compress}}{C_{f,incompress}} = \left(1 + r \frac{\gamma - 1}{4} M^2\right)^{-1} \quad (6-3)$$

Substituting $r = \sqrt{\text{Pr}} = \sqrt{0.7}$ and $\gamma=1.4$ for air and $M=2.4$ in to Eqn. (6-3) yields a correction factor of 0.682.

The two mentioned methods of predicting C_f using the boundary layer survey data for Mach 2.4, along with the four measurements obtained by Orr, and two measurements in Runs 2 and 3 are shown in Figure 6-15 [57]. The data points presented by Orr were obtained using a ‘non-nulling’ skin friction sensor. As seen the value obtained in Run 2 ($C_f = 0.00119$) is approximately 15 – 20% lower than the Van Driest II and reference temperature predictions. There is excellent agreement in the value measured in Run 3 with the Van Driest II model. The measured value, $C_f = 0.00132$ is within 3 and 7% of the Van Driest II and reference temperature predictions, respectively. Prior to the sensor being damaged, the measured values of skin friction showed good correlation to the predicted values. However, additional measurements are needed to assess the overall performance of the sensor.

CHAPTER 6 – SUPERSONIC WIND TUNNEL TESTING

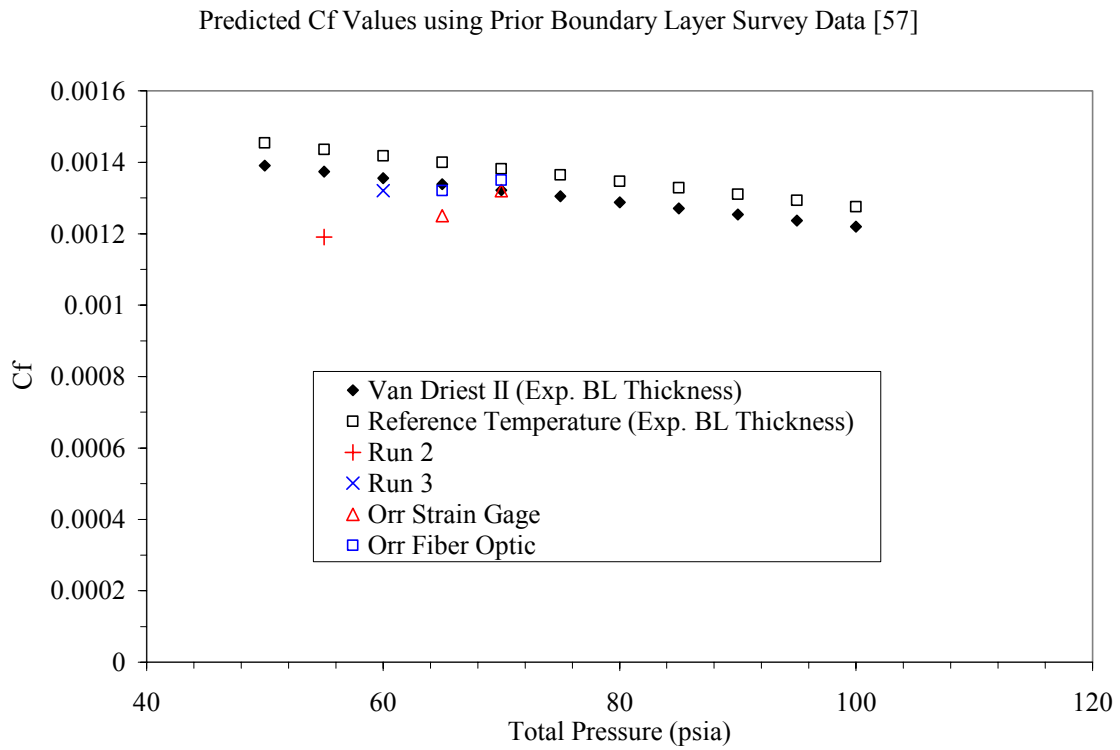


Figure 6-15. Predicted and measured skin friction values.

7 CONCLUSIONS AND RECOMMENDATIONS

An array of MWNTs supporting a shear sensor head has been tested in the Virginia Tech Supersonic Wind Tunnel with limited success. Two test runs were conducted at a nominal Mach number of 2.4 with good results. Run 2 measured a skin friction coefficient 15 – 20% lower than the predicted values by the Van Driest II and reference temperature methods using boundary layer survey results [57]. Run 3 was performed at a slightly higher total pressure and obtained a skin friction measurement 3 – 7% lower than the predicted values obtained through indirect measurements. While these first results are encouraging, additional test runs are needed to draw a conclusion on the reliability of this sensor.

Two distinct anomalies during Run 3 lead one to believe the sensor was damaged during this test run. The reason for the failure of the skin friction sensor is left for speculation. There are numerous possibilities ranging from human error to material failure. The following discussion presents a few of the many possible explanations for the failure of this skin friction gage.

The first possible cause for the gage's failure is that it was damaged during the vertical positioning of the sensing element between Run 2 and 3. Due to the delicacy of the device, if the sensor head was contacted during the alignment process, it could have disrupted either the epoxy bond or the growth bond. During the calibration of similar sensors, human interaction with the sensing element caused the growth bond to fail, detaching the sensor head. This indicates that the sensor is extremely fragile.

Another possible explanation of the failure of the sensor is the repeated venting of air from the nanotube array during the starting of each the wind tunnel test (Fig. 7-1). As mentioned in Chapter 6, the large pressure difference during the starting of the wind tunnel will cause the pockets of air in the nanotube array to try to escape through the gap around the perimeter of the sensor head. During this venting, a normal force results, attempting to push the sensor head vertically up. The previous experiment testing of this hypothesis did not simulate the wind tunnel tests exactly, due to the absence of the sensor housing. This experiment should be conducted again, replicating the wind tunnel environment more closely.

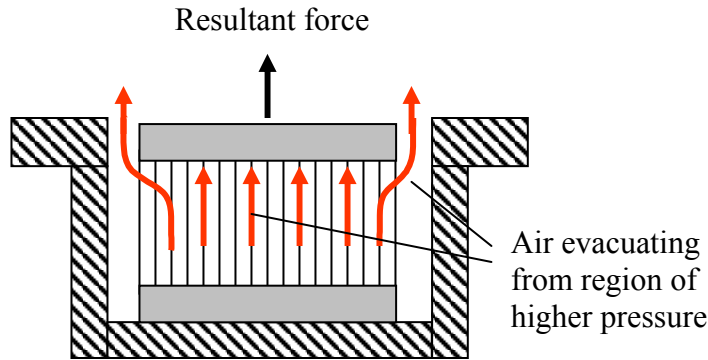


Figure 7-1. Schematic illustration of air pockets in nanotube array “venting” from region of high pressure to region of lower pressure, creating a normal force on the sensor head.

Another possible explanation of the failure of the gage is the exposure of the nanotubes to moisture over repeated test runs. Figure 7-2 is a SEM image of an array of once vertically aligned carbon nanotubes. This image was taken after the sample was exposed to moisture. It shows how the tips of nanotubes are attracted to one another in a ‘tee-peed’ manner. The sensor may have been exposed to moisture when the cold air in the plenum chamber condenses and moves through the test section after each run. It is unknown how this affects the growth or epoxy bonds or the mechanical properties of the nanotubes.

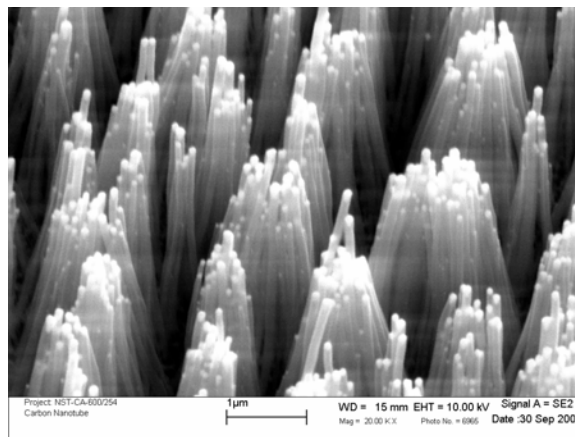


Figure 7-2. SEM image of an array of MWNTs exposed to moisture.

A lesser likelihood lies in the assumption that a foreign object caused the failure of the sensor. A small particle from within the sensor housing, i.e. loose epoxy, could have detached and contacted the sensor head during the test run.

CHAPTER 7 – CONCLUSIONS AND RECOMMENDATIONS

Research in the fields of nanotechnology and micro-manufacturing must advance before a reliable skin friction sensor can be fabricated utilizing carbon nanotubes. The major limitation in designing and fabricating a sensor is the submicron size of the nanotubes which requires fabrication techniques that are not well established. This lack of fundamental methodologies presents many obstacles when setting out to design such a device.

The most problematic area encountered in this exploratory study is the weakness of the growth bond between the nanotubes and the substrate. Of the 6 displacement sensors calibrated, 5 failures occurred. In each case there was a clear indication that the growth bond was the failure method. The black soot (nanotubes) left in 2 x 2 mm squares on the 1 x 1 cm silicon substrate revealed that the epoxy bond was more durable than the growth bond. There is no method to control the strength of the growth bond. Until pre-synthesis techniques are discovered that increase the growth bond strength, this area will remain a large obstacle of the fabrication of a reliable shear sensor.

Problems also exist with the epoxy bonding techniques. There is no precise control of the thickness or the uniformity of the thickness of the epoxy. If the epoxy is not laid down in a uniform thickness, this could potentially cause alignment issues. Research is needed to find the epoxies and techniques that are most suitable for this type of bonding scenario.

Currently, the one factor which plays a large role in the inability to use nanotubes in a reliable skin friction sensor is the lack of control over the quality and geometry of the nanotubes. Throughout this study the nanotubes have been modeled as perfect cylinders with identical lengths and diameters. There is not a method to ensure these dimensions are identical or that the nanotubes are free of defects. If one could select the geometry such that all metallic zigzag nanotubes were grown, the electromechanical method would look more promising. The electrical behavior of the system would be more predictable when subjected to mechanical deformation.

As the need for truly local skin friction measurements continues to grow, focus should remain on producing small skin friction sensors and *MEMS* gages. Once the constraints on selective nanotube growth, bonding procedures, and sub-micron

CHAPTER 7 – CONCLUSIONS AND RECOMMENDATIONS

fabrication techniques are lifted, an array of carbon nanotubes will be successfully utilized to make skin friction measurements.

REFERENCES

- [1] Vogel, S., *Life in Moving Fluids*, Princeton University Press, Princeton, New Jersey, pp. 96 – 97, 1994.
- [2] American International Automobile Dealers, “Jet-Fueled Ingenuity; As the price of flying soars, airlines try every trick they can think of to cut costs.” Retrieved June 8th, 2004 from World Wide Web: <http://www.aiada.org/article.asp?id=9647>
- [3] Smith, T.B. “Development and Ground Testing of Direct Measuring Skin Friction Gages for High Enthalpy Supersonic Flight Tests.” Ph.D. Dissertation, Aerospace and Ocean Engineering, Virginia Polytechnic Institute and State University, pp., 2001.
- [4] Charles, E. D., *Flight Theory and Aerodynamics*, John Wiley & Sons, New York, pp. 39 – 46, 1981.
- [5] Schetz, J.A., *Boundary Layer Analysis*, Prentice Hall, Englewood Cliffs, New Jersey, 1993.
- [6] Pulliam W. J., “Development of Fiber Optic Aerodynamic Sensors for High Reynolds Number Supersonic Flows”, Ph.D. thesis, Virginia Polytechnic Institute and State University, pp. 1 – 22, 2000.
- [7] Nitsche, W. and Haberland, C. and Thunker, R., “Comparative Investigation on Drag Measuring Techniques in Experimental Aerodynamics,” ICAS-84-2.4.2, 14th ICAS Congress, Sept. 1984.
- [8] Schetz, J.A., “Direct Measurements of Skin Friction in Complex Flows Using Movable Wall Elements,” AIAA 2004-2112, July 2004.
- [9] Paros, J.M. “Application of the Force-Balance Principle to Pressure and Skin Friction Sensors.” 16th Annual Technical Meeting, Proc. Inst. Environmental Sciences, pp.363 – 368, 1970.
- [10] Froude, W. “Experiments on the Surface-friction Experienced by a Plane Moving through Water.” 42nd British Association Report, pp. 118-125, 1872.
- [11] Kempf, G., *Neue Ergebnisse der Widerstandsforschung, Werft- Reederei-Hafen*, Vol. 11, no. 12, pp. 234-239, 1929.
- [12] Schoenherr, M.W. “Resistance of flat surfaces moving through a fluid.” *Trans. Soc. Nav. Archit Mar Engrs.*, vol. 40, pp. 279-313, 1932.
- [13] Schultz-Grunow, F. “Neus Reiwngswiderstandsgestez fur glatte Platten,“ *Luftfahrtforschung*, vol.17, pp. 239-246, (New frictional law for smooth plates).” NASA, TM 986, 1941.
- [14] Weiler, J.E. and Hartwig, W.H., “The direct measurement of local skin friction coefficient.” University of Texas, DR:-295, 1952.
- [15] Chapman, D. R. and Kester, R. H. “Measurements of Turbulent Skin Friction on Cylinders in Axial Flow and Subsonic and Supersonic Velocities.” *J. Aeronautical Sciences*, vol. 20, no. 7, pp 441-448, 1953.
- [16] Coles, D. “Measurements in the Boundary Layer on a Smooth Flat Plate in Supersonic Flow.” JPL Report 20-70, 1953.
- [17] Dhawan, S., “Direct Measurements of Skin Friction.” NACA Report 1121, 1953.
- [18] Eimer, M. “Direct Measurement of Laminar Skin Friction at Hypersonic Speeds.” Dissertation in Partial Fulfillment for the Degree of Master of Science in Aeronautical Engineering, University of Texas, Austin, August, 1958.

- [19] Hakkinen, R. J. "Measurements of Turbulent Skin Friction on a Flat Plate at Transonic Speeds." NACA 3486, 1955.
- [20] Blumer, C.B. "The Direct Measurement of Skin Friction on a Cone at Supersonic Speed. Masters Thesis, University of Minnesota, November, 1954.
- [21] Wolff, J.M. "An Evaluation of Equipment to Measure Directly the Skin Friction Forces on a Flat Plate." Masters Thesis, University of Minnesota, May, 1956.
- [22] Fenter, F.W. and Lyons, W.C., "The Direct Measurement of Local Skin Friction on Aerobee-Hi Rockets in Free Flight." University of Texas DRL-391, 1957.
- [23] Everett, H.U. "Calibration of Skin Friction Balance Discs for Pressure Gradient." University of Texas DRL-426, 1958.
- [24] Smith, D. W. and Walker, J. H. "Skin Friction Measurements in Incompressible Flow." NASA TR R26, 1959.
- [25] MacArthur, R.C. "Transducer for Direct Measurement of Skin Friction in the Hypersonic Shock Tunnel." CAL Report 129, Cornell Aero. Lab., Buffalo, NY, 1963.
- [26] Moulic, E.F., "Flat Plate Skin Friction in Low Density Hypersonic Flow-Preliminary Results." ARL Report 63-24, 1963.
- [27] O'Donnell, F.B., "A study of Effect of Floating Element Misalignment on Skin Friction Accuracy." University of Texas DRL-515, 1964.
- [28] Young, F.L. and Westkaemper, J. C., "Experimentally Determined Reynolds Analogy Factor for Flat Plates." AIAA J., vol. 3, no. 6, pp. 1201-1202, 1965.
- [29] Dershin, H., Leonard, C.A., Gallaher, W.H., and Palmer, J.P., "*Direct Measurement of Compressible Turbulent Boundary Layer Skin Friction on a Porous Flat Plate with Mass Injection.*" NASA CR 79095, 1966.
- [30] Moore, J.W. and McVey, E.S. "Investigation of Systems and Techniques for Multi-component Microforce Measurements on Wind Tunnel Models." University of Virginia Report EME-4029-102-66U, NASA CR-74385, 1966.
- [31] Brown, K.C. and Joubert, P.N. "Measurement of Skin Friction in Turbulent Boundary Layers with Adverse Pressure Gradients." J. Fluid Mechanics, vol. 35, pt. 4, pp. 737-757, 1967.
- [32] Fowke, J.G. "Development of a Skin Friction Balance to Investigate Sources of Error in Direct Skin Friction Measurements." NASA TM X 61905, N69-40-054, 1969.
- [33] Bruno, J.R., Yanta, W.J., and Risher, D. B. "Balance for Measuring Skin Friction in the Presence of Heat Transfer." Final Report. USA Naval Ordnance Lab., NOLTR-69-56, 1969
- [34] Winter, K.G. and Gaudet, L. "Turbulent Boundary Layer Studies at High Reynolds Numbers at Mach Numbers Between 0.2 and 2.8." ARC R&M 3712, 1970.
- [35] Hastings, R.C. and Sawyer, W. G. "Turbulent Boundary Layers on a Large Flat Plate at Mach 4." ARC R&M 3678, 1970.
- [36] Paros, J. M. "Application of the Force-Balance Principle to Pressure and Skin Friction Sensors." 16th Annual Technical Meeting, *Proc. Inst. Environmental Science*, 363-368, 1970.
- [37] Miller, B. L. "A Floating-Element Skin-Friction Meter," University of Leicester England Department Report 71-19, 1971.

- [38] Franklin, R. E. "Some Measurements with Simple Skin Friction Balances," University of Oxford Report 1058/73. *ARC 3447*, 1973.
- [39] Waltrup, P. J. and Schetz, J.A., "Supersonic Turbulent Boundary Layer Subjected to Adverse Pressure Gradients," *AIAA J.*, vol. 11, no. 1, pp. 50-57, 1973.
- [40] Morsy, M. G. "An Instrument for the Direct Measurement of the Local Wall Shear Stress on Circular Cylinders," *J. Physics E*, vol. 7, pp. 83-86, 1974.
- [41] Frei, D. and Thomann, H., "Direct measurements of skin friction in a turbulent boundary layer with a strong adverse pressure gradient," *J. Fluid Mech.*, vol. 101, pp. 79-95, 1980.
- [42] Allen, J. M. "Improved Sensing Element for Skin-Friction Balance Measurements," *AIAA J.*, vol. 18, no. 11, pp.1342-1345, 1980.
- [43] Schetz, J.A. and Nerney, B., "The Turbulent Boundary Layer with Injection and Surface Roughness," *AIAA J.*, Vol. 15, No. 9, pp. 1288-1294, 1977.
- [44] Kong, F. and Schetz, J. A. "Turbulent Boundary over Porous Surfaces with Different Geometries." *AIAA 82-0030*, January 1982.
- [45] Collier, F. and Schetz, J.A., "Injection into a Turbulent Boundary Layer Through Different Porous Surfaces," *AIAA J.*, vol. 22, no. 6, pp. 839-841, 1984.
- [46] DeTurris, D., Schetz, D., and Hellbaum, R. F. "Direct Measurements of Skin Friction in a SCRAMjet Combustor." *AIAA Paper 90-2342*, July 1990.
- [47] Kelly, G. M., Simmons, J. M., and Paull, A., "Skin-friction Gage for Use in Hypervelocity Impulse Facilities." *AIAA J.*, vol. 30, no. 3, pp. 844-845, 1992.
- [48] Chadwick, K., DeTurris, D.J. and Schetz, J.A., "Direct Measurements of Skin Friction in Supersonic Combustion Flowfields," *J. Eng. Gas Turbines and Power*, vol. 115, no. 3, pp. 507-514, 1993.
- [49] Bowersox, R., Schetz, J. A., Chadwick, K., and Diewert S., "Technique for Direct Measurements of Skin Friction in High Enthalpy Impulsive Scramjet Experiments." *AIAA J.*, vol. 33, no. 7, pp. 1286-1291, 1995.
- [50] Paik, S. and Schetz, J.A., "Simultaneous Direct Measurement of Skin Friction and Heat Flux in a Supersonic Flow." *The 6th Asian Congress of Fluid Mechanics: Proceedings*. V.T. Chew and C.P. Tso Eds., Vol. 2. Singapore. May 22-26, 1995.
- [51] Novean, M., Schetz, J.A., and Bowersox, R. "Skin Friction Measurements in Short Duration, High Enthalpy Flows." *AIAA 95-6109*, April 1995.
- [52] Remington, A. and Schetz, J.A., "A Study of Magnetically Damped Skin Friction Measurements for High Vibration Environments," *AIAA 2000-2522*, June 2000.
- [53] Magill, S., MacLean, M., Schetz, J.A., Kapania, R., Sang, A. and Pulliam, W., "Study of Direct-Measuring Skin-Friction Gage with Rubber Sheet for damping," *AIAA J.*, vol. 40, no.1, pp. 50-57, 2002.
- [54] Sang, A. and Schetz, J.A., "Study of Rubber Damped Skin Friction Gages for Transonic Flight Testing," *AIAA 2002-0533*, Jan. 2002.
- [55] Goldfeld M., Nestoulia R., and Falempin F., "The Direct Measurement of Friction in the Boundary Layer at Supersonic Flow Velocities." *AIAA 2002-5199*, October 2002.
- [56] Goyne, C.P., Stalker, R.J. and Paull, A., "Transducer for Direct Measurement of Skin Friction in Hypervelocity Impulse Facilities," *AIAA J.*, vol. 40, no.1, pp. 42-49, 2002.

- [57] Orr, M.W., Schetz, J.A. and Fielder, R.S., "Design, Analysis and Initial Tests of a Fiber-Optic Shear Gage for 3D, High-Temperature Flows," AIAA 2004-0545, Jan. 2004.
- [58] Dresselhaus, M.S., Dresselhaus, G. and Avouris, P. (Eds.), *Carbon Nanotubes: Synthesis, Structure, Production and Application*, Springer, Heidelberg, 2001, pp. 294 – 295.
- [59] Nature, "Focus on Carbon Nanotubes." Retrieved January 13th, 2004 from World Wide Web: <http://www.nature.com/nsu/991202/991202-1.html>
- [60] Berkley Lab Research Review, "Nanotubes" Superhard, Superstrong, Super useful." Retrieved on January 14th, 2004 from World Wide Web: <http://www.lbl.gov/Science-Articles/Research-Review/Magazine/2001/Fall/features/02Nanotubes.html>
- [61] Carbon Nanotube: Next Generation Sensor, Retrieved on March 15th, 2004 from the World Wide Web: http://boiling.seas.ucla.edu/shashank/cool_stuff/CarbonNanotube.pdf
- [62] Physicsweb, "Carbon Nanotubes", Retrieved January 8th, 2004 from the World Wide Web: <http://physicsweb.org/box/world/11/1/9/world-11-1-9-1>
- [63] Tomanek, D. and Enbody, R.J. (Eds.), *Science and Application of Nanotubes*, Kluwer Academic/Plenum Publishers, New York, 2000, pp. 94.
- [64] Wong, E.W., Sheehan, P.E. and Lieber, C.M., *Science* **277**, 1971 (1997).
- [65] Treacy, M.M.J., Ebbesen, T.W., and Gibson, J.M., *Nature* **381**, 678 (1996).
- [66] Treacy, M.M.J., Dujardin, E., Ebbesen, T.W., Krishnan, A., and Yianilos, P.N., *Phys. Rev. B* **58**, 14013 (1998).
- [67] Salvétat, J.P., Briggs, G.A.D, Bonard, J.M, Bacsá, R.W., Kulik, A.J., Stockli, T., Burnham, N.A. and Forró, L., *Phys. Rev. Lett.* **82**, 944 (1999).
- [68] Muster, J., Burghard, M., Roth, S., Düsberg, G.S., Hernández, E., Rubio, A. and Vac, J., *Science Tech.* **16**, 2796 (1998).
- [69] Collins, P.G. and Avouris, P., *Appl. Phys. A* **74**, 329 (2002).
- [70] Frank, S., Poncharal, P., Wang, Z.L., de Heer, W.A., *Science* **280**, 1744 (1998).
- [71] Tomblér, T.W., *Nature* **405**, 769 (2000).
- [72] Maiti, A., Svizhenko, A., and Anantram, M.P., *Phys. Rev. Lett.* **88**, 126805 (2002).
- [73] Dresselhaus, M.S., Dresselhaus, G. and Avouris, P. (Eds.), *Carbon Nanotubes: Synthesis, Structure, Production and Application*, Springer, Heidelberg, 2001, pp. 30.
- [74] Carbon Nanotube Fabrication, Retrieved on June 6th, 2004 from the World Wide Web : http://www.ee.virginia.edu/~cmf6p/research_docs/nanotubes.pdf
- [75] Andrews, R., Jacques, D., Qian, D. and Rantell, T., *Acc. Chem. Res.* **2002**, 35, 1008 – 1017.
- [76] Ren, Z.F., *Science* **282**, 1105 (1998).
- [77] Zdravkovich, M. M., *Flow around Circular Cylinders Vol. 1: Fundamentals*, Oxford Science Publications, Oxford, New York, 1997.
- [78] White, F. M., *Viscous Fluid Flow*, McGraw-Hill, New York, 1991.
- [79] Dresselhaus, M.S., Dresselhaus, G. and Avouris, P., (Eds.), *Carbon Nanotubes: Synthesis, Structure, Production and Application*, Springer, Heidelberg 2001. pp. 30.

- [80] Timoshenko, S. and Gere, J., *Mechanics of Materials*, Van Nostrand Reinhold Co., New York, 1972.
- [81] Vogel, S., *Life in Moving Fluids*, Princeton University Press, Princeton, New Jersey, pp. 96 – 97, 1994.
- [82] Zdravkovich, M. M., *Flow around Circular Cylinders Vol. 2: Applications*, Oxford Science Publications, Oxford, New York, 1997.
- [83] Safaai-Jazi, A., “Electromagnetic Modeling of Carbon Nanotube Structures,” Report submitted to Luna Innovations, Inc. Bradley Department of Electrical and Computer Engineering, Virginia Tech, pp. 1-11, August 2001.
- [84] W. A. de Hear, W. S. Bacsa, A. Chatelain, T. Gerfin, R. Humphrey-Baker, L. Forro, and D. Ugarte, *Science* **268**, 845 (1995).
- [85] Dresselhaus, M.S., Dresselhaus, G. and Avouris, P. (Eds.), *Carbon Nanotubes: Synthesis, Structure, Production and Application*, Springer, Heidelberg, 2001, pp. 339.
- [86] Pulliam, W.J. “Development of Fiber Optic Aerodynamic Sensors for High Reynolds Number Supersonic Flows.” Ph.D. Dissertation, Aerospace Engineering Department, Virginia Polytechnic Institute and State University, 2000.
- [87] Dresselhaus, M.S., Dresselhaus, G. and Avouris, P. (Eds.), *Carbon Nanotubes: Synthesis, Structure, Production and Application*, Springer, Heidelberg, 2001, pp. 41 – 42.
- [88] Bingqing Wei, B., Zhang, Z.J., Ramanath, G. and Ajayan, P.M., *Appl. Phys. Lett.* **77**, 19 (2000)
- [89] Charlier, J.C., *Acc. Chem. Res.* **2002**, 35, 1063-1069
- [90] AutoSignal Contents, “Goodness of Fit Statistics.” Retrieved on July 1st, 2004 from the World Wide Web: http://www.clecom.co.uk/science/autosignal/help/Goodness_of_Fit_Statistics.htm
- [91] Luna Innovations, “Temperature Sensors at Luna Innovations.” Retrieved on July 5th, 2004 from the World Wide Web: <http://www.lunainnovations.com/products/temperature.htm>
- [92] Aerospace and Ocean Engineering Department, “Supersonic Wind Tunnel,” Retrieved on June 1st, 2004 from the World Wide Web: <http://www.aoe.vt.edu/research/facilities/superson.php>
- [93] Schetz, J.A., “Direct Measurements of Skin Friction in Complex Flows,” *Appl. Mech. Rev.*, Vol. 50, No. 11, Pt. 2, Nov. 1997.
- [94] Worthy, M. and Schetz, J.A., "Experimental Study of Slot Injection into a Supersonic Stream," *AIAA J.*, Vol. 11, No. 5, 1973.
- [95] Schetz, J.A. and Van Overeem, J., "Skin Friction Reduction by Injection Through Combinations of Slots and Porous Sections," *AIAA J.*, Vol. 13, No. 8, pp. 971-2, 1976.
- [96] Remington, A. “A Study of Non-Fluid Damped Skin Friction Measurements for Transonic Flight Applications.” Masters Thesis, Aerospace and Ocean Engineering Department, Virginia Polytechnic Institute and State University, 1999.
- [97] Sang, A. “ Study of Rubber Damped Skin Friction Gages for Transonic Flight Testing.” Masters Thesis, Aerospace Engineering Department, Virginia Polytechnic Institute and State University, 2001.

- [98] Smith, T.B., Schetz, J.A. and Bui, T, "Development of Direct-Measuring Skin Friction Gages for Hypersonic Flight Tests," AIAA J., vol. 41, no. 8, pp. 1429-37, 2003.